Strain-engineered CMOS-compatible Ge Photodetectors

By

Douglas Dale Cannon

Submitted to the Department of Materials Science and Engineering in Partial Fulfillment
of the Requirements for the Degree of

Doctor of Philosophy in Electronic Materials

at the

Massachusetts Institute of Technology
[February 2004]
November 2003

Signature of Author:_____
Department of Materials Science and Engineering

Certified by:_____
Lionel C. Kimerling
Thomas Lord Professor of Materials Science and Engineering
Thesis Supervisor

Accepted by: _____
Harry L. Tuller
Professor of Ceramics and Electronic Materials
Chair, Departmental Committee on Graduate Students

Strain-engineered CMOS-compatible Ge Photodetectors

By

Douglas Dale Cannon

Submitted to the Department of Materials Science and Engineering
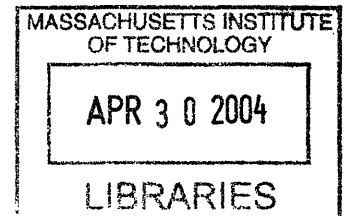on November 5, 2003 in Partial Fulfillment of the Requirements for the
Degree of Doctor of Philosophy in Electronic Materials

ABSTRACT

The development of CMOS-compatible photodetectors capable of operating throughout the entire telecommunications wavelength spectrum will aid in the integration of photodetectors with Si microelectronics, thus offering a low cost platform for high performance photoreceivers. This thesis demonstrates the first CMOS process compatible high-responsivity Ge p-i-n diodes for 1.55 μm wavelengths. The thermal expansion mismatch between Ge epilayers and Si substrates was used to engineer tensile strain upon cooling from the growth temperature. This 0.2% tensile strain results in a lowering of the direct transition energy in Ge by 30 meV and extends the responsivity curve to near 1.6μm.

Design rules are given for high speed and high responsivity, and the advantages of waveguide integration for simultaneous achievement of high speed and high responsivity are illustrated. It is shown that waveguide integration has advantages to vertical illumination when optical saturation is considered. Optical saturation will become important as photodetector sizes shrink to the order of a few tens of microns in diameter.

High Ge content SiGe could have applications for a SiGe electro-optic modulator utilizing the Franz-Keldysh effect. High Ge content SiGe films have been grown on Si substrates. The Franz-Keldysh effect has been observed in our pure Ge films as an increase in responsivity with increasing reverse bias for wavelengths longer than the bandgap energy.

Thesis Supervisor: Lionel C. Kimerling
Title: Thomas Lord Professor of Materials Science and Engineering

Acknowledgements

Many people have been instrumental in helping me through this thesis, but the first thanks goes to Kim, my fearless advisor, for his encouragement and endless optimism. He let me do things my way, allowing me to make some mistakes along the way, but was there when I needed him. And no one could ask for a better cheerleader.

Jurgen and Kazumi have been with me the whole time and have been an immense help with the day to day problems that arise in the course of research. Jurgen's ability to fix things in the lab was key when equipment went down, and Kazumi's helped me gain a better understanding of the theoretical matters.

Anat was a life saver when the reactor went down, and I don't think we could have fixed it without her. I can't thank her enough for her help through those tough months last winter, and because of her I now consider myself an expert in vacuum systems.

I owe a big thank you to all the students of EMAT for their friendship and support, and I especially want to thank Dave, Nok, and Jifeng. Their help in the lab was instrumental to getting here, and I owe a lot of the characterization work in this thesis to them. It was a privilege to help train them in the clean room when they were just starting out and amazing to see their progress. In their two years here at MIT they have all accomplished much more than I had after two years, and I expect great things out of them. I'm very thankful to them for all of their help along the way. My UROP Uche was also a big help in characterizing Ge films. I also share a special bond with Sajan, Jessica, and Mindy, who have also been in EMAT with me from the start. I couldn't mention EMAT without thanking Andy, who taught me how to use the reactor and was a fine example of a careful researcher.

When the reactor went down we all relied on Anat for her understanding of vacuum systems. She is an excellent teacher and so friendly and helpful. If it weren't for her help, we may have never fixed Gizelle.

Our industrial sponsors were a big help throughout and provided good insights, as well as help in the lab. Thanks to all the people at Analog and Pirelli who helped.

I also want to thank Tom Eagar and his group for their friendship and interesting consulting projects. I don't know anyone more generous than Tom. I learned so many practical lessons from those seemingly random consulting projects and was able to increase my standard of living and pay down student loans at the same time. I've enjoyed my friendship with Chris and will always remember the late nights last summer coloring chocolate. His work ethic is truly amazing. And Jeri was always so helpful with whatever I needed.

My friends outside of MIT have been a big help in keeping me sane. Now that this is done, I hope to have more time for them.

Finally, I want to thank my family. If it weren't for them, I would be here. Even though we're spread across the country now, I feel as close as ever. I am especially happy to have Erik and Cami out on the east coast with me. Being able to see them on a regular basis has been special. I expect the rest to make the trip out for graduation.

Table of Contents

List of Figures

Chapter 1: Introduction

Section 1.1   Motivation

Silicon microphotonics, the optical analog of microelectronics, is the integration of optoelectronic components on a Si substrate using CMOS-compatible processing technologies[1]. It involves the creation, control, processing, and detection of optical signals. Emitters[2], waveguides[3], modulators[4], amplifiers, and detectors[5-7] are some of the fundamental building blocks of microphotonic systems. Successful development of silicon microphotonics technologies will dramatically improve information processing capabilities and deliver the benefits of optoelectronic technology at a greatly reduced cost.

This thesis focuses on the development of CMOS-compatible photodetectors and modulators in the Ge and SiGe materials systems. This requires fundamental materials science, device simulation, and materials process development. SiGe is an ideal materials system for these applications for at least two reasons: 1) Ge is a completely miscible alloy in Si and is completely CMOS-compatible. 2) Although Ge is an indirect semiconductor, the direct energy transition is only 120 meV above the indirect transition, giving it many advantageous properties of direct semiconductors, such as a sharp absorption spectrum.

Following is a brief description of each chapter in this thesis.

Section 1.2   Outline of Thesis

In chapter two we consider many design and integration issues of monolithically integrated Ge photodetectors. Design plots are used to show the relationships between

11

depletion width, area, photocurrent, responsivity, and bandwidth. The performance advantages of waveguide integration are illustrated, and it is shown for the first time that waveguide integration allows for a potentially higher optical saturation point, as a result of the ability to use devices with thin depletion regions.

Chapter three is devoted to Ge and SiGe epitaxial growth by ultra-high vacuum chemical vapor deposition (UHVCVD). For pure Ge, high-yield selective epitaxial growth of Ge has been demonstrated by two methods. Photodetectors made from these selectively grown mesas are demonstrated in chapter four. Additionally, the ability to grow high Ge content SiGe directly on Si by utilizing a low temperature Ge buffer layer is demonstrated. Thermal annealing is shown to reduce the dislocation density of both Ge and SiGe films to the low $10^7/cm^2$ range.

In chapter four we show that the direct bandgap in our Ge films can be engineered by controlling the amount of tensile strain in the film. By utilizing the difference in thermal expansion coefficient of Ge and the underlying Si substrate, tensile strain can be introduced in the films, which results in a decrease in the direct transition energy, E_g^Γ. Theoretical predictions agree with our experimental results. The intrinsic carrier concentration of strained Ge is calculated, predicting a 15% increase in n_i for 0.2% tensile strain.

Chapter five is devoted to the processing of CMOS-compatible Ge p-i-n photodetectors on Si substrates. To our knowledge, this is the first time Ge photodetectors have been fabricated on Si using a completely CMOS-compatible process. Devices exhibit good electrical and optical characteristics, and the responsivity is shifted to longer wavelengths in agreement with the results of chapter four. SiGe p-i-n diodes

have also been fabricated, and the responsivity roll-off with wavelength agrees well with the bandgap measurements of chapter three.

Chapter six is devoted to the modulation of near infrared light using the Franz-Keldysh effect, which can be thought of as photon assisted tunneling of carriers from the valence band to the conduction band. While this effect is weak for an indirect semiconductor, near the direct band transition of Ge the effect is expected to be significant. The Franz-Keldysh effect is experimentally demonstrated in Ge photodetectors as an increase in responsivity for increased electric fields.

Chapter seven summarizes the main findings of this thesis and discusses directions for future work.

Chapter 2:   p-i-n photodetector design considerations

In this chapter we examine the expected performance of both vertically illuminated and waveguide-integrated Ge p-i-n photodetectors. The performance metrics we are primarily concerned with are frequency response and photocurrent, although we also need to know the photocurrent at the onset of saturation. We are specifically interested in understanding how varying the design parameters, such as the device area and depletion width, affects performance characteristics. We also want to determine if waveguide integration offers any advantages over vertical illumination.

We will show that waveguide integration does indeed offer fundamental advantages over vertical illumination, both in responsivity and saturation characteristics. While significant engineering and design issues still need to be solved to implement high performance waveguide integration in Ge photodetectors, no fundamental barriers exist that would prevent it. A discussion of the feasibility of waveguide integration is contained in the latter part of the chapter.

In the course of examining the above issues, we will create several design plots showing how changes in design parameters affect our performance metrics. This will allow us to determine the allowable design space for a given set of performance requirements and also illuminate the fundamental limitations of potential designs. We must make a few assumptions in making these calculations. First, we assume that all of the absorbed light is converted into electron-hole pairs that are collected and measured as current. This is a good assumption, as previous diodes have very high quantum efficiencies.[5] Second, we use 2000cm-1 as the absorption coefficient in Ge at 1550nm. This is the value we obtain by shifting the bulk Ge value to longer wavelengths by

30meV.[8] The shift is due to the bandgap reduction due to biaxial tensile strain in our Ge films, as discussed further in chapter four.

We begin by discussing the frequency response of photodetectors, which is independent of the method of optical coupling. We then discuss the photoresponse of both vertically illuminated and waveguide-coupled devices, followed by saturation effects. We show that waveguide-integrated detectors have significant advantages to traditional vertically illuminated detectors in both photocurrent and saturation effects. The noise characteristics of photodetectors are also important and are covered at the end of this chapter.

Section 2.1 Frequency response of photodetectors

The bandwidth of a detector can be limited by either transit time delay or RC delay, and is independent of the method of optical coupling. For highest-speed operation, detectors should be designed to be transit-time limited.

Section 2.1.1 Transit Time Delay

The transit time is the time it takes a photo-generated carrier to be collected by the detector. All of the generated carriers from one light pulse must be collected before the next light pulse arrives. Otherwise, the detector will not be able to distinguish between individual bits.

Assuming equal electron and hole velocities, the 3 dB bandwidth of vertically illuminated transit-time limited thin detector is given by [9]

$$f_t = \frac{0.45v}{x_d}$$

(2.1)

where v is the carrier velocity and x_d is the depletion width. As expected, this is basically just the carrier velocity divided by the transit distance, multiplied by a constant. Simply stated, it is the time required for the generated carriers to exit the depletion region before the next pulse of incident light generates more carriers. Das has constructed a similar model but considered separate electron and hole velocities, as well as illumination from the electron or hole side of the device.[10] The results are qualitatively the same and show that the response is limited by the hole velocity, which is generally slower than the electron velocity. P-side illumination results in higher frequency response than n-side illumination, because more holes will be generated near the p-side of the device and will therefore have a shorter transit distance. This result has been confirmed by others.[11]

These models are valid only under low power conditions. Under high-power illumination, the electric field due to photo-generated carriers screens the built-in field in the device, thus reducing the carrier velocity and frequency response.[12-15]

In our calculations we use the saturation velocity of 5 x 10⁶cm/s as the carrier velocity. [16] Note that the saturation velocity of electrons and holes is very similar.

Section 2.1.2 RC Delay

The RC delay is related to the product of the load resistance on the circuit and the capacitance of the device. This physical origin of this delay is the charge that must be supplied to the diode to maintain the required bias voltage. The 3dB frequency in the RC limited case is

$$f_{RC} = \frac{1}{2\pi C R_L}$$

(2.2)

16

where R_L is the load resistance and C is the device capacitance. We assume a load resistance of 50Ω in our calculations. We can approximate the diode as a parallel plate capacitor and express the capacitance as

$$C = \frac{\varepsilon A}{x_d}$$

(2.3)

where $\varepsilon = 16 \, \varepsilon_o$ and x_d is the depletion width of the diode.

The total frequency response is given by [17]

$$\frac{1}{f_{3dB}^2} = \frac{1}{f_t^2} + \frac{1}{f_{CR}^2}$$

(2.4a)

or

$$f_{3dB} = \sqrt{\frac{f_{tt}^2 f_{RC}^2}{f_{tt}^2 + f_{RC}^2}}$$

(2.4b)

The overall frequency response will be limited by the slower of the transit time and RC delay. For a given depletion width, the device should be transit-time limited for the highest frequency response.

3dB cutoff frequency for Ge vertical p-i-n diodes

Legend:
- 0.5 um depletion width
- 1 um depletion width
- 2 um depletion width
- 4 um depletion width
- high frequency limit

X-axis: Area (um^2)
Y-axis: 3dB cutoff frequency
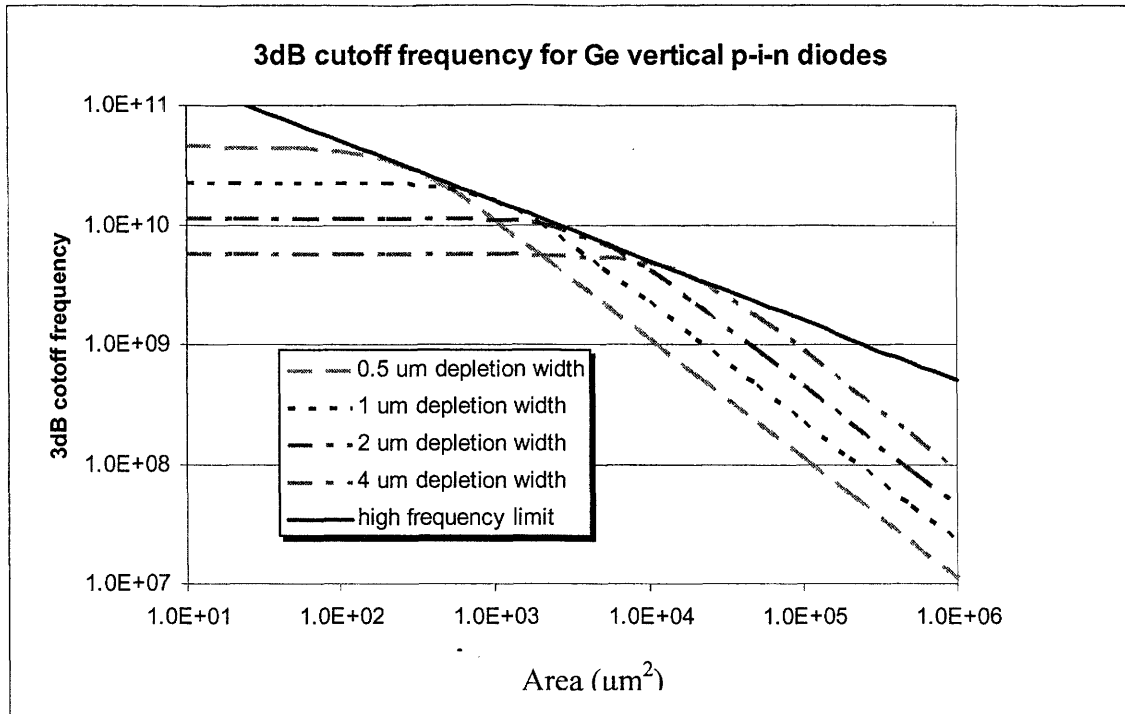
Figure 2.1 3dB frequency response of Ge p-i-n diodes as a function of depletion width

Figure 2.1 shows the 3dB cutoff frequency for vertical p-i-n diodes as a function of area and depletion width. For small detectors, the frequency response is limited by the transit time, and is nearly independent of device size. As the diode area increases a cross-over point occurs at which the RC delay dominates and the cutoff frequency decreases with further increase in size. The area of the cross-over point is found by setting the two terms on the right of equation 2.4a equal and solving for the area.

$$A = \frac{x_d^2}{0.9\pi R v_{sat}\varepsilon}$$

(2.5)

We see that the cross-over area increases with the square of the depletion width. Another interesting observation from figure 2.1 is that for diodes large enough to be limited by RC delay, increasing the depletion width increases the 3dB cutoff frequency.

If equation (2.5) is solved for x_d and the result inserted into equation (2.4b), we get the maximum 3dB cutoff frequency for a given diode area, which is also shown in figure 2.1.

$$f_{3dBMax} = \sqrt{\frac{0.45v_{sat}}{4\pi R \varepsilon A}}$$

(2.6)

If desired, this can be expressed as a function of depletion width by using equation 2.5 to eliminate A in equations 2.2, 2.3 and 2.4b.

Section 2.2 Photocurrent of vertically illuminated p-i-n diodes

The photocurrent is the electrical current produced upon illumination by a light source and is equal to the responsivity times the incident optical power. The responsivity is wavelength dependent and drops off sharply for photon energies below the direct bandgap of the semiconductor used in the diode.

In order to calculate the photocurrent of a vertically illuminated p-i-n photodetector, we first calculate the responsivity and then multiply by the incident optical power. To obtain the responsivity, we first calculate the quantum efficiency of the detector, which is the fraction of photons incident on the detector that contribute to the current. The quantum efficitncy ,η, of a vertical illuminated p-i-n diode can be found in standard textbooks [18] and is given by

$$\eta = (1-r)\delta[1 - \exp(-\alpha x_d)]$$

(2.7)

where r is the reflectivity of the surface, δ is the fraction of electron-hole pairs that contribute to the photocurrent, α is the absorption coefficient of the material (cm^{-1}), and x_d is the absorption depth (depletion width in our case). We assume zero reflectivity

and that all of the generated carriers are collected and contribute to the photocurrent. The absorption coefficient for our strained Ge is approximately 2000cm^{-1}.

The quantum efficiency is related to the responsivity, R, by

$$R = \frac{\eta e}{h\nu} = \eta \frac{\lambda}{1.24} \qquad (2.8)$$

and has units of A/W. λ is the wavelength given in microns. The ratio e/hv converts the optical power in watts to electrical charge in Coulombs.

Combining the above equations, we can express the photocurrent, i_p, of the diode as

$$i_p = \frac{\lambda}{1.24}[1 - \exp(-\alpha x_d)]AI_o \qquad (2.9)$$

where A is the area and Io is the incident power.

For our calculation we assume an incident optical power density of 1 W/cm^2, which is equivalent to -10dBm optical power incident on a 100μm x 100μm diode, and assume an incident wavelength of 1550nm. Figure 2.2 shows the photocurrent as a function of area and depletion width.
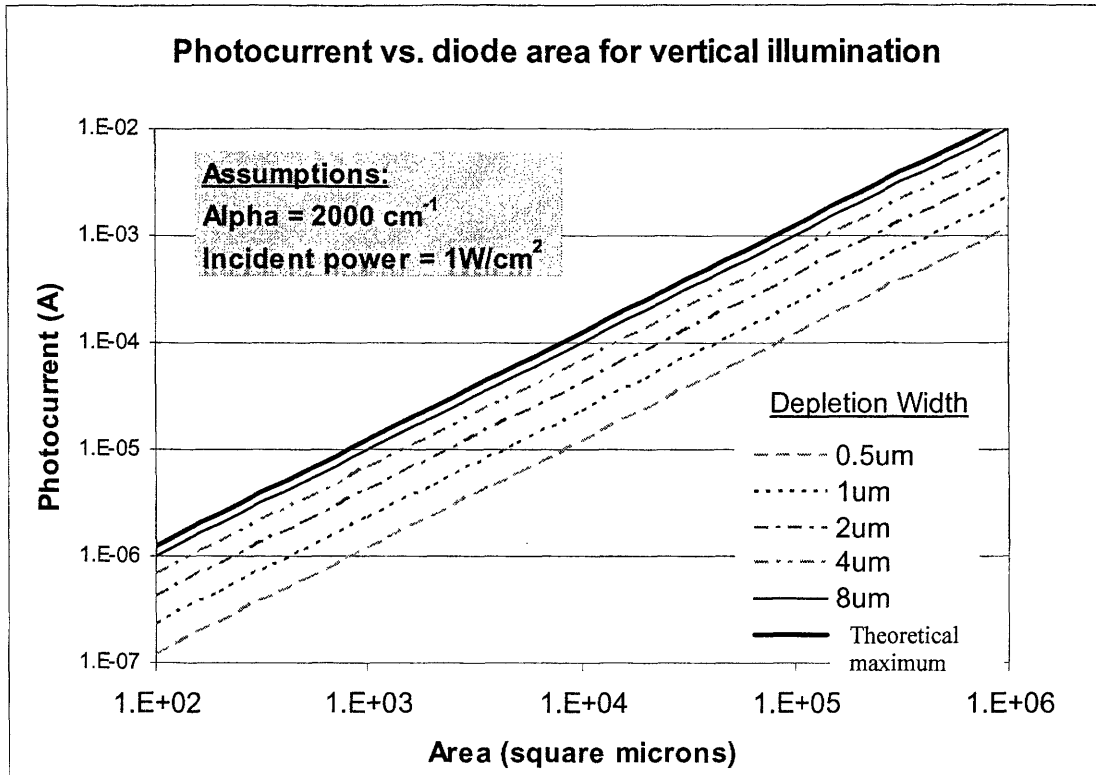
Figure 2.2 Photocurrent as a function of depletion width and diode area for vertically illuminated p-i-n photodetectors

If an application requires a given photocurrent, we can see that the required area increases with decreasing depletion width. For given optical power density and bandwidth requirements, figures such as Figure 2.1 and Figure 2.2 can be generated and used to find the ranges of diode areas and depletion widths satisfying these requirements.

For traditional detection schemes with light incident onto a vertical p-i-n structure, a trade-off exists between the bandwidth and efficiency of the device. If the depletion width is very thin (for highest frequency response), then the absorption length will be short. Not all of the all of the incident light will be absorbed, thus reducing the efficiency. On the other hand, if the depletion width is wide for maximum absorption,

the frequency response will be slower. This tradeoff has led to a common figure of merit

known as the bandwidth-efficiency product.

For a waveguide integrated detector, the light travels parallel to the surface of the

diode and is coupled in evanescently. The rate at which the light is coupled into the

detector (and the amount of light scattered) depend upon the specific design, but in theory

it is possible to couple all of the light into the diode. The use of impedance matching

layers between the waveguide and detector can be used to control the coupling length.

[19, 20] Indeed, 90% coupling efficiencies have been achieved in as little as 20μm. [21]

Figure 2.3 shows a vertical illuminated p-i-n detector, as well as a waveguide-integrated

scheme.
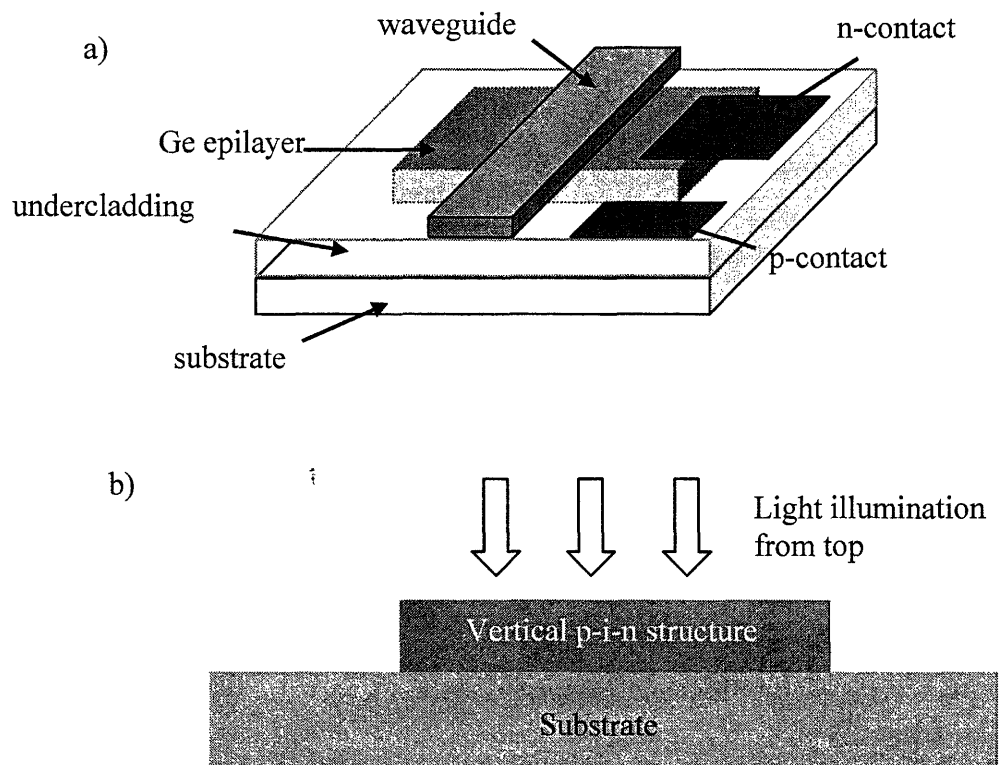
Figure 2.3 a) waveguide-integrated coupling scheme b) vertial illumination scheme

One primary advantage to waveguide-integrated detectors is that the absorption efficiency is not limited by the film thickness. If we consider the detector as a waveguide, then we are simply considering the case of coupling between two waveguides, where one of the waveguides is absorbing. The thickness of the detector (or absorbing waveguide) does not prohibit 100% coupling efficiency. An important consequence of this is that the photoresponse is not limited by the depletion width, as in vertically integrated diodes. Therefore, the upper limit on responsivity is the theoretical responsivity, regardless of the depletion width of the p-i-n detector. This is shown in Figure 2.2 by the thick black line. The improvement over vertically illuminated diodes with diminishing depletions widths is apparent. The minimum coupling length to absorb all the light will be at least equal to the absorption length of light in the material, which is $1/\alpha$. Waveguide-detector coupling is discussed further in section 2.4.

The maximum photocurrent for a waveguide-coupled detector is simply the product of the theoretical responsivity multiplied by power in the waveguide.

$$i_p = \frac{\lambda}{1.24} P_{waveguide}$$

(2.10)

Section 2.3   Diode Saturation

As generated electrons and holes are swept in opposite directions, an electric field is generated between them. This electric field opposes, and therefore partially screens, the field due to the applied reverse bias (and built in field present in the diode). If too many carriers are generated, this screening field becomes large enough to slow the removal of carriers from the depletion region, thus reducing device performance. This condition is called saturation.

In this section we attempt to quantify the point at which saturation will begin to occur in photodetectors. We will show that diodes with thick depletion regions saturate at lower optical power intensity than diodes with thin depletion regions, due to the longer transit times of generated carriers. This is a further advantage of waveguide integrated detectors, where very thin diodes can be made that still have high responsivity. This means that waveguide-integrated detectors not only simultaneously allow high speed and high responsivity, they also have higher saturation thresholds than vertically illuminated diodes.

In analyzing the onset of saturation in p-i-n photodiodes, we will first consider the case of vertical illumination and then waveguide integration.

Section 2.3.1   Saturation in vertically illuminated photodetectors

Our goal is to calculate the electric field due to the generated carriers and compare it to the background field present in the diode. Because the distribution of carriers is not uniform, the screening electric field is also not uniform. Furthermore, the reduction in device performance at which we define the onset of saturation is somewhat arbitrary and depends on the specific application. However, the generated screening field must be much less than the applied field. In calculating the generated field, we make a very conservative estimate by calculating the field that would be present if all of the generated carriers present in the depletion region were placed at the edge of the depletion region and follow an approach similar to that of Lucovsky [22] in making our calculation. Because we are assuming that the electrons and holes are completely separated at opposite ends of the diode, we are overestimating the generated field.

24

For non-saturated operation, the applied electric field must be much less than the generated field.

$$E_{app} >> E_{gen} \qquad (2.11)$$

The applied field is given by

$$E_{app} = \frac{V}{x_d} \qquad (2.12)$$

where V is the applied voltage and xd is the depletion width. Here we assume the field is constant across the depletion width. If the intrinsic region of the p-i-n diode is large compared to the depletion widths at the edges on the n and p side, this is a reasonable approximation.

The generated field is given by Poisson's equation,

$$E_{gen} = \frac{\rho}{\varepsilon} \qquad (2.13)$$

where ρ is the generated charge (the greater of either the electrons or holes) present in the depletion width. This charge is given by

$$\rho = e \int g(x) t_{trans}(x) dx \qquad (2.14)$$

where e is the electronic charge, g(x) is the generation of carriers due to absorbed light, and $t_{trans}(x)$ is the transit time required for a carrier generated at position x to be swept out of the depletion region. x is the distance from the surface of the diode and the integral is over the entire depletion width.

The carrier generation, g(x), is

$$g(x) = -\frac{\lambda}{1.24*1.6x10^{-19}} \frac{dI}{dx} = -\frac{\alpha \lambda I_o}{1.24*1.6x10^{-19}} \exp(-\alpha x) dx \qquad (2.15)$$

25

The absorption coefficient, α, is wavelength dependent, and the wavelength energy must be equal to or greater than the band gap. The transit time of generated carriers, $t_{trans}(x)$, is

$$t_{tras\_e}(x) = \frac{x}{v_{sat}}$$

(2.16a)

$$t_{trans\_h}(x) = \frac{x_d - x}{v_{sat}}$$

(2.16b)

for electrons and holes, respectively. We have assumed that the light is incident on the n-side of the device, which is the case for diodes we have fabricated.

Substituting into equation 2.14 and carrying out the integral over the entire depletion width yields the total number of electrons and holes in the depletion width.

$$\rho_e = \frac{\lambda I_o}{1.24 \alpha v_{sat}} \left[1 - e^{-\alpha x_d} (1 + \alpha x_d) \right]$$

(2.17a)

$$\rho_h = \frac{\lambda I_o}{1.24 \alpha v_{sat}} \left[x_d \alpha - 1 + e^{-\alpha x_d} \right]$$

(2.17b)

Note that as the depletion width become much larger than the absorption length, these become

$$\rho_e = \frac{\lambda I_o}{1.24 \alpha v_{sat}}$$

(2.18a)

$$\rho_h = \frac{\lambda I_o x_d}{1.24 v_{sat}}$$

(2.19b)

The total number of electrons present in the depletion region becomes independent of the depletion width and varies inversely with the absorption length and saturation velocity. The electrons are swept back towards the surface of the diode, so increasing the depletion width has no effect on the transit distance of generated carriers. Once the depletion width is large enough to absorb all of the light, the number of carriers reaches a

maximum. The $1/\alpha$ term can then be thought of as the average transit distance of an electron. The holes, on the other hand, must travel to the opposite end of the depletion width as the electrons. Increasing the depletion width increases the transit distance for holes. As the depletion width becomes much greater than the absorption length, the number of carriers present becomes proportional to the depletion width.

Under the assumption of equal electron and hole velocities, which we have made here for simplicity, the number of holes will always be greater than the number of electrons (for n-side illumination). We therefore use the number of holes in calculating the generated electric field, as this will yield a higher value. In this way we make a more conservative estimate of the light intensity necessary for diode saturation.

Combining equations 2.11, 2.17, and 2.18, we reach the following condition for non-saturation of a vertically illuminated p-i-n diode.

$$I_o << \frac{1.24\alpha v_{sat} V \varepsilon}{\lambda x_d (x_d \alpha - 1 + e^{-\alpha x_d})} \qquad (2.20)$$

This condition must be satisfied in order for the generated field to be much less than the applied field. If the two sides of the equation are equal, then the generated field is equal to the applied field. If we somewhat arbitrarily say that we will allow the generated field to be no more than 10% of the magnitude of the applied field, then we demand that I_0 be no more than 10% of the right side of the equation. Figure 2.4 shows the total optical power incident on a diode under these conditions as a function of diode size and depletion width.

Optical power at onset of saturation in a vertically illuminated p-i-n detector

Optical power (W)

- — — 0.5um
- - - - 1um
- - - - 2um
- — - 4um
- ——— 8um

1.E+02
1.E+01
1.E+00
1.E-01
1.E-02
1.E-03
1.E-04
1.E-05
1.E-06
1.E-07
1.E-08

1.0E+00   1.0E+01   1.0E+02   1.0E+03   1.0E+04   1.0E+05   1.0E+06

Area (square microns)
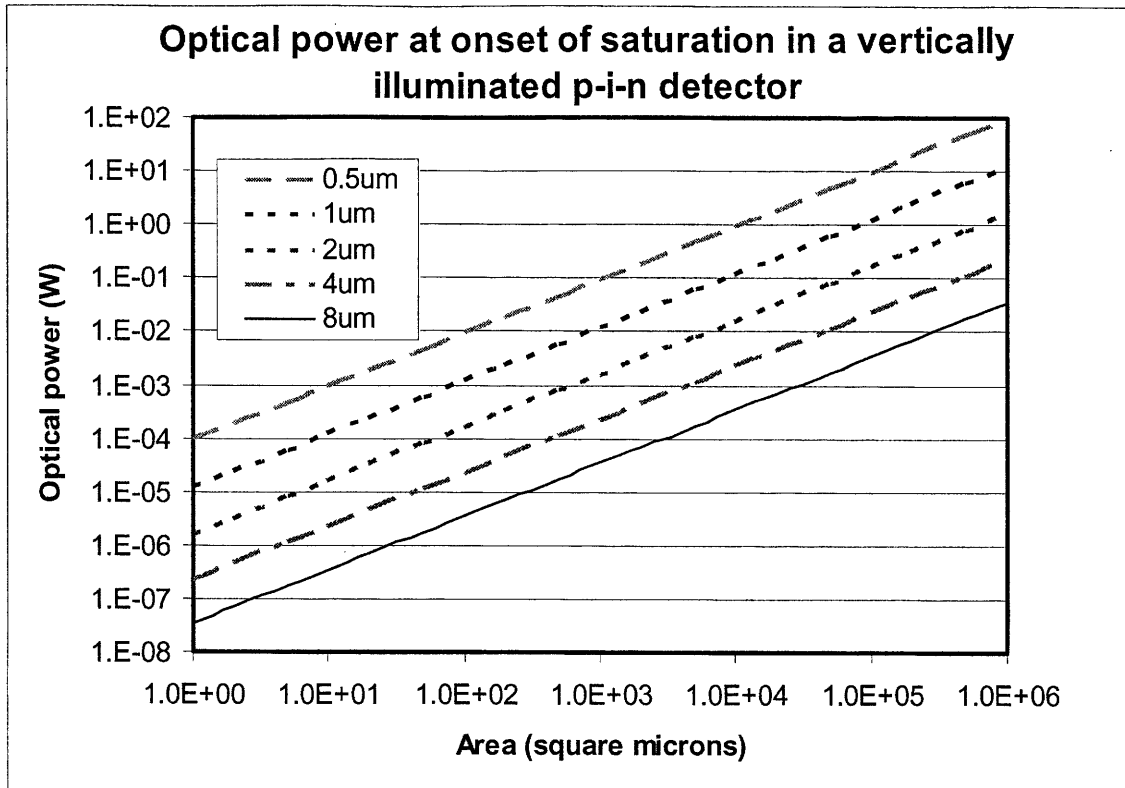
Figure 2.4 Optical power at onset of saturation in a vertically illuminated p-i-n photodetector for different depletion widths

The maximum optical power increases linearly with diode area and decreases substantially with increasing depletion width. Two reasons exist for the decrease in maximum optical power with increasing depletion width: 1) As the depletion width decreases, less of the light is absorbed converted into electron-hole pairs. 2) As the depletion width decreases, the average time for carriers to be swept out of the depletion width decreases.

By inserting the maximum optical power intensity into equation 2.9, we can compute the maximum photocurrent that can be generated from a vertically illuminated p-i-n diode. Figure 2.5 shows this maximum photocurrent in Ge as a function of diode area and depletion width for a detector bias of 2 Volts (including built in bias).
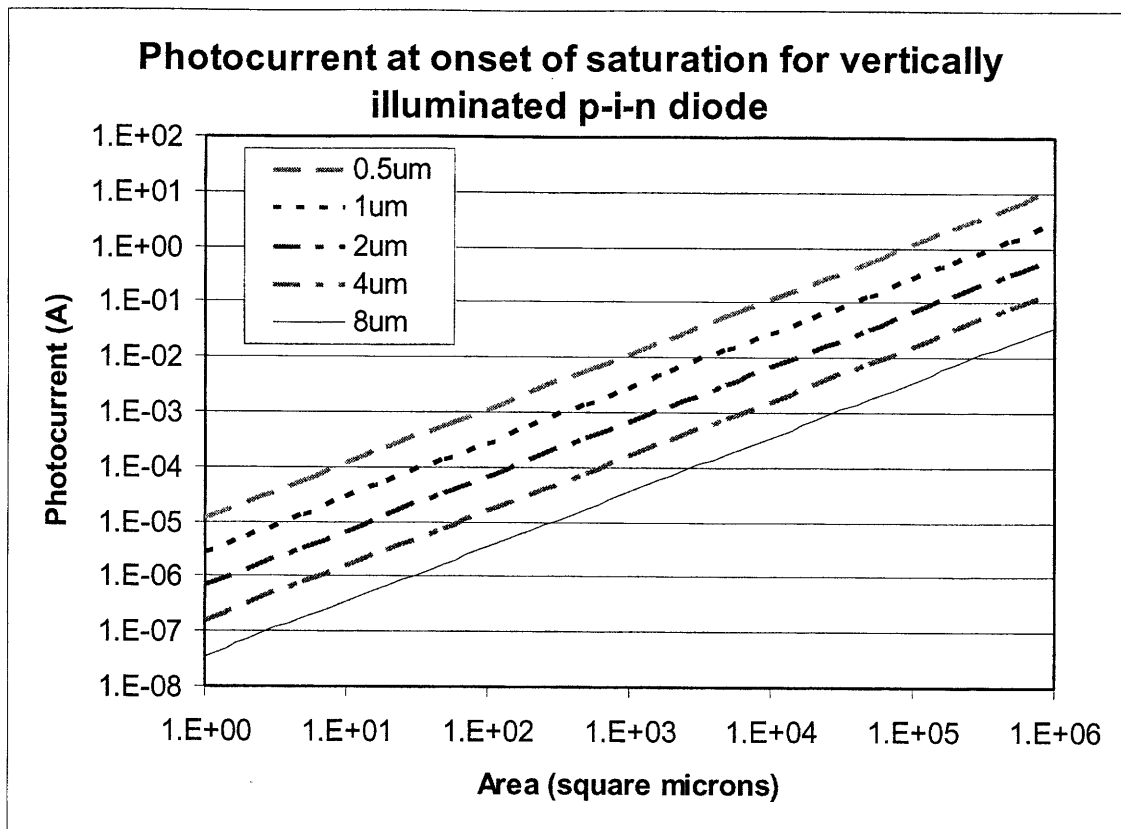
Figure 2.5 Photocurrent at onset of saturation for vertically illuminated p-i-n detector

Section 2.3.2 Saturation in waveguide-coupled photodetectors

We follow the same approach as before in calculating the point of optical

saturation in a waveguide-coupled photodetector, but with one significant difference. In

the waveguide coupled case, we no longer know the generation rate as a function of

distance in the diode, as this will be dependent on the specifics of the optical coupling.

We therefore make the conservative assumption that all of the carriers are generated at

the surface of the diode and must transit the entire depletion width. This will

overestimate the number of carriers present in the diode, and therefore the generated

field, because the average transit time of carriers is overestimated.

29

At first thought we might think that due to the overestimation of the transit distance, the saturation point will be at a lower optical power density than in the vertically-illuminated case. However, this is not the case. On the contrary, because all of the light is absorbed at the surface, a high responsivity can be achieved with a very thin diode. The average transit time is much shorter than for the thick vertically illuminated diode with the same responsivity. Because of the shorter transit time, the number of carriers present in the depletion width is less in a waveguide-coupled device than in a vertically illuminated one with the same photocurrent. The lower carrier density translates to a lower generated field and correspondingly higher saturation point.

With our assumption that all of the light is absorbed at the surface of the diode, equations 2.15 and 2.16 become

$$g(x) = \frac{\lambda}{1.24 * 1.6 x 10^{-19}} I_o \delta(0)$$

(2.21)

$$tt(x) = \frac{x_d}{v_{sat}}$$

(2.22)

respectively, where $\delta(0)$ is the delta function evaluated at x=0. Using equations, 2.20, 2.21, and 2.22 we reach the following condition for non-saturation of a waveguide-coupled vertical p-i-n photodetector:

$$I_o << \frac{v_{sat} V \lambda \varepsilon}{x_d^2}$$

(2.23)

The saturation power varies linearly with the carrier velocity and applied voltage and inversely with the square of the depletion width. We can again define the onset of saturation the point at which the generated field is 10% of the background field and compute the total power incident on a diode, as shown in Figure 2.6.
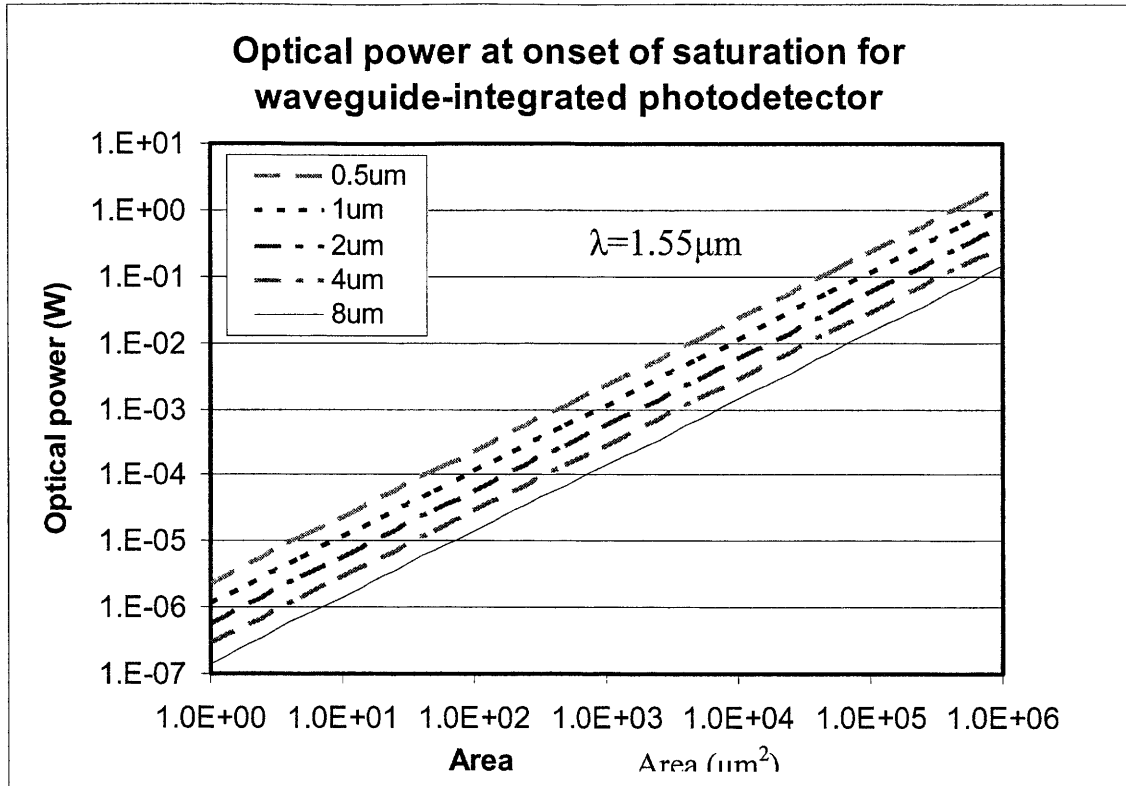
Figure 2.6 Optical power at onset of saturation for integrated photodetector

The photocurrent at the onset of optical saturation is easily computed assuming ideal

responsivity and is shown in Figure 2.7.

It should be remembered that although the diode is in saturation, the responsivity

will still be low in a thin, vertically illuminated detector. For most applications,

responsivity must be high. For thin detectors, waveguide integration must then be

employed.
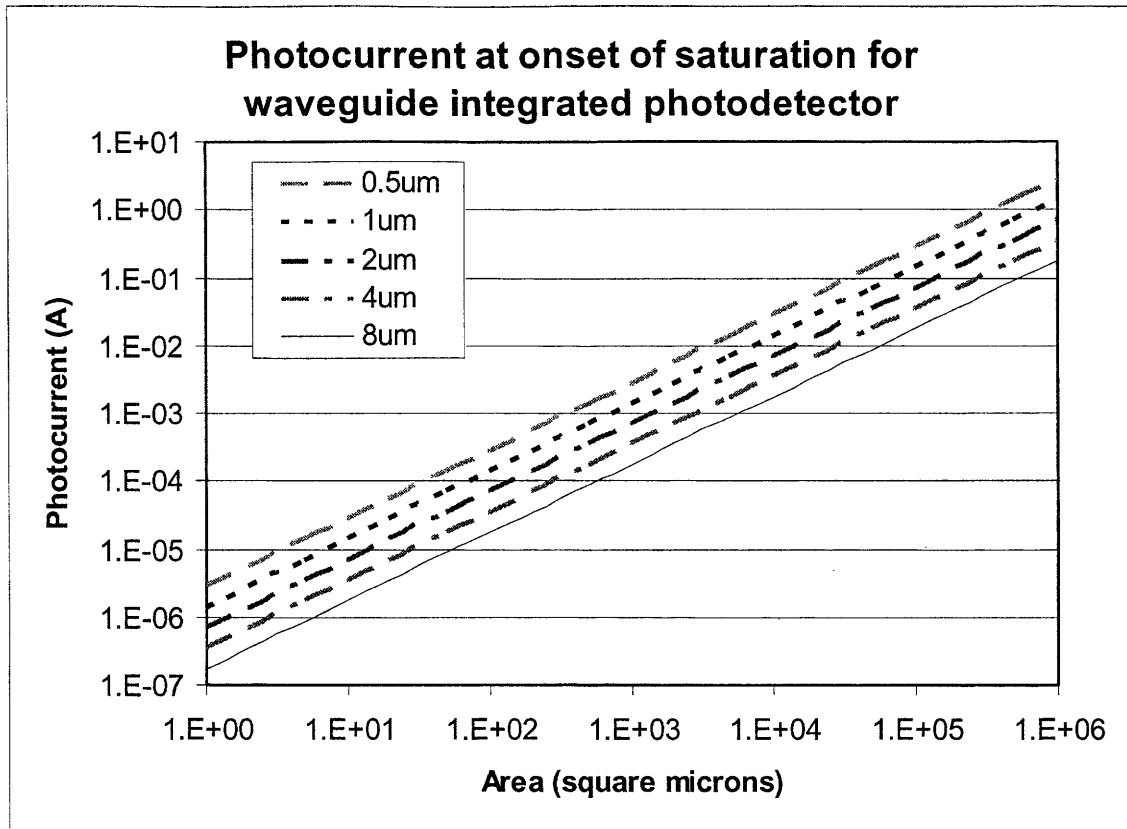
Figure 2.7 Photocurrent at onset of saturation in an integrated p-i-n photodetector

Section 2.3.3   Allowable design space for Ge p-i-n detectors

From the previous discussion it is clear that the diode cannot be too large or too small. If it is too large, the RC delay will limit the frequency response. If it is too small, optical saturation will not allow for enough photocurrent. We are now in a position to determine the allowable design space, given the performance requirements.

We consider the case of a p-i-n detector with a minimum 3dB bandwidth requirement of 10 GHz. The depletion width must be chosen such that the transit-time limited bandwidth is larger than this value. We choose in this example a depletion width

32

of 1μm, which from the previous discussion has a 3dB bandwidth of 22 GHz. For areas above 5000μm², or about 70μm in diameter, this device will be too slow.

We also need a minimum photocurrent level. If the noise of our detector is approximately 1μA and we have a signal to noise requirement of 14 (for 10^{-12} BER) [23], then the diode must be at least a few tens of square microns in area to absorb generate the required current without becoming saturated.

This allowable range is illustrated below in Figure 2.8.
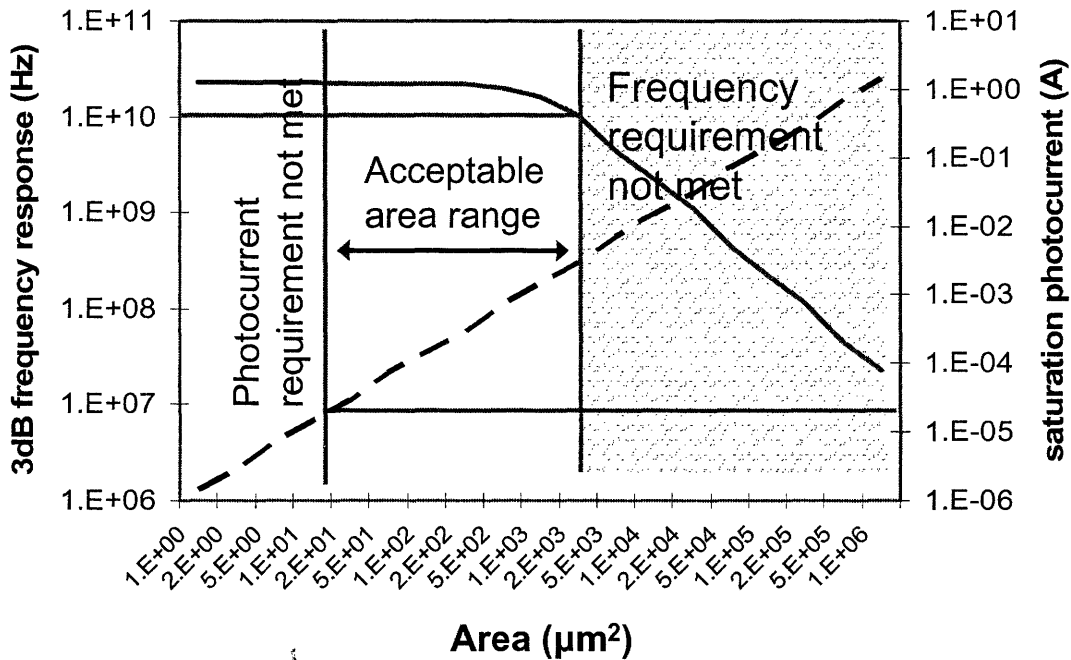
Figure 2.8 Allowable design space for 10 GHz Ge photodetector with 1 micron depletion width

Section 2.4   *Advantages to integration*

Based on the previous discussion, we ask what advantages, if any, integration has over vertical integration. Our important figures of merit are the bandwith, responsivity, and saturation photocurrent.

The primary benefit of waveguide integration is the simultaneous achievement of both high bandwidth and high responsivity. One common photodetector figure of merit, known as the bandwidth-efficiency product, illustrates the inherent tradeoff present in these performance measures for vertical illumination. The band-width efficiency product is obtained by multiplying equations 2.1 and 2.7. If we assume full no reflection from the surface and 100% internal quantum efficiency this becomes

$$bandwidth * efficiency = \frac{0.45 v_{sat}}{x_d} \left(1 - e^{-\alpha x_d} \right) \tag{2.24}$$

The first term is the frequency response, which increases as the depletion width shrinks. However, the second term, which is the efficiency, decreases as the depletion width shrinks. If the depletion width becomes large, the opposite happens. The frequency response drops, but the efficiency approaches unity. The advantage of waveguide integration is that it decouples the dependence of efficiency on bandwidth. The efficiency can be largely independent of the depletion width.

Another benefit of integration is that it also offers the potential for very small photodetectors, as the size will be controlled by the waveguide dimensions and coupling scheme. As diode sizes shrink, saturation becomes an important issue that we must also consider.

Waveguide integration offers clear advantages over vertical illumination in terms of saturation characteristics, because a thinner depletion width allows for higher photocurrent density, as shown in equations 2.20 and 2.23. If high responsivity is important, then vertical illumination is at a disadvantage, due to the need for a thick depletion width.

Section 2.5 *Feasibility of waveguide integration*

Waveguide-integration offers clear advantages to vertical illumination. We now discuss whether or not it is feasible. We ask the following questions regarding waveguide coupling:

1) Is it possible to couple all of the light from a waveguide to a detector?

2) Will there be a confined optical mode in the detector?

3) As the detector becomes thin, how will this affect the absorption length of the optical signal?

Although the answer to the first question is in principle yes, how to do it is a very open and difficult question. No theoretical barriers exist that prohibit the coupling of light from a waveguide to a Ge detector. In fact, waveguide-coupled detectors have been successfully demonstrated in III-V sytems. Our situation is more difficult, though, due to the higher index contrast between Ge and potential waveguide candidates, such as Si and Si_3N_4. Designing and fabricating a structure that will allow for coupling of light into a Ge detector with minimal losses from scattering and reflection may present significant challenges. However, at present there is no reason to believe that a satisfactory solution will not be found. Finding the solution lies outside the scope of this thesis.

With regards to the second and third questions, we will give very definitive answers. There will be a confined optical mode, meaning that light can in principle be coupled to the detector. We will calculate the mode for a general one-dimensional structure and quantitatively show how the absorption length of the optical signal is affected by the thickness of the Ge detector.

Rigorously calculating the equilibrium mode of a waveguide on a detector requires solving Maxwell's equations for a two-dimensional index profile representing the cross-section of the device. The two-dimensional index profile can be reduced to a one dimensional problem resulting in effective indices of refraction of the layers. Variations in the refractive index and thickness of layers will result in changes in the resulting optical mode. We have calculated the optical mode for a one dimensional structure consisting of a Si substrate, Ge detector layer, Si_3N_4 waveguide, and SiO_2 top cladding. The Ge layer thickness was varied between 0.2 and 2.0 microns and an absorption coefficient of 2000 cm^{-1} was used. This value for the absorption coefficient is obtained by shifting the absorption data for bulk Ge from Braunstein et al. [8] to lower energies by 30meV. This is the reduction in direct transition energy present in our strained Ge films and is covered in more detail in chapter four. This shift in absorption to lower energies (or longer wavelengths) is in agreement with the shift in responsivity we have observed in our Ge diodes, which is covered in chapter five. Details of calculating the optical mode are not covered here but are covered in several texts [18, 24, 25]. Matlab was used to carry out all computations, and the code used is found in Appendix A.

It is important to note that in order for light to couple from the waveguide to the detector, the modes in each of these structures must be properly matched. In other words, the propogation vectors of the modes must be similar in order for light to couple from the waveguide to the detector. This is an additional design constraint that must be taken into account.

Figure 2.9 shows the index profiles and first order optical modes for structures

with Ge thickness layers of 200nm and 500nm. For the thinner layer, more of the optical

mode penetrates into the Si substrate. More of the optical mode is contained in the Ge

layer as it becomes thicker. Because Ge has the highest index of refraction of any

material in the structure, there will always be a confined optical mode containing the Ge.
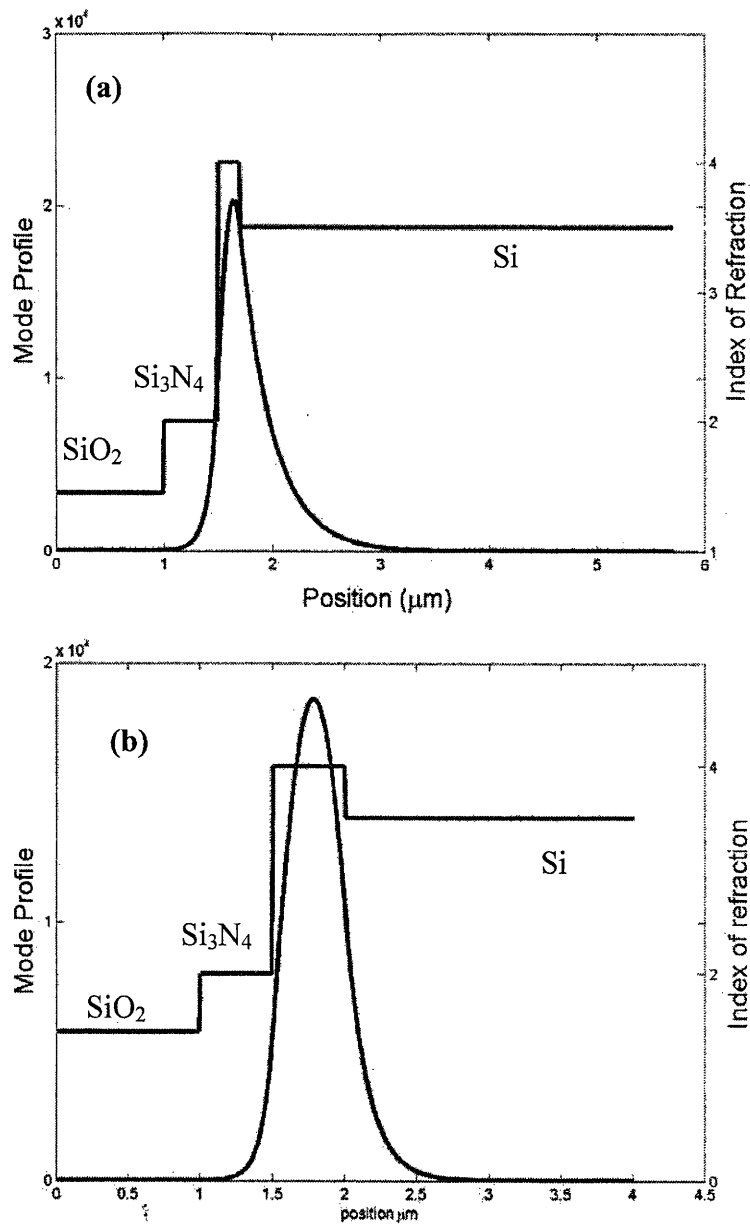
Figure 2.9 Mode profiles for 1D waveguide detectro structure with Ge thickness of a) 200nm and b) 500 nm

The effective index of the one-dimensional structure was also computed, and the imaginary component of the effective index was used to compute the absorption loss in dB/cm resulting from the absorption of the light by the Ge. (The imaginary component

of the effective index is found by multiplying the fraction of the optical power present in the Ge by its absorption coefficient.) This absorption loss is due to absorption of light by the Ge photodetector and can be used to calculate the length of detector needed to absorb the light. For example, for a Ge thickness over 0.5 microns, the absorption loss is approximately 0.85dB per micron. To absorb 90% of the light would require a minimum detector length of 12 microns, assuming the light is effectively coupled from the waveguide to the Ge.

The important conclusion we can draw from this is that if the coupling is efficient, the required detector length will be on the order of a few tens of microns at most. Such a device will have a small area, allowing the device to be transmit time limited and operate at high frequencies. Also, only 0.5 microns of Ge are required to have a well confined optical mode in the detector, and from Figure 2.1 we see that a 0.5 micron depletion width allows for a 3dB cutoff frequency of 45 GHz. We can conclude that waveguide integration offers the potential for very high performance Ge photodetectors.
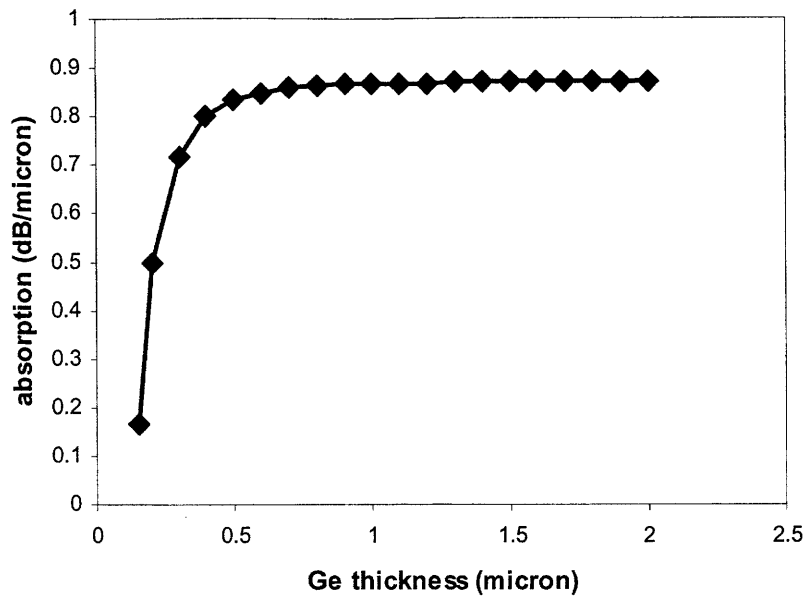
Figure 2.10 Absorption in 1D waveguide detector structure as a function of Ge layer thickness

Section 2.6 *Photodetector noise and system performance*

We now discuss the effects of photodetector noise to the photoreceiver sensitivity, which is the minimum optical power required to maintain a specified bit error rate (BER). Noise occurs in many areas of a communication system, but it is of particular concern for photoreceivers, because the strength of the incoming signal is very weak. Furthermore, because the sensitivity of the photoreceiver determines the minimum acceptable input power, it has important implications on other aspects of the system, such as the maximum signal transmission distance before termination.

Much has been written on photoreceiver sensitivity in several books [26-28], so only the main conclusions and their implications will be presented here. A photoreceiver consists of a photodetector and a preamplifier. Three main types of preamplifiers exists: low-impedance (LZ), high-impedance (HZ), and transimpedance (TIA). The LZ

preamplifier is the most straightforward, but does not have high sensitivity. On the other

hand, the HZ preamplifier has very high sensitivity, but the front-end bandwidth is less

than the signal bandwidth, requiring that the input signal be integrated and equalization

techniques be used for compensation. The TIA largely overcomes the drawbacks of the

HZ preamplifier, although it is not quite as sensitivive as the HZ [29]. In our discussion

we will use as an example the transimpedance amplifier, which is widely used in

industry. Figure Figure 2.11 shows a simple photoreceiver circuit design utilizing a

transimpedance amplifier. The bond capacitance and resistance, C_b and R_b, are shown.
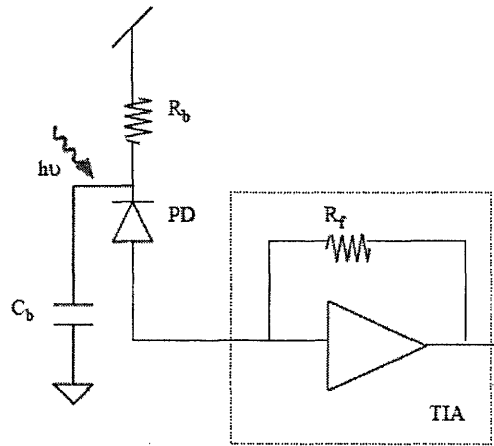
Figure 2.11 Equivalent circuit of photoreceiver utilizing a TIA

Assuming ideal input sensitivity and a perfect extinction ratio of the signal, the

photoreceiver sensitivity can be written as

$$Sensitivity(dBm) = 10Log_{10}\left(\frac{I_{tot} * 2Q * 1000mW / W}{2R}\right) \qquad (2.24)$$

where I_{tot} is the rms input noise, Q is the signal to noise ratio, and R is the responsivity of

the photodiode. $2Q = 14.1$ for a BER of 10^{-12} [23], and we use 0.8A/W as the

responsivity, which is the theoretical responsivity for Ge photodetectors operating at 1.55 μm.

The input noise is composed of noise from several sources: shot noise (I_s), thermal noise (I_t), generation-recombination noise (I_{gr}), and 1/f noise. The TIA input noise (ITIA), usually the dominant source of noise, has been included in the thermal noise in the following discussion. Other sources of noise may also be present. As the noise sources are uncorrelated, they must be summed as rms values rather than a linear summation. The total noise is given as

$$I_{tot}^2 = I_s^2 + I_t^2 + I_{gr}^2 + I_{1/f}^2 + ... \qquad (2.25)$$

Shot noise occurs in all photodetectors and is due to the fact that individual photoelectrons are created at random intervals as photons are absorbed. As a result, the signal has some variation with time. Shot noise is present in the current generated by the optical signal, I_p, by background radiation, I_b, and the dark current, Id. Each of these sources is random in nature, so they contribute to the total shot noise by a mean square current variation of

$$I_s^2 = 2e(I_p + I_b + I_d)B \qquad (2.26)$$

where e is the electron charge and B is the bandwidth. Shot noise increases with both current and bandwidth and is at a minimum when only dark current exists.

Thermal noise, also known as Johnson or Nyquist noise, is caused by randomness in carrier generation or recombination due to thermal excitation in a conductor. It results in fluctuations in the resistance of the photodetector and any resistor in series with the detector, such as the junction resistance (R_j), series resistance (R_s), the load resistance

(R_l), and the input series resistance of the amplifier. The series resistance can usually be neglected, so the thermal noise is given by

$$I_t^2 = 4kT_A B \left(\left(\frac{1}{R_j} \right) + \left(\frac{1}{R_l} \right) + \left(\frac{1}{R_i} \right) \right)$$

(2.27)

where k is Boltzmann's constant, B is the bandwidth, and T_A is chosen to include the equivalent noise power of the amplifier following the diode. The amplifier noise temperature T_A is related to its "noise figure" F by

$$F = 1 + \frac{T_A}{290}$$

(2.28)

The noise contribution of the TIA is ~1 μA in current systems and is generally the dominant source of noise.

Generation recombination noise is due to the randomness in the generation and recombination of individual carriers and can be shown to be equal to [30]

$$I_{gr} = 2I \left(\left(\frac{\tau B}{N} \right) \left(1 + (2\pi f \tau)^2 \right) \right)^{\frac{1}{2}}$$

(2.29)

where I is the average current, τ is the carrier lifetime, B is the bandwidth, N is the total number of free carriers, and f is the frequency at which the noise is measured.

1/f noise is present in biased conductors, and although its origin is not well understood, it is thought to be connected to the imperfect conductive contact at detector electrodes [26]. It has been empirically shown to follow a curve of 1/fβ, where β is a constant varying between 0.8 and 1.2. Poor Ohmic contact increases this noise, but it is not known if any particular contact will eliminate this noise. The expression for the noise current is empirically given as

43

$$I_f = \alpha \left(\frac{iB}{f^\beta} \right)^{\frac{1}{2}}$$
(2.30)

where α is a proportionality constant and i is the current through the detector. Note that this noise becomes increasingly smaller as we go to higher frequencies.

As previously stated, the TIA input noise is ~1μA and is the dominant source of thermal noise in a modern system. Generation recombination and 1/f noise are small and can be neglected. The relative magnitude of shot noise will depend on the leakage current of the diode. If the leakage current is very small, as is the case for III-V detectors, the shot noise is much smaller than the TIA input noise and can be neglected. However, as the leakage current grows to the shot noise becomes comparable to the TIA input noise. Ensuring that the leakage current is low in a Ge photodetector is important in order to ensure that the shot noise is not the limiting noise factor. As long as the shot noise is much lower than 1μA the TIA input noise will dominate and determine the optical sensitivity. Figure 2.12 shows the leakage current as which the shot noise becomes equal to 0.1μA as a function of bandwidth. For a 10GHz bandwidth, the diode leakage current must be below 30μA. In chapter five we demonstrate Ge photodiodes with leakage currents satisfying this requirement. We can therefore conclude that Ge photodetectors can be made that will satisfy the noise requirements in modern photoreceivers for high-speed detection.

Leakage Current Requirement vs. Bandwidth
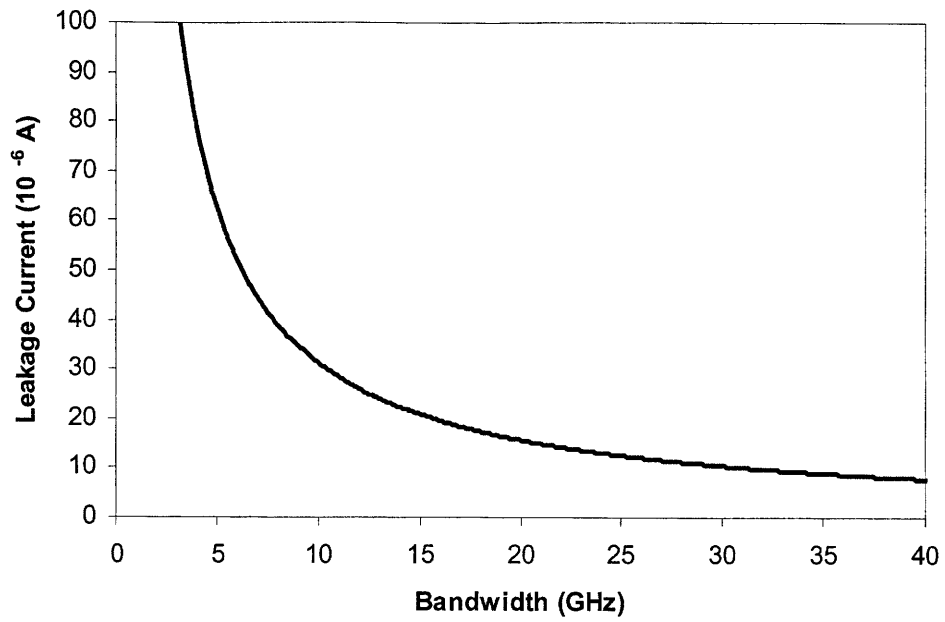
Figure 2.12 Leakage current requirement such that shot noise is 0.1µA as a function of bandwidth

Chapter 3:   Ge and SiGe UHV/CVD Epitaxy

This chapter discusses two topics: 1) the growth of high quality selectively grown Ge mesas and 2) high Ge content SiGe blanket films. Both are grown directly on Si substrates by UHV/CVD. The ability to grow selectively offers advantages for integration with other devices and allows for improved dislocation density reduction, as compared to blanket films. The growth of high Ge content SiGe films also allows for bandgap tuning near 0.8eV, or 1.55µm.

We begin with a brief review of prior work in Ge and SiGe epitaxy, setting the stage for the present work. We then show how we have advanced on previous work in two areas. First, we show the achievement of high quality selectively grown Ge mesas directly on Si substrates. Second, we show the achievement of high Ge content SiGe films grown directly on Si substrates. P-i-n diodes fabricated from these mesas and blanket films are presented in chapter 5.

Section 3.1   Prior developments in Ge and SiGe epitaxy

The development of high quality Ge and SiGe epitaxy has been pursued for a variety of reasons. Perhaps the most important reason is the ability to tailor the bandgap, while still working with Si CMOS technology. Ge is a completely miscible allow with Si, allowing for bandgap engineering over the range of 0.66 to 1.12eV. Furthermore, the addition of Ge to Si does not pose problems to further CMOS processing. Bandgap engineering can be useful in electrical devices, such as the base of a SiGe heterojunction bipolar transistor (HBT), or optical devices, such as the photodetectors and modulators discussed in this thesis. SiGe alloys can also be used to tailor the strain in a material,

which in turn affects the mobility of carriers. The development of strained Si for higher speed CMOS devices is currently an active area of research. Strain also affects the band gap, and the strain-induced bandgap reduction in SiGe alloys has been calculated by People [31].

The primary difficulty in SiGe epitaxy is the 4% lattice mismatch between Si and Ge. This lattice mismatch must be accommodated either through strain or dislocations. The critical thickness for relaxation through introduction of dislocations depends on the lattice mismatch of the alloy, but is only a few atomic layers for pure Ge on Si. [32] Upon relaxation, dislocations are introduced at the interface in the growth plane (misfit dislocations). Because a dislocation cannot terminate within the bulk, it must terminate at the edge or surface of a material, or else close upon itself, forming a closed loop. Consequently, many dislocations leave the growth plane and propogate through the film to the film surface (threading dislocation). These threading dislocations degrade device performance by reducing carrier lifetimes.

The field of SiGe epitaxy is almost thirty years old. Kasper et al. [33] used CVD to achieve the first successful growth of a SiGe heterostructure on Si in 1975. Masini, et al. have reviewed the development of this field [34]. The developments of ultra high vacuum chemical vapor deposition (UHV/CVD) and molecular beam epitaxy (MBE) in the 1980's aided the development of SiGe epitaxy [35]. The first pseudomorphic growth of SiGe on Si by MBE was achieved by Bean et al. in 1984 [36]. In 1986 Meyerson achieved the first low temperature UHV/CVD heteroepitaxy of SiGe on Si [37].

The deposition of pure Ge epilayers is of interest for near infrared (NIR) photodetectors for operation at 1.3 and 1.55μm, and also for a suitable substrate for

deposition of GaAs on Si. In one attempt, pure Ge epilayers were obtained by depositon of amorphous Ge on si, followed by annealing for crystallization [38]. Heteroepitaxy of pure Ge on Si by CVD was achieved by Keuch, et al [39]. They also compared epilayers grown by physical layer deposition (PVD) and CVD, with the best CVD samples exhibiting dislocation densities of $4x10^9 cm^{-2}$ [40]. Cunningham and coworkers demonstrated the first low temperature Ge buffer on Si by UHV/CVD [41]. Other groups have also studied heteroepitaxy of Ge on Si by several methods, including evaporation [42], CVD [40, 43], MBE [44-49], and rapid thermal chemical vapor deposition (RTCVD) [50]. One problem with direct epitaxy of Ge or SiGe alloys is the high dislocation density. Due to the lattice mismatch, SiGe alloys with Ge concentrations greater than 30% generally have dislocation densities of 10^{11} - $10^{12} cm^{-2}$ [51].

In their RTCVD work, Ozturk and coworkers showed that Ge CVD is surface reaction limited at temperatures below 450C and mass transport limited at higher temperatures [50]. Cunningham and coworkers have shown similar results in UHV/CVD [41]. They also report that growth is planar at growth temperatures of 350C and below but that islanding occurs at 375C and above. Luan has grown high quality epitaxial films by first growing a low temperature buffer layer and then raising the temperature to grow the remainder of the film. Post-growth cyclic annealing reduced the dislocation density to $10^7 cm^{-2}$ [52].

One successful approach to reducing the dislocation density is through the use of buffer layers. Calculations predict a reduction of the threading dislocation density with increasing buffer layer thickness [53]. The first effective linearly graded buffers were grown by Fitzgerald et al. by MBE at AT&T Bell Labs [54, 55]. The graded buffers

reached 50% Ge composition, and they later improved their results with CVD [56]. Above 50% Ge composition, dislocation pileups produced surface undulations and prevented further relaxation by grading. In order to remove the dislocations and surface undulations, growth was interrupted at 50% Ge and a CMP step was employed. Growth was then resumed, allowing successful grading to pure Ge [57]. A grading rate of 10% Geμm^{-1} was used with a 2μm Ge cap, for a total thickness of 12μm. This process yielded a very low threading dislocation density of 2.1×10^6 cm^{-2}.

One way to reduce the strain, while still tailoring the bandgap, is by the addition of carbon to form SiGeC. The incorporation of carbon allows a bandgap reduction with respect to SiGe with the same lattice mismatch [58] and was first demonstrated by MBE by Ebert, et al [59]. Unfortunately, the addition of carbon to create an alloy lattice matched to Si is not a viable possibility for high Ge content films. This is because the carbon concentration is limited to about 4%, due to SiC precipitates and the low solubility of carbon in Si [60].

The method we have chosen for our Ge and SiGe growth is direct growth by UHV/CVD on Si substrates. This work builds on the work by Luan [5, 52, 61, 62], who used a two-step UHV/CVD growth process with post-growth cyclic annealing to produce high quality Ge epitaxial films with 10^7 cm^{-2} dislocation densities. This method produces Ge films suitable for high quality photodetectors without the need of thick buffer layers.

Relatively little work has been done with high Ge content Si$_x$Ge$_{1-x}$. Compositions ranging from pure Si to pure Ge were grown in the early days of semiconductors in bulk crystal growth, but the large splitting of the solidus/liquidus phase boundary makes it very difficult to pull bulk crystals of acceptable radial and axial homogeneity for

compositions differing from pure Si or pure Ge by more than a few percent [63].
Illustrating this point, Braunstein and coworkers reported in their seminal paper on the
optical absorption of SiGe alloys that samples of Ge composition between 20 and 90
percent were actually polycrystalline [8]. As the emphasis switched from Ge to Si,
interest in SiGe waned for many years. Although interest in SiGe has recently revived,
the interest has been primarily for Ge concentrations up to about 25%. In fact, many
articles in the literature refer to compositions of $x < 0.5$ as high Ge content. Kuyan and
Iyer, Jesson and coworkers, and Bauer and coworkers have all reported compositions of
$Si_{0.5}Ge_{0.5}$, but to our knowledge SiGe films of higher Ge concentration grown directly on
Si have not been reported without the use of graded buffers or strained layer superlattices.
The exception to this is a $Si_{0.7}Ge_{0.3}/Si_{0.2}Ge_{0.8}/Si_{0.7}/Ge_{0.3}$ structure grown by MBE on Si by
Barradas and coworkers. However, a layer of intermediate composition was grown to
accommodate strain, and the thickness of the $Si_{0.2}Ge_{0.8}$ layer was reported to be
inhomogeneous.

Section 3.2   *High Ge content SiGe epitaxy*

Section 3.2.1 Experimental growth procedure

A hot-walled UHV/CVD system was used for SiGe heteroepitaxy on Si. The base
pressure in the chamber is $< 10^{-8}$ Torr, and the water and oxygen partial pressures are
each $< 10^{-9}$ Torr. The substrates were 4" p-type Si <001> wafers with a resistivity less
than 0.01 Ohm-cm. Before heteroepitaxy the wafers were cleaned in a Piranha solution
(H2SO4 : H2O2 = 3 : 1) for 10 minutes. Following rinsing in deionized water, the native
oxide was removed by dipping the wafers in aqueous HF solution (HF : H2O = 1 : 10) for

30 seconds. In addition to removing the native oxide, the HF dip passivates the surface

of the wafer with a monolayer of hydrogen that is stable in atmosphere for several

minutes. After introduction to the reactor, heteroepitaxy was initiated at 335C with a

flow of 4.5 sccm of GeH4 (35% in Ar). The total pressure during Ge heteroepitaxy was

approximately 10 mTorr. After 50 nm was deposited, the furnace temperature was raised

and both SiH4 (n % in Ar) and GeH4 were flowed until approximately 1 μm was

deposited. Table 3-1 shows the temperature and flow conditions for each of the samples.

Finally, the wafers were annealed in the same furnace used for epitaxy.

Sample composition and crystallinity were determined by x-ray diffraction (XRD)

and the dislocation density determined by etch-pit density counding (EPD).

Photoreflectance measurements were performed to measure the direct transition energy,

E_g^{Γ}, as described in chapter four. XRD was performed using a Rigaku Ru300 instrument

with a high resolution 250mm diffractometer. A Cu anode is used in all experiments, and

a power of 0.6kW is used. Due to the high resolution of the instrument and strong

diffraction peak of Ge, and error of +- 0.001 degrees can be obtained. For EPD, the

etchant was a mixture of CH_3COOH (65 mL), HNO_3 (20 mL), HF (10 mL), and I_2

(35mg). Proper etching time for revealing etch pits varied between samples, but was

approximately 5 seconds. An optical microscope was used to count etch pits and was

calibrated using a microscope stage micrometer.

Section 3.2.2 Results and Discussion

Our primary purpose in growing Ge rich SiGe epitaxial films is to control the

direct transition energy, E_g^{Γ}, for use in optical applications, such as electro-optic

modulators. As shown in chapter four, tensile strain can be used to shrink E_g^{Γ}. Our goal

is to increase E_g^{Γ} by the addition of Si. The addition of Si increases E_g^{Γ} very rapidly, increasing approximately linearly with composition from 0.8eV for Ge to just over 4eV for pure Si [64]. The addition of only a few percent silicon is enough to vary E_g^{Γ} near the wavelength of interest, 1.55µm.

Using the previously described growth procedure, several films of varying compositions have been grown. This growth procedure is similar to the two step growth procedure developed by Luan for the growth of high quality Ge epilayers on Si [62], but has been modified by the flowing of SiH4 during the high temperature step to incorporate Si.

The attentive reader may note that the low temperature buffer layer is of pure Ge, whereas the rest of the film is SiGe. Attempts were made to incorporate Si into the low temperature buffer layer, but it was found that flowing SiH_4 during the low temperature step greatly reduced the deposition rate, most likely due to the higher activation energy of SiH_4 incorporation into the film. For this reason it was decided to incorporate silicon only in the high temperature step.

After growth, the SiGe films appear specular and exhibit no cross-hatch pattern, as is often associated with SiGe films grown using graded buffers. They have the same shiny appearance as the pure Ge epitaxial films.

XRD and photoreflectance analysis were performed to characterize the composition and E_g^{Γ} of the films. Photoreflectance analysis was performed as described in chapter four for pure Ge films. XRD was used to determine composition , but because both composition and strain are unknown, lattice spacings must be measured from two different lattice planes.

The two lattice planes used were the <001> and <422> planes. After obtaining

the spacing for each of the planes, the strain and composition are obtained as follows.

The following equations can be written for the spacing of each plane:

$$d_{400} = (1 + \varepsilon_{perpendicular}) \frac{a_{SiGe}}{4}$$

(3.1)

$$d_{422} = (1 + \varepsilon'_{perpendicular}) \frac{a_{SiGe}}{\sqrt{24}}$$

(3.2)

where the prime denotes the strain in the <422> direction. The perpendicular strain in the

two directions are related by

$$\varepsilon'_{perpendicular} = \varepsilon_{parallel} \sin^2 \theta + \varepsilon_{perpendicular} \cos^2 \theta$$

(3.3)

where theta is the angle between the planes and is 35.26 degrees. The parallel and

perpendicular strains are related by

$$\varepsilon_{parallel} = -\frac{2C_{11}}{C_{12}} \varepsilon_{perpendicular}$$

(3.4)

where C_{11} = 126.5 GPa and C_{12} = 48.3 GPa are the elastic constants of Ge [65]. Using

the above equations, the lattice constant of the SiGe film can be obtained. The lattice

constant is related to the composition by

$$a_{SiGe} = a_{Si}(1-x) + a_{Ge}(x) - bx(1-x)$$

(3.5)

where b = 1.88 x 10-3 nm [66].

Table 3-1 shows the growth conditions, composition, and E_g^Γ for each of the SiGe

films. It was found that an increase in Si content can be obtained by either increasing the

SiH$_4$ flow or by raising the growth temperature. SiH$_4$ incorporation into the film is

kinetically limited in our temperature range, whereas GeH$_4$ has a lower activation energy

and is only limited by the arrival rate of GeH$_4$ molecules. Therefore, raising the

temperature for a fixed SiH$_4$/GeH$_4$ ratio increases the Si content of the film.

Table 3-1 Growth conditions and resulting film properties for Si-rich SiGe films

Sample#	Tg(C)	SiH$_4$ (sccm)	GeH$_4$ (sccm)	Strain (%)	X$_{Si}$(%)	E$_g^{\Gamma}$(eV)	λ (nm)
R558-3	700	1.0	10	0.180	5.3	0.923	1343
R573-4	700	1.0	10	0.184	4.8	0.912	1360
R574-4	600	1.0	10	0.162	3.4	-	-
R576-5	650	1.0	10	0.172	4.2	0.905	1370
R577-6	650	0.7	10	0.17	2.7	0.87	1425

We found that for a given composition, a minimum growth temperature exists at which specular films may be grown. Below this temperature the film surface is characterized by large shallow depressions. The exact nature of the defect is not understood but is currently under investigation. For pure Ge, the minimum temperature for specular growth is 600C. Run 574 was a 600C growth containing 3.4% Si, but was of very poor quality. Because of the rough surface, it was not possible to use photoreflectance to measure the direct band gap. Keeping the same flow conditions but increasing the temperature (run 576) yielded a high quality film.

Figure 3.1 shows the direct band gap of our films as a function of composition, plotted together with published data for bulk SiGe. The measured band gaps of our films are consistently lower than for bulk SiGe, and we attribute this reduction to the tensile strain of the films. The amount of this energy reduction is similar to that for similarly strained pure Ge films, as discussed in chapter four.
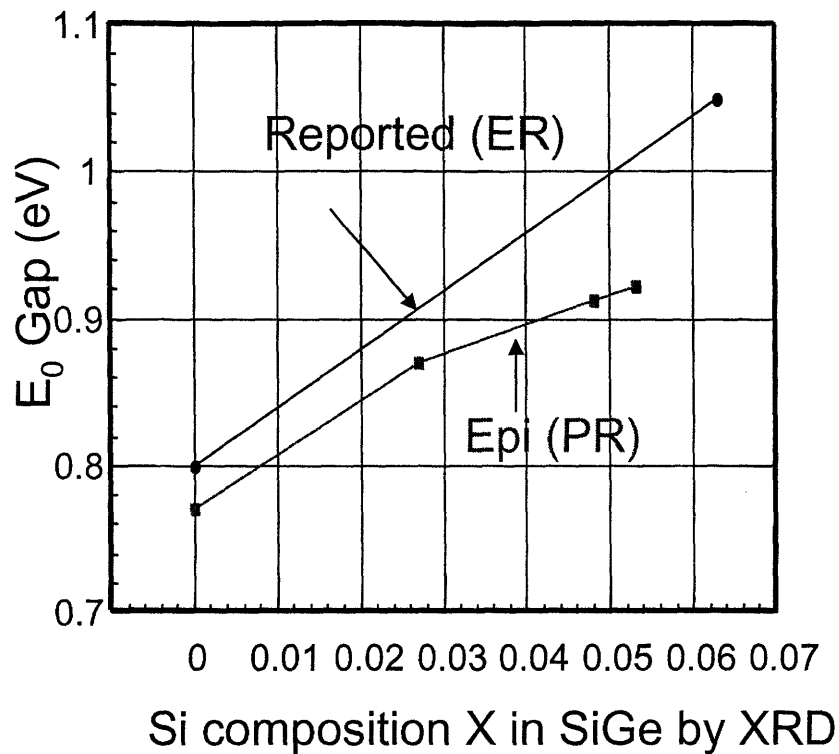
Figure 3.1 Band gap as a function of composition in epitaxially grown strained SiGe films. PR measurements courtesy of Jifeng Liu.

Films were annealed under different conditions and dislocation densities checked by etch pit density counting to determine film quality. Cyclic annealing has been shown to effectively reduce the dislocation density in Ge epitaxial films by two orders of magnitude to 10^7 cm^{-1} [62]. The present study had two objectives, which were to:

1) Determine the ability of a standard anneal to remove dislocations

2) determine the effect of Si (as an alloy material) on the ability to remove dislocations by annealing.

In this study we have used etch pit density counting to determine the dislocation density. This particular etch procedure has been shown to agree with TEM results to within a factor of two for counting dislocation densities in Ge epitaxial films [62].

55

Pieces of sample 558-3, which is $Si_{5.3}Ge_{94.7}$, were annealed at 900C under vacuum for 20, 40, and 60 minutes and the dislocation density counted by etch pit density counting. These are compared to samples of a pure Ge film grown at 600C. As shown in Figure 3.2, increasing the anneal time does reduce the dislocation density slightly. However, it is clear that a 20 minute anneal is effective in reducing the dislocation density to a similar level as that achieved by cyclic annealing.
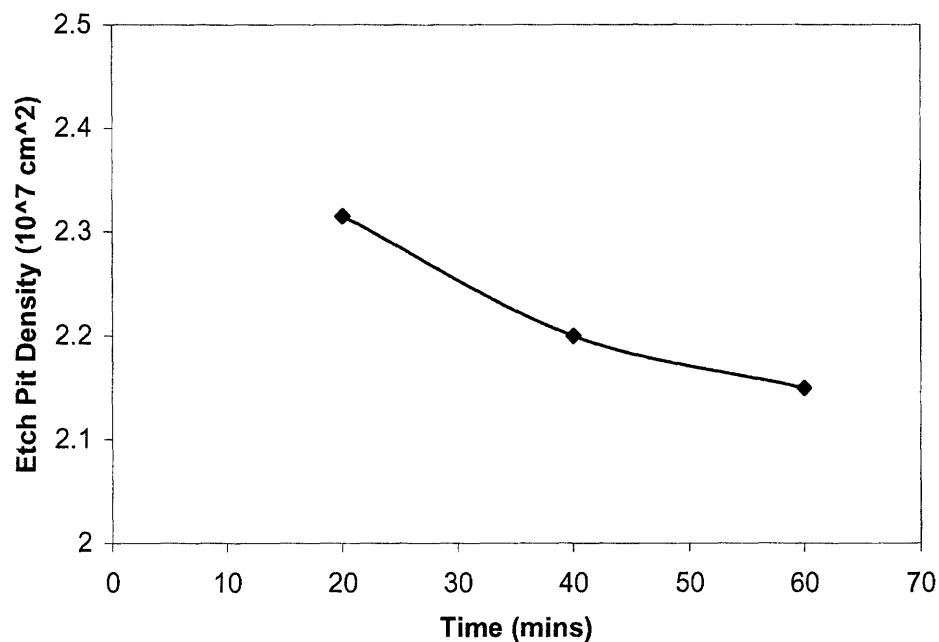
Figure 3.2 Dislocation density as a function of anneal time at 900C. Etch pit measurements courtesy of Uche Enuha.

Pieces from a pure Ge sample grown at 600C and annealed for different times show a similar trend of decreasing dislocation density for longer anneal times. The pure Ge samples also have a lower dislocation density than SiGe films annealed at the same conditions. While it may be that the presence of silicon does inhibit the removal of dislocations, the difference is relatively small and could be attributable to other factors. In comparing the effect of Si content on the dislocation reduction by annealing, all

samples were annealed for one hour at 900C. In examining the data of Figure 3.3, we do

not see a significant difference in the dislocation density over the range of Si content

studied, but note that all have dislocation densities similar, though slightly higher, to

those obtained for pure Ge. We can conclude that alloying small amounts of Si with Ge

does not have a large impact on dislocation motion and subsequent annihilation. This is a

significant result for Ge rich SiGe devices, for which film quality is an important

parameter directly affecting the leakage current and carrier lifetime.

Effect of Si content on dislocation density
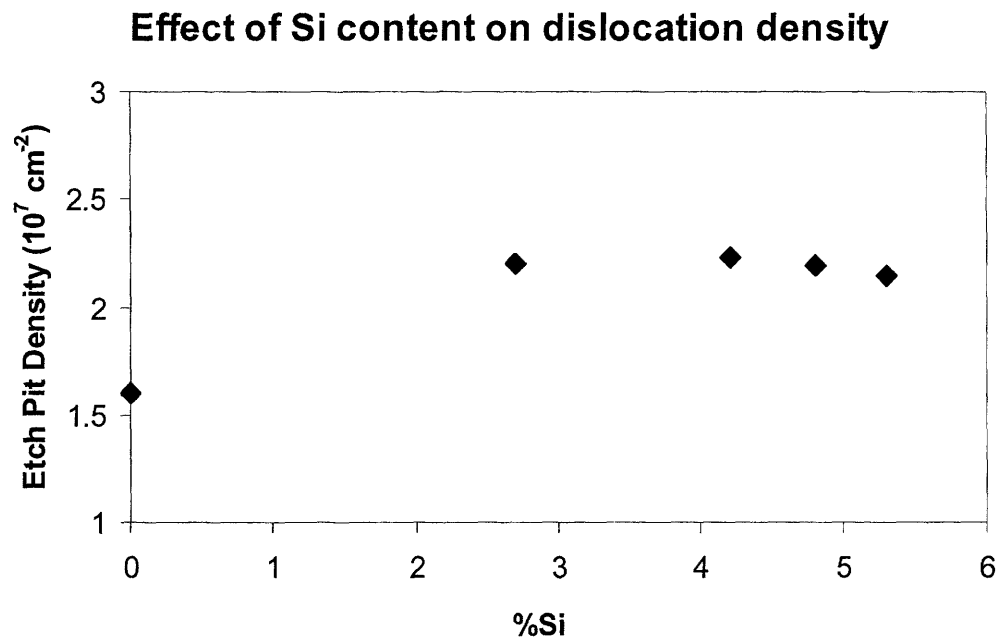
Figure 3.3 Dislocation density as a function of Si content in film. Etch pit measurements courtesy of Uche Enuha.

We have also shown that a single anneal at 900C is very effective in reducing the

dislocation density to levels obtained by cyclic annealing. It is important to note,

however, that dislocation density is not the only determining factor in determining the

carrier lifetime. In his cyclic annealing studies, Luan showed that additional cycles

significantly improved p-i-n responsivity, even though the reduction in dislocation density due to the additional annealing was small.[62] This shows that defects other than dislocations, such as point defects, play a significant role in determining the carrier lifetime in the material.

Section 3.3   *High quality and high yield selective Ge growth*

Selective epitaxial growth (SEG) of Ge is important for multiple reasons. First, if Ge is to be added to a wafer which has already undergone processing, the ability to grow selectively allows incorporation of Ge without covering the entire wafer. Although Ge is not detrimental to CMOS processing, manufacturers are very cautious when introducing new materials. Second, when reducing the dislocation density through annealing, growing on mesas allows for significant improvement over bulk films. The reason for this is that dislocations are eliminated from the material either by annihilation with dislocations of opposite Burger's vector or by gliding to the edge of the film. If the mesa size is of the order of the glide distance of a dislocation, the majority of the dislocations are able to leave the material through this mechanism. Luan has shown that cyclic annealing is more effective in reducing dislocation density as mesas size shrinks, with the dislocation density dropping very rapidly for microns smaller than 50 μm in diameter [62].

Section 3.3.1 Background

Selective growth of Si and SiGe has been the subject of prior investigation, with the first selective SiGe growth from SiH_4 and GeH_4/H_2 by UHV/CVD reported by Racanelli and Greve in 1991 [67]. Selective growth of SiGe by UHV/CVD has more

recently been investigated as a self-aligned base of a heterojunction bipolar transistors (HBT) to the emitter, the self-alignment allowing for smaller features and thereby reduced capacitance [68, 69]. In other work, selective epitaxial growth of Si has been explored by low pressure chemical vapor deposition (LPCVD) [70], and selective growth of SiGe has been pursued by low pressure vapor phase epitaxy (LPVPE) [71] and gas source molecular beam epitaxy (MBE) [72]. In both cases the Ge concentration studied was approximately 15%. The selective epitaxy of pure Ge on Si has been studied in the context of Ge dots by gas source MBE, but dot sizes were very small (~0.1 μm) and did not exhibit faceting, as was observed in the other research.

The focus of the present work was to develop a process for not only high quality mesas, as demonstrated by Luan, but high yield as well. Luan grew selective mesas by etching windows in an SiO_2 film on Si. Because GeH_4 will not deposit on SiO_2, mesas are grown selectively in the exposed Si windows. While this process yields selective growth, the overall quality of the mesas is poor. The reason for this is the loss of hydrogen passivation of the Si surface during the clean, due to the presence of the SiO_2 film. The last step of the clean is an HF dip, which serves not only to remove the native oxide from the Si surface, but leave a passivating layer of hydrogen. Bare Si wafers are hydrophobic and dewet upon removal from the HF dip, leaving a hydrogen passivated surface. On the contrary, a wafer predominantly covered with SiO_2 is not hydrophobic and does not dewet when pulled from the HF dip. The many HF droplets must be blown off with a nitrogen gun or removed in the spin dryer. In either method, as droplets are blown across the wafer surface, the hydrogen passivation is damaged. While some mesas can be found, the yield is low and the majority of the mesas have many visible pits in the

surface after growth. Unpassivated surface sites can oxidize in the air creating small regions of SiO_2, thus inhibiting epitaxial growth of Ge and leading to pits in the resulting epitaxial film. Figure 3.4 shows an optical micrograph of a mesa grown on a predominantly SiO_2 covered wafer. The mesa has many pits, which are congregated near the edge of the mesa. It has been found that defects are often congregated at the edges and corners of mesas where water droplets are most likely to stick. AFM has been perfomed on these defects and they have been shown to be deep pits whose depth is often the majority of the film thickness.
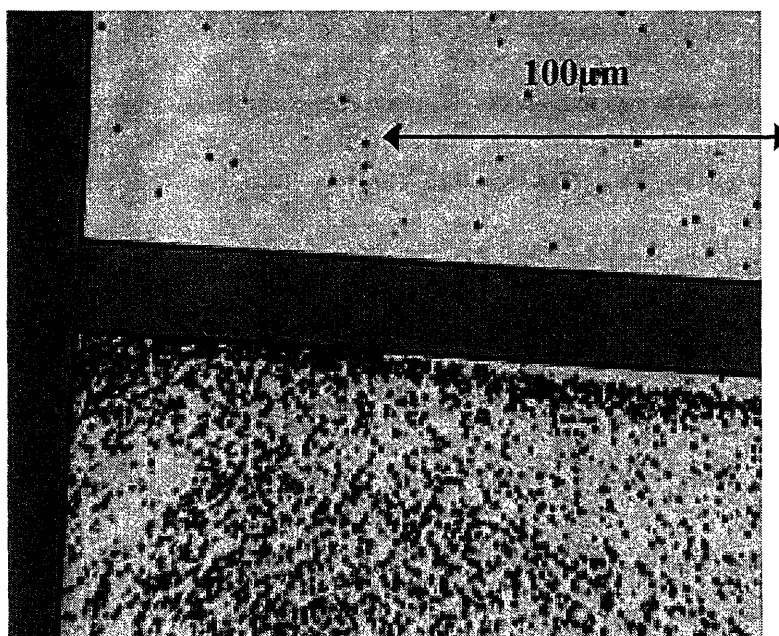
Figure 3.4 Optical micrograph of Ge mesa with growth defects due to loss of surface passivation

Section 3.3.2 Experimental growth of high yield Ge mesas

Two separate methods were successfully shown to maintain effective hydrogen passivation of the growth surface and produce a very high percentage of defect-free mesas. Although a few defects are still present, they are randomly distributed with a density no higher than that found on blanket Ge films with no selective growth.

60

The following two methods were used to produce high yield defect-free Ge

mesas:

Section 3.3.2.1   Poly Dewet Process

This process allows for high quality Ge selective epitaxial growth (SEG) without

depositing Ge directly on devices that may already be present on the wafer. Prior to Ge

deposition, the vast majority of the wafer surface is either the single crystal substrate

(where mesas are to be grown) or poly silicon deposited onto an oxide layer. In this way,

almost the entire surface of the wafer is hydrophobic, thus prohibiting droplets from

remaining on the wafer during cleaning and destroying the surface passivation. This is

done by first growing a thermal oxide and then etching openings where Ge mesas are to

be grown. Then, a layer of poly silicon is deposited and patterned so as to cover the

majority of the SiO_2 film. A ring of oxide is left to separate the poly Si from the epitaxial

Si, which serves to separate the Ge mesa (on epitaxial Si) from poly Ge (deposited on

poly Si) after growth. The wafer cleaning and growth procedure are the same for this

process as for growth and bare Si wafers. Figure 3.5 shows a side view of the structure

before and after growth.
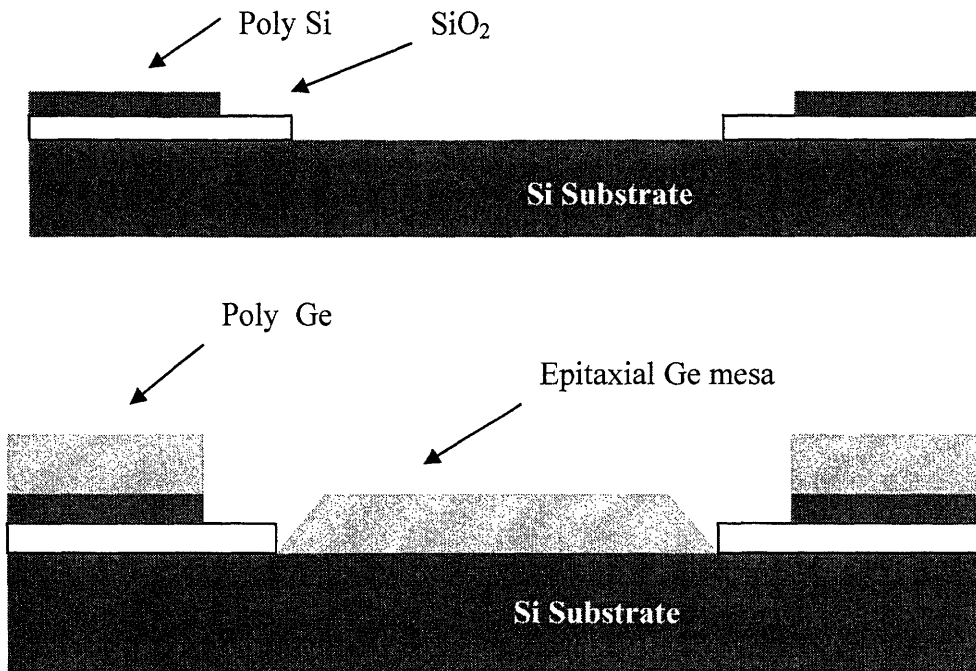
Figure 3.5 Cross-sectional view of poly dewet process wafer a) before and b) after Ge deposition

For actual device processing, the poly Ge can be removed from the wafer after

growth by etching in H_2O_2 or other Ge etchants, if the mesa is protected by photoresist or

another protective layer.

Figure 3.6 shows cross-sectional an SEM image of a Ge mesa grown using the

poly dewet process. The Ge mesa is clearly shown, as well as the oxide layer, polySi

layer, and poly Ge growth. The mesa is grown on <100> Si and the edge lies in the

<110> direction. The facet at the mesa edge exposes the <311> face, which makes a 27

degree angle with the wafer surface. <311> faceting has been observed in both Si [70]

and SiGe [72] SEG. The Ge deposition on the polySi, on the other hand, does not exhibit

faceting, but deposits on both the top and side of the poly Si.
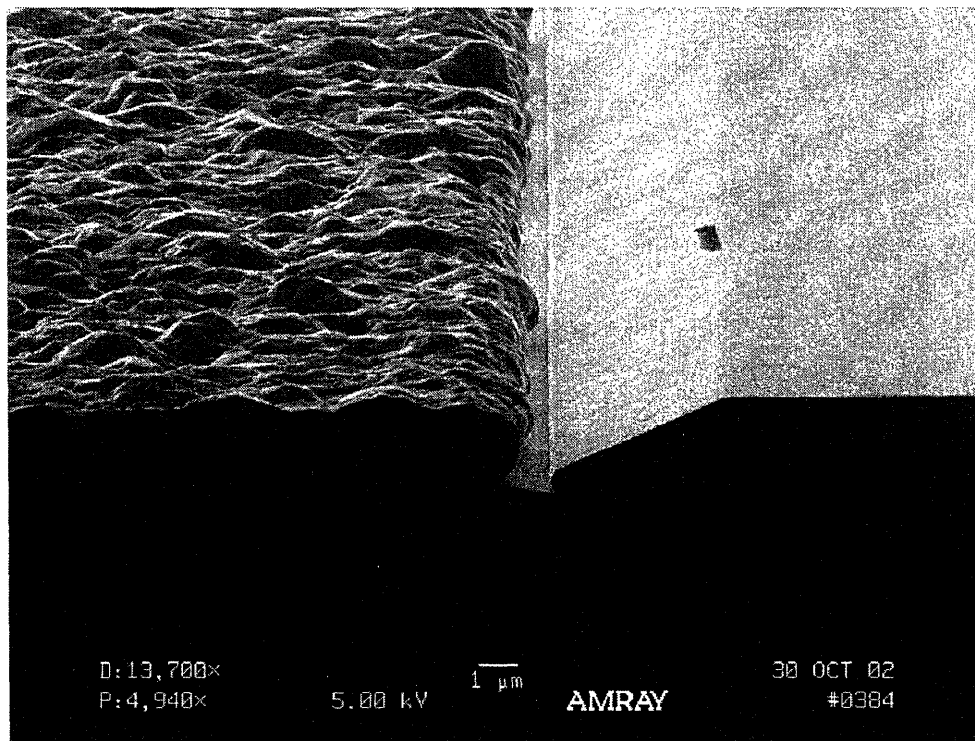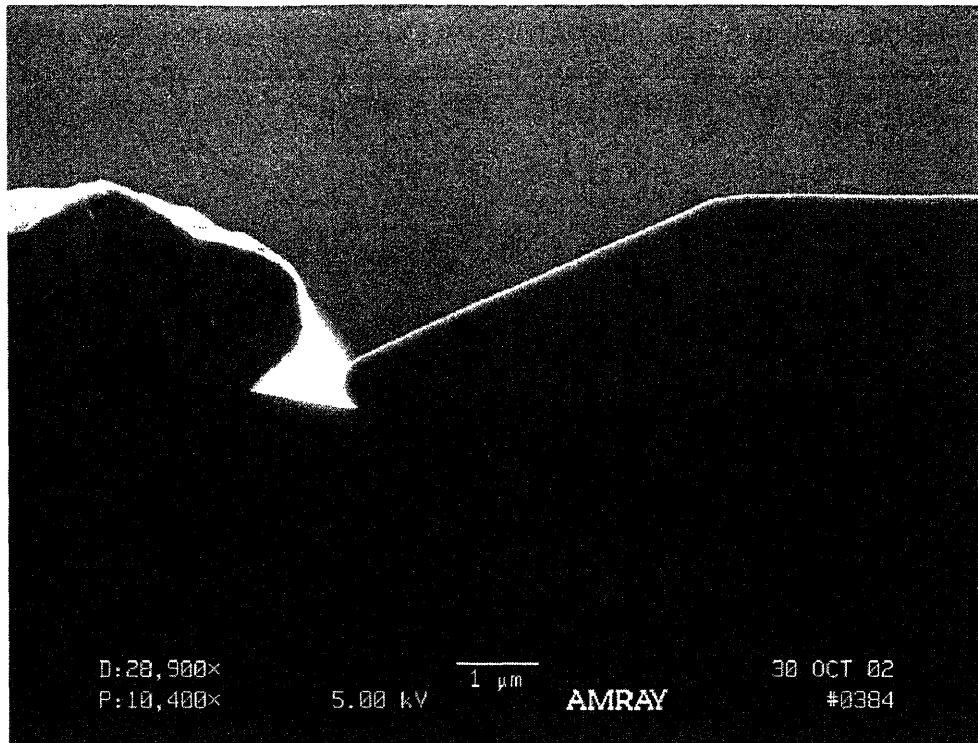
Figure 3.6 Cross-section SEM images of Ge mesa grown using poly dewet process

Figure 3.7 shows an AFM image of a 50µm x 50µm Ge mesa from the same wafer. The height of the mesa is measured to be 2.1µm, and the top surface of the wafer has an rms roughness of 2.03nm. An interesting feature is the slight ridge present at the edge of the mesa, which is not visible in the SEM photos. Kawaguchi and co-workers report similar ridges in Si and $Si_{86}Ge_{14}$ SEG on Si (001) grown by gas source MBE [72]. For the silicon case, the ridge was shown to be due to longer surface diffusion length of Si atoms on the <311> facet than on the <100> surface. This leads to a net flow of atoms from the <311> facet to the <100> surface. For the SiGe case, surface diffusion alone could not account for the shape of the ridge, and it was believed that strain in the film also played a role. We believe that the same mechanisms are also responsible for the ridges present on our mesas.
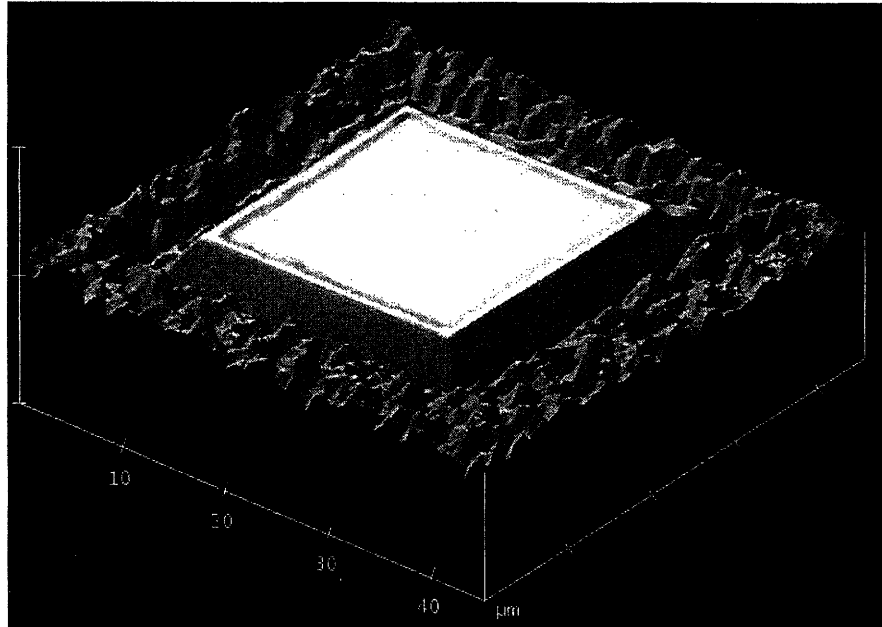
Figure 3.7 AFM image of Ge mesa grown using poly dewet process. Image courtesy of Dave Danielson

Figure 3.8 shows an optical micrograph of a cross-shaped mesa grown using the poly dewet process. The rough poly Ge is clearly visible surrounding the smooth Ge mesas. The <311> facets on the edges of the mesa are also clearly visible.
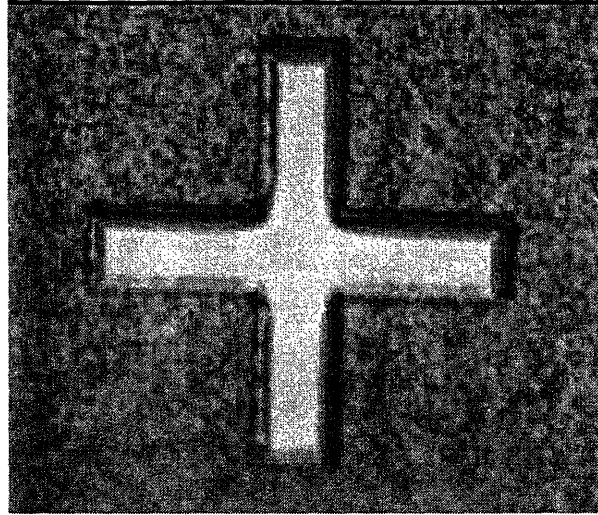
Figure 3.8 Optical micrograph of Ge mesa grwon using poly dewet process

Section 3.3.3   Oxide ring process

The second process used to grow high yield mesas is to simply pattern oxide rings on the wafer, which serve to outline the edges of the Ge mesas. In this simpler process, the number of masks levels required prior to Ge deposition is only one. However, if other devices are already present on the wafer, materials that are not hydrophobic may attract drops from the HF clean and reduce the effectiveness of the hydrogen passivation, as previously described. This process was used for p-i-n diodes fabricated in this thesis, as they are the only devices present on the wafers.

Figure 3.9 shows a side view of a wafer with Ge mesas deposited that was prepared using this process. First, a layer of SiO_2 is either grown or deposited. (In our case a 0.2μm thermal oxide was grown.) Then, the oxide is patterned and etched to leave

rings of oxide defining the Ge mesas. The only constraint is that any remaining oxide

areas must not be large enough to attract droplets when pulled from the HF dip. The final

step is to grow epitaxial Ge using the procedure previously described. Ge mesas

produced using this method are of high quality and have been used to fabricate Ge

diodes, as described in chapter five.
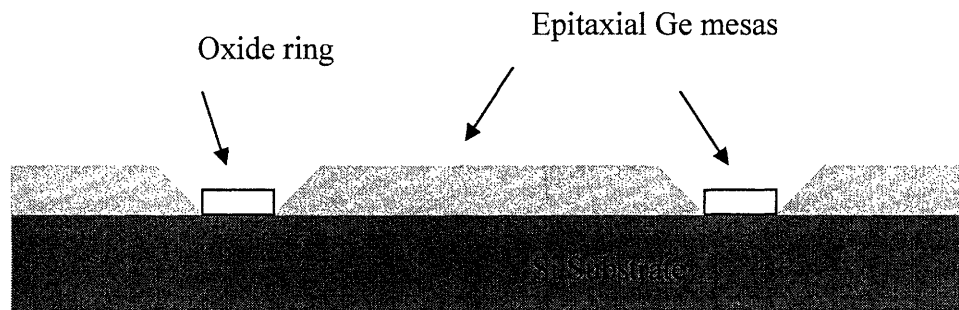
Figure 3.9 Cross-sectional diagram of wafer containing Ge mesas grown by oxide ring process

The oxide ring both defines the mesas and allows for proper surface passivation

during cleaning.

In summary, two process have been presented which enable high yield selectively

grown Ge mesas. The keys to both processes are to use SiO_2 to define the mesas and to

provide a wafer surface that allows for proper hydrogen passivation upon removal from

the HF dip during wafer cleaning.

Chapter 4: Bandgap tuning of epitaxially grown Ge on Si substrates by strain control

Section 4.1 Strain: friend or foe?

This question might lead us to immediately ask additional questions:

1) Are epitaxial Ge films grown on Si by UHV/CVD strained? If so, is it tensile or compressive strain?

2) How much control do we have over the amount of strain?

3) What effect does tensile or compressive strain have on the band structure of Ge?

4) If there is an effect on the band structure, how will this affect photodetector performance?

In this chapter we answer these questions. Here are the key results, so you know what to expect:

Epitaxially grown Ge films have tensile strain, the amount of which can be controlled.

Both tensile and compressively strained Ge films have a reduced direct band gap as compared to bulk material.

This band gap reduction pushes the photoresponse of diodes to longer wavelengths, which is a big plus.

The increase in intrinsic carrier concentration resulting from the band gap reduction is less than would be expected due to a change in the valence band density of states.

Theoretical calculations agree very well with our experimental results.

Section 4.2 Effects of strain on E_g^Γ in epitaxially grown Ge films

Others have shown both theoretically[73] and experimentally[74] that strain in the <100> direction changes the direct transition energy E_g^Γ in Ge. To date, all experimental data has come from applying strain to bulk Ge samples. In our case, however, we have epitaxially grown tensile strained Ge films on Si substrates using a UHV/CVD process. The films have very little or no strain during growth at elevated temperature, but upon cooling become tensile strained due to the difference in thermal expansion coefficients between Ge and Si. The strain in the films depends on the growth temperature, and we report an increasing reduction in the direct transition energy for increasing strain. For small strains (< 0.3%) we obtain a linear decrease in the direct transition energy of ~150meV per percent tensile strain. We are also able to control the amount of strain after the growth through subsequent annealing. As will be shown in section 4.7, theoretical calculations by deformation potential theory agree well with our experimental data, within the limits of experimental error.

Section 4.3 Growth procedure

Ge films were epitaxially grown on Si substrates by UHV/CVD. Bare Si wafers are first prepared by wet chemical cleaning, ending with a 15 sec dip in 10:1 H_2O:HF for hydrogen passivation of the Si surface. The wafers are then introduced into the UHV/CVD system where Ge is deposited epitaxially using a two-step growth process.

68

The process consists of a low-temperature (but slow growth rate) deposition to avoid islanding of the film, followed by a high temperature deposition step with faster deposition rate. The growth procedure is described in detail elsewhere.[52] The thickness of the films used in this study ranges from 1.3 to 1.75μm as determined by Rutherford backscattering (RBS).

Section 4.4   Strain in Epitaxial Ge films

The strain in epitaxial Ge films was measured by comparing the Ge(400) peak positions in θ-2θ XRD step scans of Ge thin film with bulk Ge(100) single crystal samples (Fig. 4.1). The Ge(400) peaks in epitaxial Ge films show significant shifts to higher 2θ angles, indicating the existence of tensile strain in these samples. From the θ-2θ XRD data, we can obtain the strain in the direction perpendicular to the film:

$$\varepsilon_\perp = \frac{d_{400}^{film} - d_{400}^{bulk}}{d_{400}^{bulk}}, \qquad (4.1)$$

where d_{400}^{film} and d_{400}^{bulk} are the spacings of Ge(400) planes determined from Kα1 diffraction peak positions in thin film and bulk samples, respectively. Since the film is under biaxial stress, the in-plane strain $\varepsilon_\parallel$ is related to $\varepsilon_\perp$ by:

$$\varepsilon_\parallel = -\frac{2C_{11}}{C_{12}}\varepsilon_\perp, \qquad (4.2)$$
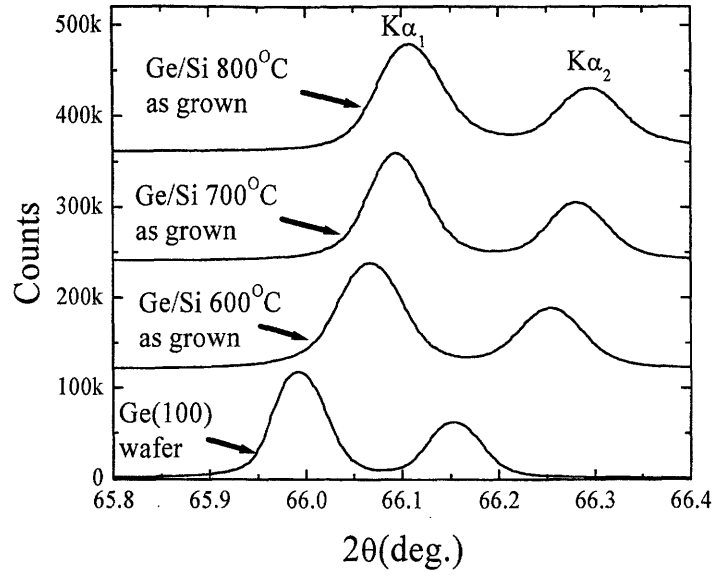
Figure 4.1 Raw XRD data for Ge films grown at different temperatures. Measurements courtesy of Jifeng Liu.

where C_{11}=126.5GPa and C_{12}=48.3GPa [65] are the elastic constants of Ge. On the other hand, thermally induced strain in thin films can be calculated theoretically by taking into account the difference in thermal expansion coefficients of Si and Ge assuming no strain relaxation occurs upon cooling:

$$\varepsilon_{\parallel} = \int_{T_0}^{T_1}(\alpha_{Ge}(T) - \alpha_{Si}(T))dT , \qquad (4.3)$$

where T_0 and T_1 are room temperature and growth temperature, $\alpha_{Ge}(T)$ and $\alpha_{Si}(T)$ are the thermal expansion coefficients of Ge and Si at temperature T (°C), respectively, and are given by[75, 76]:

$$\alpha_{Ge}(T) = 6.050\times10^{-6} + 3.60\times10^{-9}T - 0.35\times10^{-12}T^2 \quad (°C^{-1}) \qquad (4.4)$$

$$\alpha_{Si}(T) = \{3.725\times[1 - \exp(-5.88\times10^{-3}(T + 149.15))] + 5.548\times10^{-4}T\}\times10^{-6} \quad (°C^{-1}) \quad (4.5)$$

70

in the range between 25 and 900°C. Figure 4.2 shows the comparison of the experimentally measured strain (by XRD) in Ge films with theoretical calculation by (3) assuming no strain relaxation upon cooling. It is found that although the experimental data are roughly consistent with the calculation, they are generally smaller (by ~0.05%) than theoretical calculations. The strain in Ge film can be divided into two parts: (i) intrinsic compressive strain ε_i due to the lattice mismatch between Si and Ge, and (ii) thermally induced tensile strain ε_T accumulated during the cooling process due to the thermal mismatch. So there are two possible reasons for the smaller tensile strain observed experimentally compared to theoretical calculation: (i) existence of a small intrinsic compressive strain at the growth temperature, and (ii) strain relaxation during the cooling process. Both factors may contribute to the final experimental results and further investigation is needed to fully understand the process of strain accumulation.
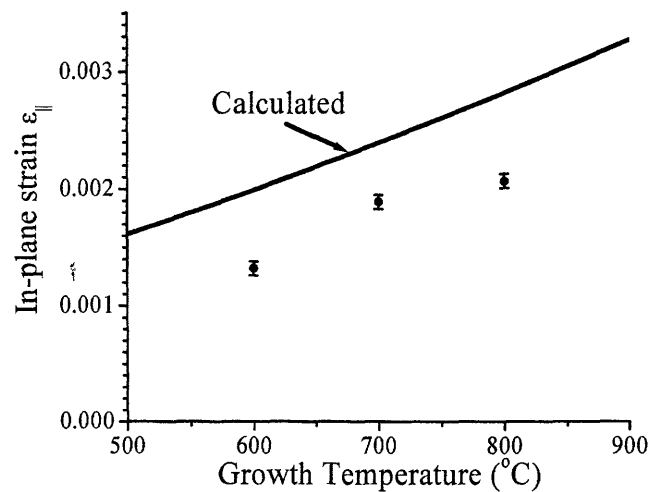
Figure 4.2 Experimenatl and calculated data for strain vs. growth temperature in Ge films epitaxially grown on Si. Measurements courtesy of Jifeng Liu.

The strain of the film may also be controlled by subsequent annealing. If the anneal temperature is high enough and the time is long enough, the film will become relaxed at the anneal temperature. During cooling from the anneal it will develop strain, as previously discussed. In this manner annealing may be used to increase the strain in a film, if the anneal temperature is higher than the initial growth temperature.

Strain vs. Growth Temperature
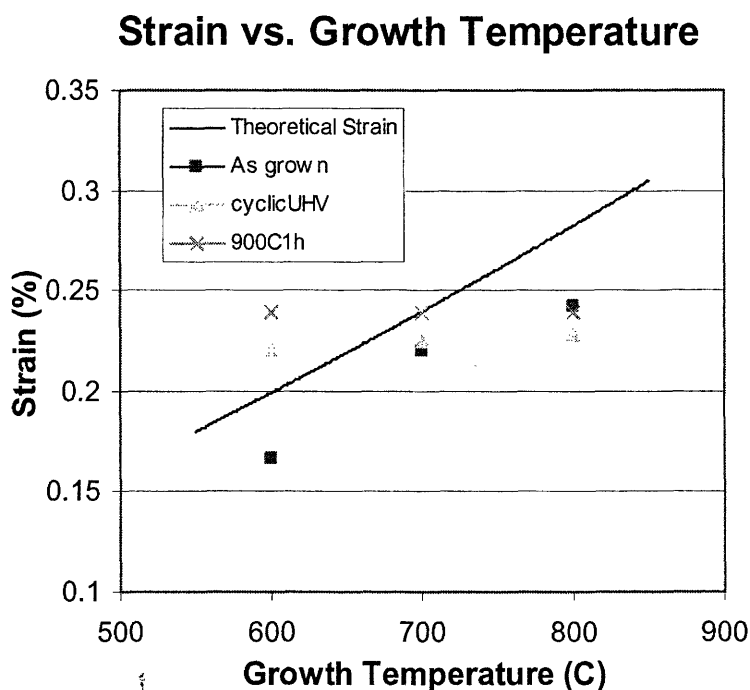
Figure 4.3 Effect of post-growth annealing on strain in Ge films. Measurements courtesy of Jifeng Liu.

Figure 4.3 shows the effect of post-growth annealing on strain. After a one hour anneal at 900C, films grown at 600, 700, and 800 degrees Celsius all have the same strain as films grown at 900C. The cyclic anneal was for 10 cycles between 900C and 700C, with each step being held for 10 minutes. For the cyclic anneal, the last step was a 10

72

minute 700C anneal, which may explain why the strain in these films is closer to that of films grown at 700C.
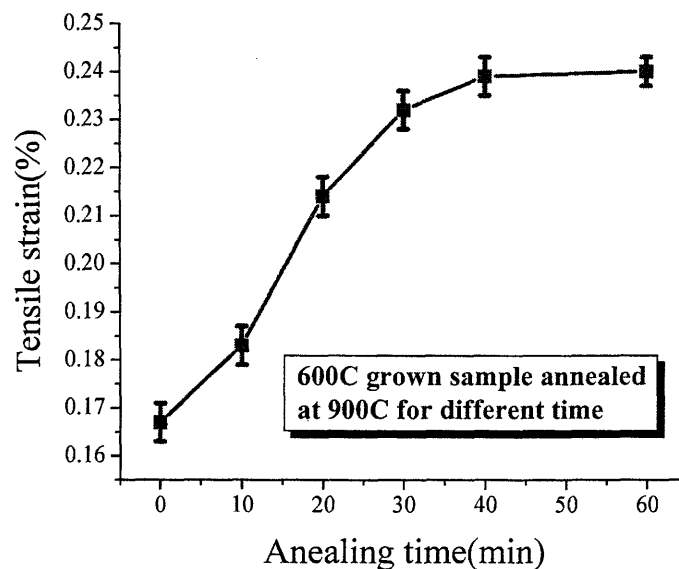
Figure 4.4 Effect of annealing time at 900C on strain of film grown at 600C. Measurement courtesy of Jifeng Liu.

Figure 4.4 shows the effects of annealing time on strain for anneals at 900C. We can see that an anneal of 40 minutes is required to achieve maximum strain. The amount of time required for the wafer to heat to 900C is not known, making it difficult to determine exactly the relaxation rate of the film.

Section 4.5   Determination of E_g^Γ by photoreflectance measurements

Photoreflectance (PR) measurements were performed to determine the direct band gap, E_g^Γ, in the tensile strained Ge thin films grown at different temperatures. With both

73

XRD and PR measurements, we are able to obtain the E_g^Γ vs. $\varepsilon_\parallel$ relation experimentally from samples grown at different temperatures.

The measurement is described in a previous publication [77] and will be reviewed briefly here. The main concept is that the reflectance of the material changes with an applied electric field. An electric field is induced in the material by shining 450nm laser light on it. This creates carriers near the surface of the film and alters the electric field. By measuring the change in reflectance due to the field over a range of wavelengths near the absorption edge, it is possible to determine both the strength of the electric field and the band gap corresponding to the absorption. A schematic of the measurement apparatus is shown in Figure 4.5.
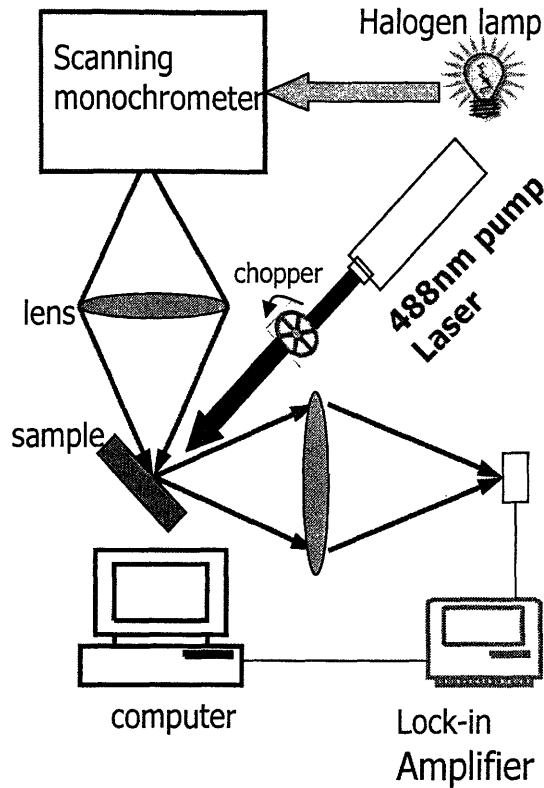
Figure 4.5 Experimental setup for photoreflectance measurement.

A Halogen lamp provides a broadband light source, and a monochrometer is used to select the given wavelength for illumination. An Ar+ laser (λ = 488 nm, 24 mW/cm2) is chopped at 200Hz and used as the pump light. The change in reflectivity is measured using a lock-in technique. For a given electric field, the change in reflectance oscillates as a function of wavelength. The direct gap energy E_g^{Γ} and electric field strength F of the Ge sample are determined from the locations of the Franz-Keldysh oscillations (FKO) peaks Ej (j = 1,2,3,....), using

$$E_j = (e^2 F^2 \hbar^2 / 8\mu)^{\frac{1}{3}} C_j + E_g \qquad (4.6)$$

and

$$C_j = \left[\frac{3\pi(j - \frac{1}{2})}{2} \right]^{\frac{2}{3}}$$ (4.7)

where μ is the interband reduced mass.[78-80] Figure 4.6 shows photoreflectance data

for bulk Ge and a Ge epilayer. The peaks in the oscillation for grown Ge are located at

lower energies than for bulk Ge, indicative of a shrinkage in the band gap. E_g^{Γ} can be

determined quantitatively from the plot of E_j vs. C_j, shown in Figure 4.7. From equation

4.6, we see that E_g is determined by the intersection of the line with C_f = 0. For the Ge

layer, E_g = 0.769 ± 0.004 eV, which is smaller than that of the bulk (E_g = 0.779 ±

0.009eV) by ~0.3eV. As will be shown, the band gap reduction is due to tensile strain.
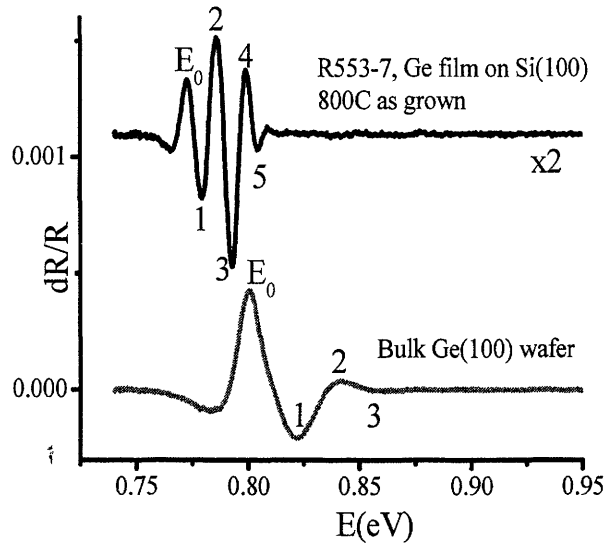
Figure 4.6 Photoreflectance data for bulk Ge and epitaxial Ge film. Measurements courtesy of
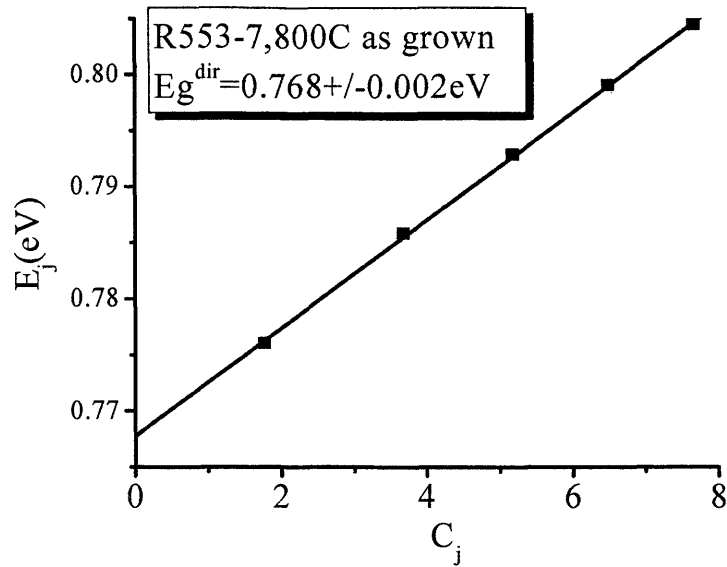
Jifeng Liu.

Figure 4.7 Plot of photoreflectance peak energy vs C$_j$. Measurements courtesy of Jifeng Liu.

Figure 4.8 shows the strain and direct band gap for samples grown at different

temperatures. We see a reduction in the direct gap for increasing growth temperature.

We have shown that increasing growth temperature also increases the tensile strain in the

film. The maximum thermal strain we have been able to attain is approximately 0.2%,

which is for 800C grown films. Annealing at 900C does not allow us to capture more

strain, indicating that dislocations are very mobile at high temperatures, allowing the film

to relax as it cools. In the next section we will show that the band gap reduction is due to

this increase in tensile strain.
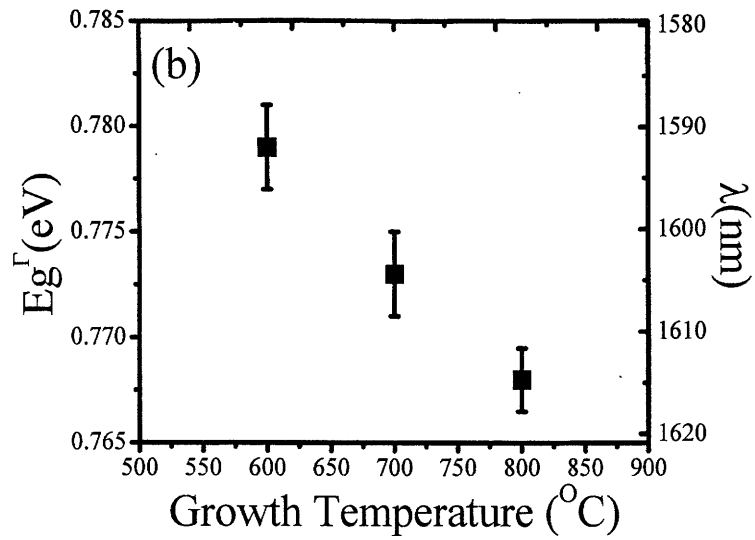
Figure 4.8 Band gap vs growth temperature of epitaxially grown Ge films. Measurements couretesy

of Jifeng LIu.

Section 4.6   Theoretical effect of tensile strain on the band

structure of Ge

E_g^{Γ} vs. $\varepsilon_{\parallel}$ relation can also be calculated theoretically by deformation potential

theory[73]. According to this theory, under the biaxial stress the direct band gap of Ge

will shrink, with the Γ point lowering and the valence band splitting.
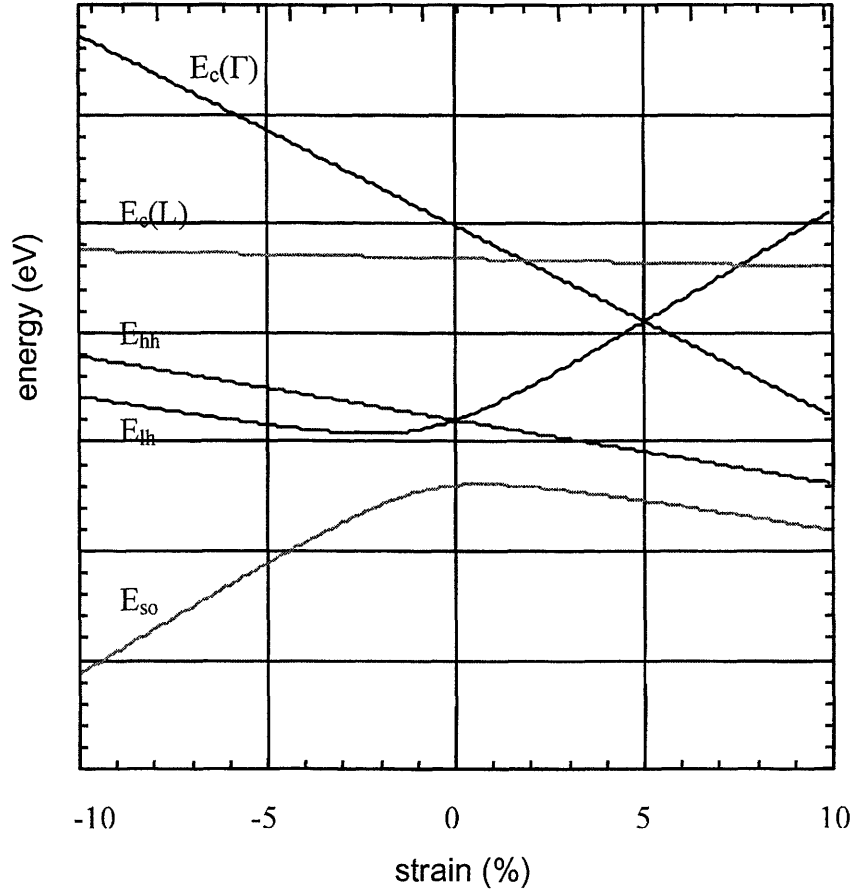
Figure 4.9 Effect of strain on the band structure of Ge. Calculated from data by Van de Walle [73]

The effect of both tensile and compressive strain on the band structure of Ge has

been calculated by Van de Walle, and is shown in Figure 4.9. [73] Figure 4.10 illustrates

the effect of biaxial tensile strain on the Ge band structure near the Γ point (000) of the

Brillouin zone. The effect of strain is quantitatively described as:

$$E_g^\Gamma(lh) = E_g^{\ \Gamma}(0) + a(\varepsilon_\perp + 2\varepsilon_\parallel) + \Delta_0/2 - 1/4\,\delta E_{100} - 1/2\,\sqrt{\Delta_0^2 + \Delta_0\delta E_{100} + 9/4\,(\delta E_{100})^2} \quad (4.8a)$$

$$E_g^\Gamma(hh) = E_g^{\ \Gamma}(0) + a(\varepsilon_\perp + 2\varepsilon_\parallel) + 1/2\,\delta E_{100}\ , \quad (4.8b)$$

where $E_g^\Gamma(lh)$ and $E_g^\Gamma(hh)$ are the band gaps from the maxima of light hole and heavy

hole valence bands to the bottom of conduction band at k=0 in the band diagram under an

in-plane strain $\varepsilon_\parallel$, respectively. $E_g^\Gamma(0)$=0.80 eV is the direct band gap of unstrained Ge

at room temperature[81]; b=-(9.0±0.4) eV and b=-(2.6±0.2) eV are deformation potential

constants of [100] Ge at room temperature as reported by Pollak et al[74];

$\delta E_{100} = 2b(\varepsilon_\perp - \varepsilon_\parallel)$ and $\Delta_0 = 0.30eV$ for Ge[81]. Figure 4.11 shows the comparison of

the calculated results with our experimental data.

Tensile

E_g^E
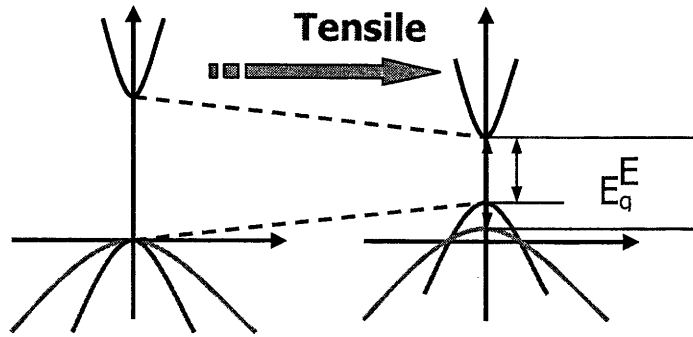
Figure 4.10 Effect of biaxial tgensile strain on the band sturcutre of Ge (near gamma point)
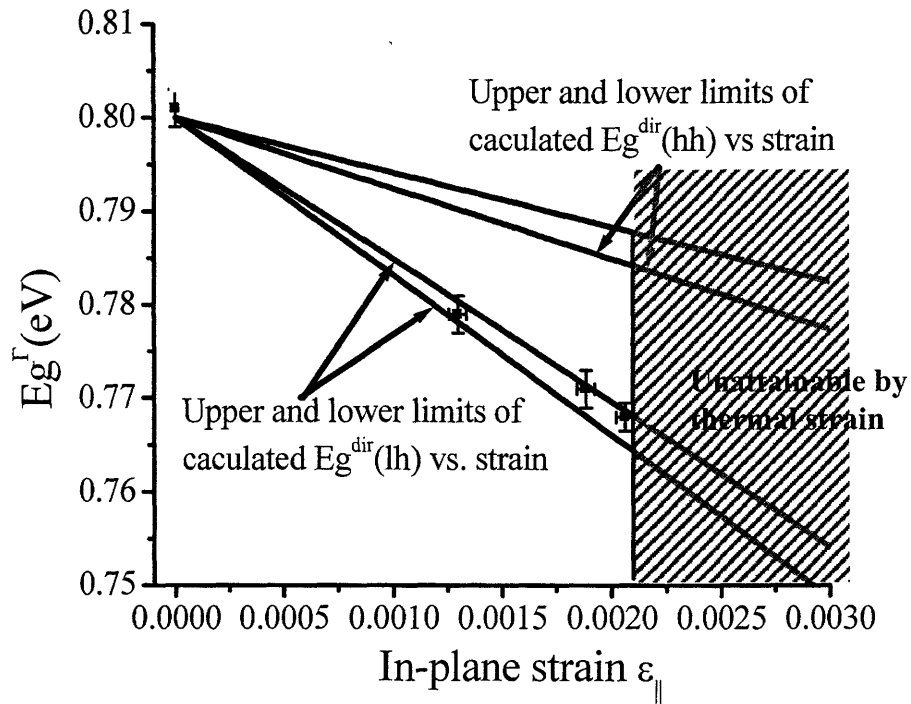
Figure 4.11 Comparison of experimental shift in band gap with stain to theoretical calculations. Measurements and calculations courtesy of Jifeng Liu.

To take into account the error ranges of a and b,we have plotted the upper and

lower limits of theoretical predictions. The experimental data for direct Eg agrees quite

well with the theoretical calculations of $E_g^\Gamma(lh)$ vs. strain, confirming that the Γ point has

moved down and the light hole band has moved up relative to the unstrained valence

band, as predicted by theory. The E_g^Γ and corresponding wavelength as a function of

growth temperature were shown previously in Figure 4.8.

Section 4.7   Improved spectral response of Ge photodetectors due to tensile strain

For the epitaxial Ge film grown at 800C we measure a 0.21% tensile strain. This results in a direct band gap reduction from 0.801eV for bulk Ge to 0.768eV, corresponding to 1550nm and 1610nm, respectively. Therefore the absorption spectrum of Ge is pushed to longer wavelengths by ~60nm, covering a large part of the L-band in telecommunications. Indeed, the absorption coefficient (α) measurements reported in our earlier paper[77] showed that the absorption coefficient of 700°C grown, cyclic annealed sample was 10^3/cm at 1605nm, while that of bulk Ge was only 2.2×10^2/cm. Figure 4.12 shows the responsivity of a diode fabricated from a strained film grown at 800C with the calculated responsivity of a comparable diode made from unstrained bulk Ge. We can see that the responsivity curve is shifted to longer wavelengths by 20-30 nm. A detailed description of the fabrication and performance of these diodes will be given in chapter 5.
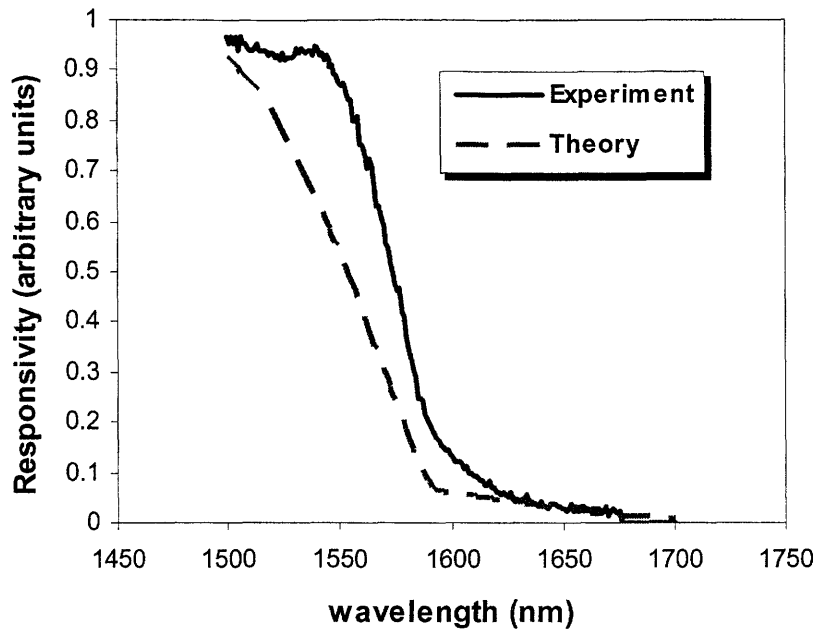
Figure 4.12 Responsivity of diode made from 800C film compared to simulated responsivity for bulk

Ge diode. Measurement courtesy of Nok Jongthammanurak

Section 4.8   Effect of tensile strain on the intrinsic carrier

concentration in Ge

We have demonstrated that epitaxially strained Ge has a reduced direct transition

energy. Furthermore, the strain induces a splitting of the light hole and heavy hole bands,

the light hole band becoming higher in energy. This raises an important question. "What

effect will biaxial strain have on the intrinsic carrier concentration of Ge?" Since the

leakage current of a diode is directly affected by the intrinsic carrier concentration, this is

an important question.

In this section we calculate the intrinsic carrier concentration of Ge under biaxial

strain. We have two competing effects. The reduction in band gap will tend to increase

83

the carrier concentration. However, the splitting of the valence bands will tend to decrease the carrier concentration. The light hole band, shifted up in energy with respect to the heavy hole band, has a much lower density of states. In this calculation we assume that the strain does not affect the density of states of the conduction or valence bands, but simply shifts them in energy.

The equilibrium carrier concentration in a band is given by

$$n_o = \int_{E_0}^{\infty} g(E) f(E) dE \tag{4.9}$$

where g(E) is the density of states, f(E) is the Fermi-Dirac function, and E_0 is the energy at the bottom of the band. A fundamental result of solid-state physics, and also an experimental observation, is that the density of states near a band edge has a square root dependence on energy. Consequently, we can express the conduction band density of states as

$$g_c = A_c \sqrt{E - E_c} \qquad E \geq E_c \tag{4.10}$$

For the valence band we express the density of states of the light and heavy hole bands separately.

$$g_{lh} = A_{lh} \sqrt{E_{lh} - E} \qquad E \leq E_{lh} \tag{4.11a}$$

$$g_{hh} = A_{hh} \sqrt{E_{hh} - E} \qquad E \leq E_{hh} \tag{4.11b}$$

The prefactors are given by

$$A_c = 4\pi \left(\frac{2m_{de}^*}{h^2} \right)^{3/2} \tag{4.12a}$$

84

$$A_{lh} = 4\pi \left(\frac{2m_{dlh}^{*}}{h^2} \right)^{3/2}$$

(4.12b)

$$A_{hh} = 4\pi \left(\frac{2m_{dhh}^{*}}{h^2} \right)^{3/2}$$

(4.12c)

where the masses are the density of states effective masses. We have used $m_{de}^{*} = 0.22m_0$, $m_{dlh}^{*} = 0.044m_0$, and $m_{dhh}^{*} = 0.33m_0$. Substituting, the equilibrium carrier concentration for the conduction band is given by

$$n_0 = 4\pi \left(\frac{2m_{de}^{*}}{h^2} \right)^{3/2} \int_{E_c}^{\infty} \frac{\sqrt{E - E_c}}{1 + \exp\left(\frac{E - E_f}{kT} \right)} dE$$

(4.13)

If the semiconductor is non-degenerate, as it is in our case, the result can be simplified to the following familiar expression

$$n_0 = N_c \exp\left(\frac{E_f - E_c}{kT} \right)$$

(4.14a)

where

$$N_c = \left(\frac{2\pi m_{de}^{*}}{h^2} \right)^{3/2}$$

(4.14b)

We can write similar equations for the carrier concentrations in the light and heavy hole bands.

$$p_{lh} = N_{lh} \exp\left(\frac{E_{lh} - E_f}{kT} \right)$$

(4.15a)

$$p_{hh} = N_{hh} \exp\left(\frac{E_{hh} - E_f}{kT} \right)$$

(4.15b)

where

$$N_{lh} = 2\left(\frac{2\pi m^*_{dlh}}{h^2}\right)^{3/2}$$ (4.16a)

$$N_{hh} = 2\left(\frac{2\pi m^*_{dhh}}{h^2}\right)^{3/2}$$ (4.16b)

Under biaxial strain the light and heavy hole bands will be shifted in energy relative to each other by an amount ΔE.

$$E_{hh} = E_{lh} - \Delta E$$ (4.17)

The total hole population can then be expressed as

$$p_0 = p_{lh} + p_{hh} = \left(N_{lh} + N_{hh} \exp\left(\frac{-\Delta E}{kT}\right)\right) \exp\left(\frac{E_{lh} - E_f}{kT}\right)$$ (4.18)

The np product is then given by

$$n_0 p_0 = N_c\left(N_{lh} + N_{hh} \exp\left(\frac{-\Delta E}{kT}\right)\right) \exp\left(\frac{-E_g}{kT}\right)$$ (4.19)

where the bandgap, E_g, is given by

$$E_g = E_c - E_{lh}$$ (4.20)

The intrinsic carrier concentration, n_i, is the square-root of the np product.

$$n_i = \sqrt{N_c\left(N_{lh} + N_{hh} \exp\left(\frac{-\Delta E}{kT}\right)\right)} \exp\left(\frac{-E_g}{2kT}\right)$$ (4.21)

We now use deformation potential theory to determine ΔE and E_g as a function of strain. The strain-dependent band gap of the light and heavy hole bands, as measured from the bottom of the conduction band, are given in equations 4.8a and 4.8b. E_g and ΔE are given by

$$E_g = E_b^{\Gamma}(hh) \qquad\qquad\qquad (4.22)$$

$$\Delta E = E_b^{\Gamma}(hh) - E_g^{\Gamma}(lh) \qquad\qquad (4.23)$$

Figure 4.13 shows the intrinsic carrier concentration in Ge as a function of biaxial strain in the film. Both valence bands become closer in energy to the conduction band as a result of the strain. As a result, the intrinsic carrier concentration increases. However, as seen in Figure 4.11, the shift of the heavy hole band is very small. Since this band has a much higher density of states than the light hole band, the overall increase in intrinsic carrier concentration is relatively small. We can conclude that the effects of biaxial strain on the noise properties of Ge diodes due to increases in the intrinsic carrier concentration is expected to be small.

We note that the leakage current in our diodes is higher than the theoretical limiting case due to defects in the film or at the Ge/Si interface, thus preventing us from experimentally measuring the intrinsic carrier concentration.

Ge ni vs. biaxial strain
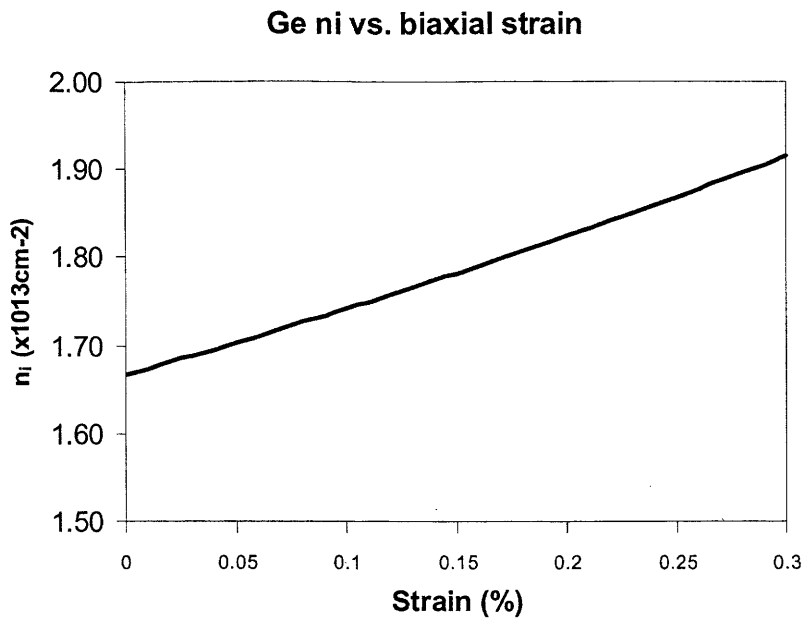
Figure 4.13 Intrinsic carrier concentration in Ge as a function of biaxial strain.

The shifting of the light hole band with respect to the heavy hole band will result in a decreased density of states in the valence band available for optical absorption. The number of available states sets an upper limit on the amount of generated carriers, and therefore on the photocurrent. The number of states in the light hole band up to the energy of the heavy hole band was calculated using equations 4.10, 4.11a, and 4.12b and assuming an energy splitting of 20meV between the light and heavy hole bands. The number of states was calculated to be $\sim 2 \times 10^{18}/cm^3$, which for a 1μm film would be $2 \times 10^{11}/cm^2$. If we assume carrier velocities of $10^5 cm/s$, the transit time of carriers is at most $10^{-9}s$ across the depletion width. Assuming all states have excited electron-hole pairs contributing to the photocurrent, this film would be able to support a current density of $28A/cm^2$, much higher than needed. Therefore, it would appear that the reduction in

88

valence band density of states will not cause the films to become optically transparent at

for optical power densities of interest.

Chapter 5: CMOS-compatible integrated Ge photodetectors

Photoreceivers are an integral part of optical communications networks. In current networks, a signal is often transduced from optical to electrical and back to optical several times before reaching its final destination. Ge is an ideal candidate for low cost, high performance photodetectors because of its compatibility with existing silicon processing, its high carrier mobility, and its high optical absorption at telecommunications wavelengths [82].

In this chapter we demonstrate for the first time CMOS-compatible fabrication of Ge photodiodes integrated on a Si substrate. The diodes are made from epitaxial films or mesas grown directly on Si by UHV-CVD. The leakage current of the diodes made from 700C planar films is 32mA/cm^2 with an edge leakage component of 0.41mA/cm. The responsivity is 0.26A/W at 1550nm, which is near the theoretical limit for the film thicknesses used. Furthermore, the responsivity of the photodiodes is shifted to longer wavelengths than for diodes fabricated from bulk Ge. This shift is due to a strain-induced band gap shrinkage resulting from the growth process, described in chapter four.

This chapter begins by presenting a brief background of prior work done on Ge photodetectors. We then discuss the experimental procedure used to process the photodiodes. Little attention is given here to Ge growth, as it is covered in detail in chapter three. Attention is devoted to subsequent processing, such as implant, anneal and etch conditions. The success of the current process was due to careful process development and utilization of simulations, prior work in the literature, and advice from

experienced researchers. The latter part of the chapter is devoted to the presentation and analysis of the electrical and optical properties of the photodiodes.

Section 5.1   Ge photodetector background

After the first attempt at fabricating a Si/Ge heterojunction photodiode by Donnely and Milnes in the 1960's, no significant work followed until the work of Luryi et al. in 1984 [83]. Much work has since been done in the field, and excellent reviews have been given by Masani [34] and Luan [62].

Luryi and coworkers introduced a 1.8μm thick graded buffer layer to prevent island growth and separate the active instrinsic region of the diode from the highly dislocated Si/Ge interface region. The diode, which was grown by MBE, exhibited an external quantum efficiency of 40% at 1.3μm and a dark current of 50mA/cm^2. Later, by introducing a 10 period 10 nm Ge$_{0.7}$Si$_{0.3}$/50 nm Ge superlattice embedded in the buffer layer just below the Ge intrinsic layer, they were able to reduce the dislocation density in the active region to 5x10^7 cm^{-2} and the leakage current to 0.4mA/cm^2. However, the quantum efficiency was reduced to 3% at 1.3μm.

Aiming to further reduce the dark current, Temkin and coworkers introduced a new device structure with the active layer composed of a coherently strained Ge$_x$Si$_{1-x}$/Si strained-layer superlattice (SSL) and used a waveguide configuration to compensate for the reduced absorption [84]. This idea is based on bandgap calculations by People [85] predicting that strained Si$_{1-x}$Ge$_x$ alloys coherently grown on Si have a smaller bandgap compared to relaxed Si$_{1-x}$Ge$_x$ alloys. Lang and coworkers later verified this prediction [86]. With x > 35%, materials with a bandgap lower than 1300 nm and 1550 nm can be grown on Si with very few dislocations. A device with an external quantum efficiency of

10.2% at 1.3μm with a reverse bias of 10V was demonstrated for a sample with x = 60% [87]. The dark current was 7.1mA/cm^2 at this bias. Other SSL based photodiodes have also been reported [88-91]. The disadvantage of strained-layer Si$_{1-x}$Ge$_x$/Si superlattices is the low absorption coefficient, which is only about 21 cm^{-1} at 1300 nm for x = 60% [86, 92], requiring long waveguide structures for high efficiency.

Samevedam and coworkers, from the Fitzgerald group, have fabricated Ge p-n diodes by using a UHV/CVD grown graded buffer to grade from Si to Ge with a dislocation density of 2 x 10^{6}cm^{-1} [93]. More recently Jungwoo and coworkers have used plasma enhanced chemical vapor deposition (PECVD) to grow a 1μm thick Ge layer on top of a 10μm SiGe graded buffer for use as a photodetector [94]. The Ge layer had a dislocation density of 10^{5}cm^{-2} and an rms surface roughness of 3.28 nm. A metal-semiconductor-metal (MSM) interdigitated p-i-n photodetector with 2μm finger spacing was fabricated and exhibited a bandwidth of 3.8 GHz at 5 V reverse bias. The external quantum efficiency was 49% at 1.3 μm.

Colace and coworkers reported an MSM photodiode based on a thick relaxed Ge layer grown on Si with the use of a low-temperature-grown Ge buffer layer [95]. The diode exhibited a responsivity of 0.24 A/W at 1.3 μm. Luan grew similar layers by UHV/CVD and introduced a cyclic anneal process to reduce the dislocation density to the low 10^{7}cm^{-2}, reporting responsivities of 550mA/W at 1.3μm and 250mA/W at 1.55μm [96]. The photodiodes in this work build upon the work of Luan.

Section 5.2   Experimental procedure

The fabrication process can be summarized by the following steps, each of which is described in detail below:

1) Preparation of SiO$_2$ rings on Si wafer that act as borders of Ge mesas. (This step does not occur for diodes made from blanket films.)

2) Epitaxial growth of Ge on p+ (100) Si substrates patterned as in step 1 (for mesa diodes) or unpatterned (for diodes from blanket films). Epitaxial growth is followed by cyclic annealing for dislocation density reduction.

3) Deposition and patterning of 0.3μm low temperature oxide (LTO) to passivate the Ge surface and define the area for the top contact to the diode.

4) Deposition of 0.2μm poly silicon layer

5) Blanket phosphorous implant and activation anneal to form the n-contact to the top of the diode. The implant is designed so that the tail of the implant extends past the Si/Ge interface, ensuring that the interface does not lie within the depletion region of the diode.

6) Patterning and etching of poly silicon top layer to define top contacts. The etching is done in a PlasmaQuest using a selective etch with a very high selectivity to the underlying SiO$_2$ layer.

A cross-section schematic of the completed diode is shown below in Figure 5.1 for diodes made from mesas and blanket films.
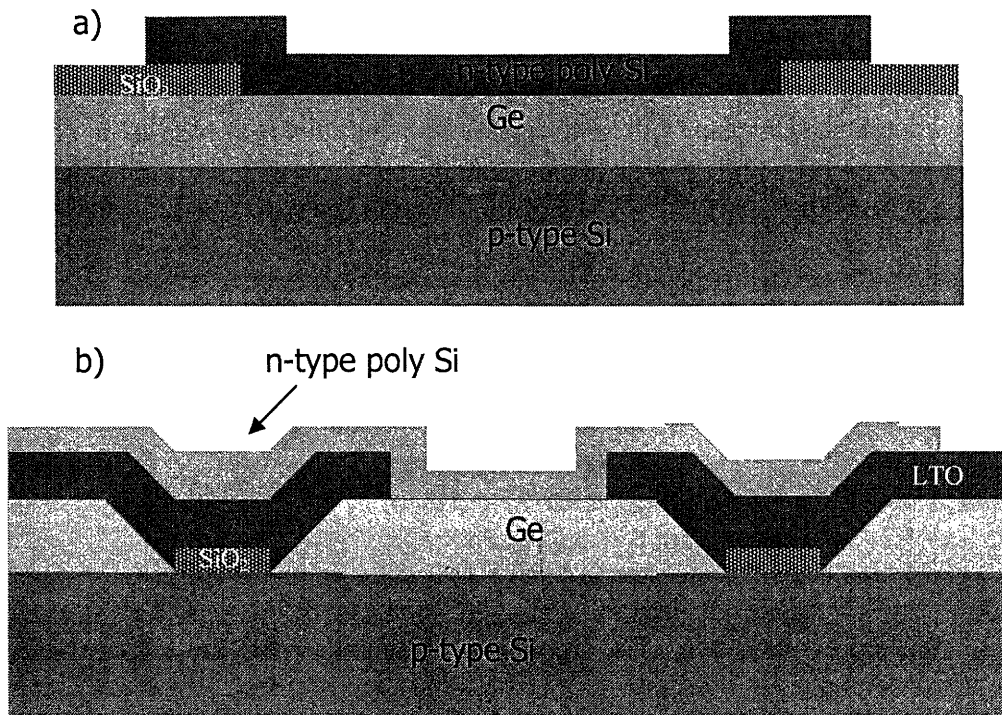
Figure 5.1 Cross-section of diode fabricated from a) blanket film and b) mesa

Section 5.3 Preparation of SiO₂ rings on Si substrates prior to Ge growth

For diodes made from selectively grown Ge mesas, the first step is to create a patterned oxide template to define the areas for Ge mesa growth. The process used to create the oxide rings is described in chapter three. Diodes were fabricated ranging in diameter from 10 to 300 microns. The diameter given is the diameter of the oxide ring, which defines the outermost edge of the diode. The mesa top and phosphorous implant area that define the area of the top contact are a few microns smaller.

Section 5.3.1 Epitaxial growth and cyclic annealing of Ge films

The epitaxial growth and cyclic annealing procedures are described in chapter three, as well as in other publications [52, 62]. Diodes were fabricated from mesas as well as blanket films. Two annealing conditions were also investigated. The first is a cyclic anneal of ten cycles between 700C and 900C, with the temperature held for ten minutes at each step. This anneal condition was shown by Luan to yield films of high quality from which high efficiency photodiodes were fabricated [97]. The second is a one hour anneal at 900C, which was shown in chapter three to yield a similar dislocation density as the cyclic anneal. By comparing diode performance from the two annealing conditions, we can determine if cyclic annealing is necessary for high quality diodes.

Section 5.3.2 Deposition and patterning of passivating LTO layer

A 0.3µm layer of LTO was deposited to passivate the surface of the Ge films. Prior to deposition in a low pressure diffusion tube, the wafers were cleaned using the following cleaning recipe:

1. $NH_4OH:H_2O$ 1:4 for 5 minutes
2. rinse
3. H_2O_2 for 30 seconds
4. rinse
5. $HF:H_2O$ 1:50 for 30 seconds
6. rinse
7. H_2O_2 for 30 seconds
8. rinse
9. $HCL:H_2O$ 1:4 30 seconds
10. rinse
11. dry

A standard RCA clean cannot be used, because the etch rate of Ge in RCA is 40µm/min and the surface is left rough, making the film useless for device application

[98]. This cleaning procedure has been developed in Dimitri Antoniadis' research group at MIT and is a modified version of what others have proposed [99-101]. The deposition was then performed in a low pressure diffusion tube with the following deposition parameters: Temperarure = 400C, pressure = 200mTorr, front O_2 flow = 75cc, rear O_2 flow = 100cc, front SiH_4 flow = 50cc, rear SiH_4 flow = 75cc. The deposition rate is approximately 50A/min.

Windows were then patterned in the LTO layer using standard lithography to define the area for the top contact of the diode. Buffered Oxide Etch (BOE) was used to etch the LTO. The etch rate is ~0.1μm/min. Since BOE does not etch Si or Ge, the etch stops at the interface.

Section 5.3.3 Deposition of 0.2μm blanket poly silicon or amorphous silicon film

A 0.2μm blanket Si layer was then deposited to serve as a top contact for the diode. The same clean was used as for the LTO deposition, and the deposition was performed by flowing 100cc SiH4 (pressure maintained at 250mTorr) at 600C, yielding a deposition rate of 10nm/min. Poly Si was deposited on the first diodes, but surface roughess was observed near the edges of the wafers. Diodes from these areas had poor performance. The deposition temperature was lowered from 600C to 560C for subsequent diodes, which resulted in amorphous silicon that was optically smooth across the entire wafer.

Section 5.3.4   Phosphorous implant to form top n-contact of diode

A 5×10^{15}/cm^2 phosphorous dose at 100 keV was implanted into the Si/Ge

structure to form the top n-contact of the diode. To ensure that the diode junction would

be in the Ge, implant conditions were chosen so that the tail of the implant distribution

would extend into the Ge film. Simulations were performed for a phosphorous implant

dose of 5×10^{15}/cm^2 into a 2100 angstrom poly Si film on Ge. 90, 95, and 100 keV

implant energies were simulated, and the results are shown in Figure 5.2. A

phosophorous concentration of $\sim 1.5 \times 10^{20}$/cm^3 is predicted at the Si/Ge interface for an

implant energy of 100 keV, corresponding to an atomic concentration of 0.34%. this is

slightly less than the reported solubility of P in Ge at 600C of 0.45% [102]. As

implanted, the tail of the phosphorous extends roughly 40 nm into the Ge.

This implant dose exceeds the amorphizing dose of 3×10^{14}/cm^2 [103], so a steep

activation annealing behavior is observed as the Si recrystallizes [104]. For a 30 minute

anneal, maximum P activation occurs at 600C [105]. The reason for this is that P is

incorporated into the Si lattice as it recrystallizes, which occurs at 600C. The same

researchers also reported that for high doses ($> 1 \times 10^{16}$cm^{-2} in their study), increased sheet

resistance is observed due to incomplete activation.

Activation anneal conditions were experimentally studied for our implant dose to

determine the thermal budget required to activate the implant. A blanket film of 0.2μm

poly Si on 0.3μm LTO was with the same implant conditions as for the diodes was used.

Anneals were performed at 500C, 600C, and 650C in a diffusion tube with N$_2$ ambient

for times ranging from three to 30 minutes. It was found that a minimum anneal of 15

minutes at 600C was necessary to activate the anneal. A large amount of scatter was

present in the measured sheet resistances, but for times longer than fifteen minutes and for temperatures above 600C, a significant fraction of the phosphorous was activated. Assuming uniform dopant distribution and a mobility of 100 cm^2/Vs, corresponding to a doping concentration of $10^{20}cm^{-3}$, the dopant activation is calculated at 40% in the best sample. Given that the carrier concentration is not uniform and not completely confined to the Si layer, this value is reasonable.

Activation of P in Ge has been shown to occur between 200 and 475C [106, 107], so activation will occur for any conditions that activate P in Si. However, we need to ensure that the P does not diffuse too far into the Ge, shortening the depletion width of the p-i-n diode. The Diffusivity of P in Ge is reported as approximately $2x10^{-14}$ cm^2/s at 600C and $9x10^{-14}cm^2/sec$ at 650C.[108] Other research has reported a diffusion enhancement at high concentrations, the diffusion coefficient differing by about an order of magnitude between high and low concentrations.[109, 110] In our calculations we use the highest reported value of $2x10^{-14}$ cm^2/s.

The diffusion length is shown in Figure 5.3 as a function of annealing time for these two temperatures. Note that in an actual anneal the wafer will take a finite amount of time to equilibrate to the furnace temperature, so the real diffusion length will actually be shorter than the calculated one. This assumes that the reported diffusion coefficient is the same in our thin films, which we know to be strained.

Poly Si   Ge
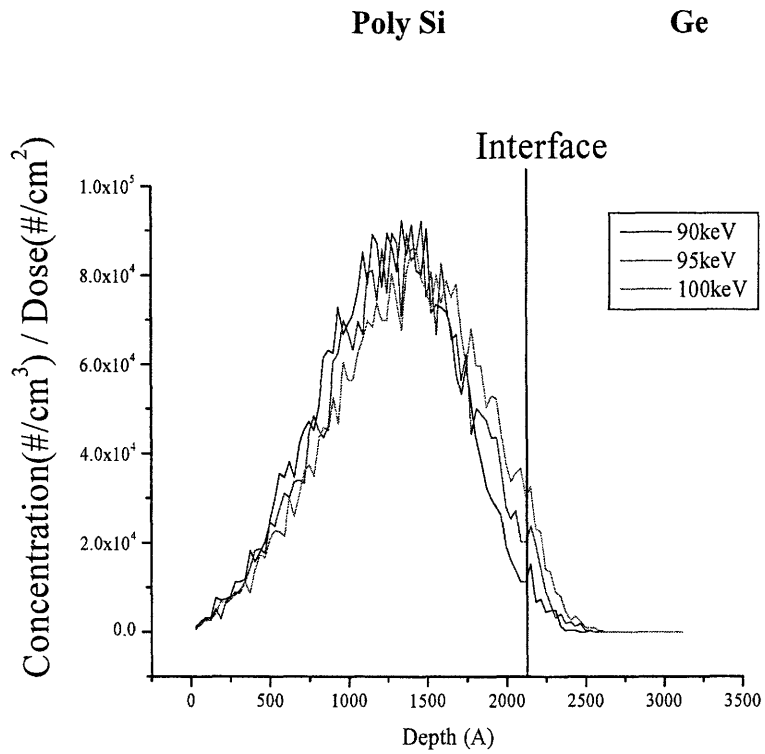
Figure 5.2 Simulated implant profile for P in Si/Ge. Simulation courtesy of Jifeng Liu.
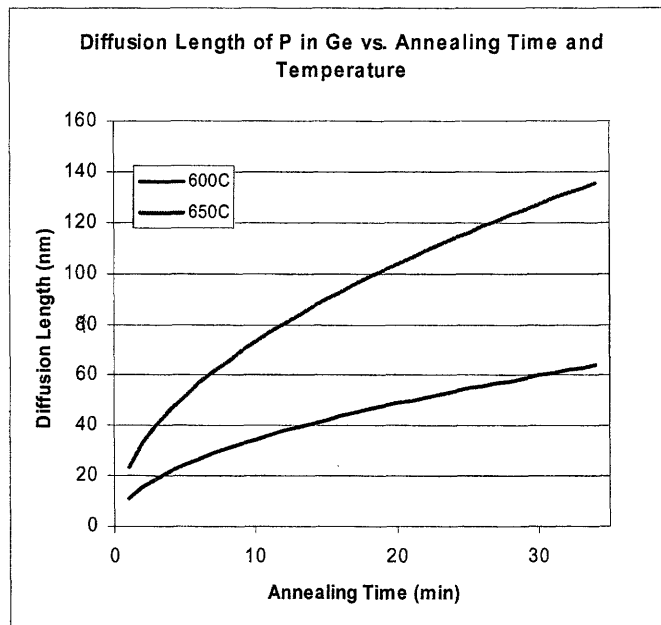
Figure 5.3 Diffusion length of P in Ge vs. Annealing Time and Temperature

99

We want to minimize the diffusion of P in Ge while still activating the P in the Si. A thirty minute anneal has been used successfully both in the literature and by other groups at MIT to activate P in polySi, so we should use this time, if possible. From Figure 5.3 we can see that the diffusion length is approximately 60nm for a 30 minute 600C anneal, as opposed to 42 nm for a 15 minute anneal. Adding 40 nm for the implantation depth, this gives a total junction depth of ~100nm, which is acceptable for our diodes. We have therefore chosen a 600C 30 minute activation anneal.

Section 5.3.5 Patterning and etching of poly silicon top contact

Etch selectivity between Si and SiO2 is the primary concern for this final processing step. A high selectivity allows for complete etching of the poly Si without concern of etching through underlying LTO layer, which acts to passivate the Ge surface. A plasma etch with a high concentration of F_2 radicals is an effective method for selectively etching SF_6 [111]. The etch was performed in a PlasmaQuest tool, which is an electron cyclotron resonsance (ECR) enhanced reactive ion etcher (RIE) and chemical vapor deposition (CVD) system. The following parameters were found to give a poor Si:SiO$_2$ selectivity of near 1:1 and an LTO etch rate of ~400A/min.

O$_2$ flow: 10 sccm
SF$_6$ flow: 50 sccm
Pressure: 30 mTorr
Source power: 400W
Bias (RF) power: 20W
Temp: 25C

Raising the pressure to 50mTorr, the impact energy of the incoming ions was reduced, thereby significantly lowering the LTO etch rate, which is an endothermic reaction and requires energy from incoming ions. The O_2 flow was also reduced to 5 sccm. The following process parameters were found to increase the Si etch rate to 2000A/min and reduce the LTO etch rate to < 100A/min, allowing for a very selective etch.

O_2 flow: 5 sccm
SF_6 flow: 50 sccm
Pressure: 100mTorr
Source power: 400W
Bias (RF) power: 20W

After etching, the photoresist was removed by ashing prior to diode measurement.

Section 5.4   Results and Discussion

Diodes exhibit low leakage currents and excellent responsivity. The responsivity is also extended to longer wavelengths, as a result of the strain-induced bandgap reduction in our Ge. The absolute responsivity is also high, indicating nearly ideal internal quantum efficiency.

Figure 5.4 shows the top views of diodes fabricated from both blanket films and selectively grown mesas. These correspond to the diode structures shown in Figure 5.1 and Figure 5.2, respectively. The facets on the Ge mesa are clearly visible in Figure 5.4b.
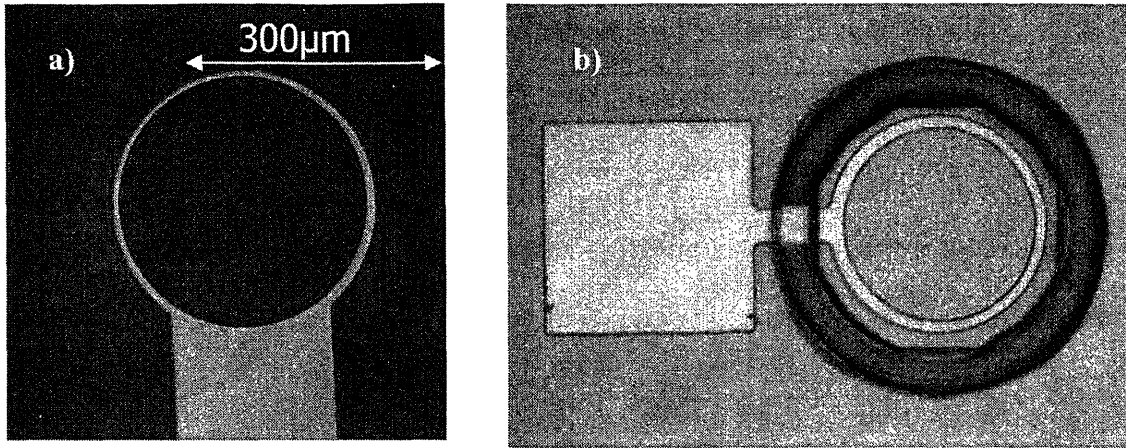
Figure 5.4 Optical micrograph of CMOS processed Ge photodiodes from a) blanket film and b) selectively grown mesa.

Section 5.5   Reverse leakage characteristics

Figure 5.5 shows the I-V characteristics of planar diodes fabricated from films grown at 700C and cyclic annealed to reduce dislocation density. Data for 10 and 300µm diameter diodes are shown. Although the area of these diodes differs by roughly three orders of magnitude, the reverse leakage current only differs by two orders of magnitude. This indicates that bulk leakage is not the only source of leakage current. The other likely source of leakage current is at the diode edge, where doping profiles, electric fields, and film passivátion are all changing. To separate the bulk and perimeter components of the leakage, we fit diode data to the following model, where c_p and c_a are the perimeter and edge coefficients of leakage current and r is the diode radius.

$$I_r = c_p 2\pi r + c_a \pi r^2 \qquad (5.1)$$
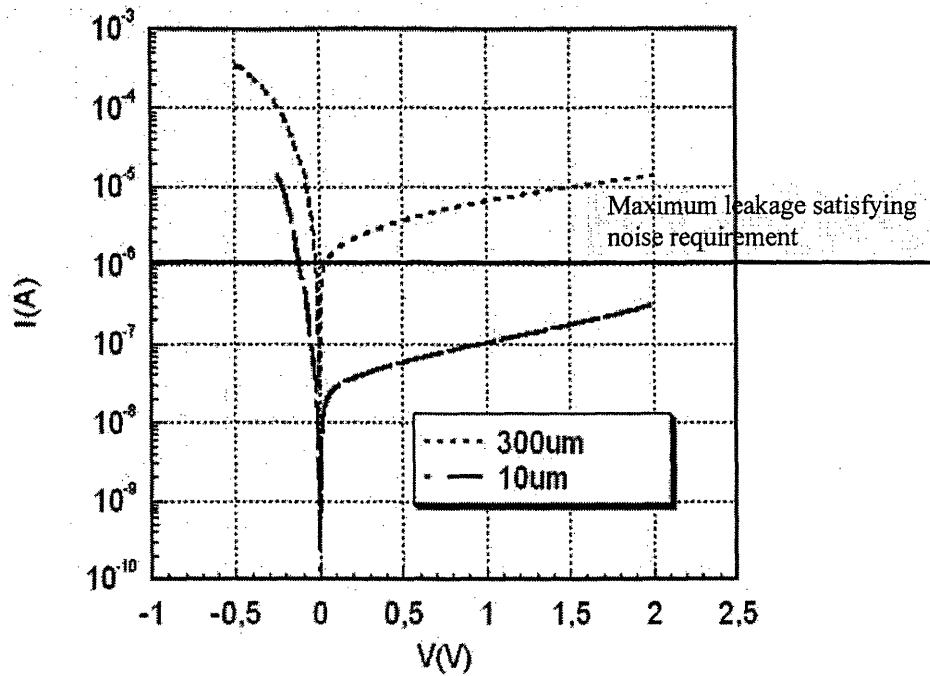
Figure 5.5 I-V curves for planar diodes fabricated from Ge film grown at 700C. Measurement courtesy of Nok Jongthammanurak.

This assumes that the leakage current has a component scaling with perimeter length and another with area. Reverse leakage data for diodes of diameter 10, 20, 50, 100, 200, and 300 μm were used. The data fits this second order polynomial model very well, allowing us to extract the edge and bulk leakage components of the diode. The edge leakage of the diodes is found to be 0.41mA/cm and the bulk leakage is 32mA/cm^2 at a reverse bias of 2V. Figure 5.6 shows the perimeter and bulk leakage components of the diode leakage as a function of diode radius. For large diodes the majority of the leakage is through the bulk, whereas for small diodes perimeter leakage dominates. The cross-over point is at a diameter of approximately 250μm. Since many applications require small diodes, the key to further improving diode leakage is to lower the perimeter leakage current; the bulk properties of the film are not the limiting factor.

For comparison, the theoretical reverse leakage current was calculated, which gives a lower limit of the expected leakage current. The equation for the reverse leakage current can be found in many texts [16], and a doping level of $10^{18}/cm^3$ was assumed for both the n and p side of the device. At this doping level electron and hole mobilities are 2000 and 270 cm^2/Vs, respectively. [16] Minority carrier diffusion lengths of 0.3 and 0.2 cm were used for electrons and holes, respectively. [112] Using these parameters a theoretical reverse leakage current of $2 \times 10^{-8} A/cm^2$ is calculated, which is several orders of magnitude less than what we observe in our diodes. The extra leakage can come from many sources, such as dislocations and point defects in the Ge films, misfit dislocations at the SiGe interface, and/or incomplete passivation of the Ge. Although our leakage current is much higher than the theoretical limit, it is low enough for the intended application and is similar to what other researchers have achieved.
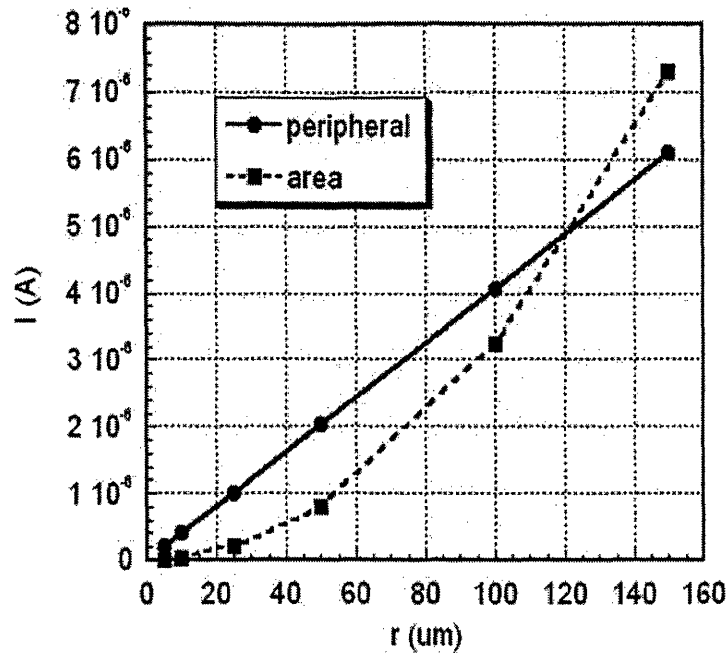
Figure 5.6 Edge and bulk components of diode leakage current as a function of radius. (2V reverse bias) Measurement courtesy of Nok Jongthammanurak

Figure 5.7 shows the I-V curves for 300µm diodes with different Ge film fabrication parameters. The 700C film annealed for one hour at 900C yields a flatter reverse leakage current than for the cyclic annealed film. Since a one hour anneal has been shown in this work (chapter three) to be effective in reducing the dislocation density as well as cyclic annealing, it is of interest to explore the diode performance of such films. The specific mechanism of this improvement has not been determined, but it is possible that the one hour anneal is more effective in eliminating point defects or other sources of charge traps. The flatter reverse leakage current has been observed in multiple samples that have undergone a 900C one hour anneal. Although the one hour anneal yields a flatter reverse leakage current, the leakage current is higher than for the cyclic annealed film. The reason for this is not currently understood. We have also observed that films grown at a higher temperature have lower leakage current. It is possible that

105

higher growth temperatures yield films with fewer point defects, but further work will be required to understand the exact mechanism of the leakage current.

Figure 5.7 also compares the leakage current for diodes fabricated from mesas and blanket films. Mesa diodes have higher leakage current than diodes from the bulk film. This is not surprising, since the mesa edge provides a current pathway if not completely passivated by the deposited LTO.

700C Diodes from the same growth run
(583-1, 3, and 7)
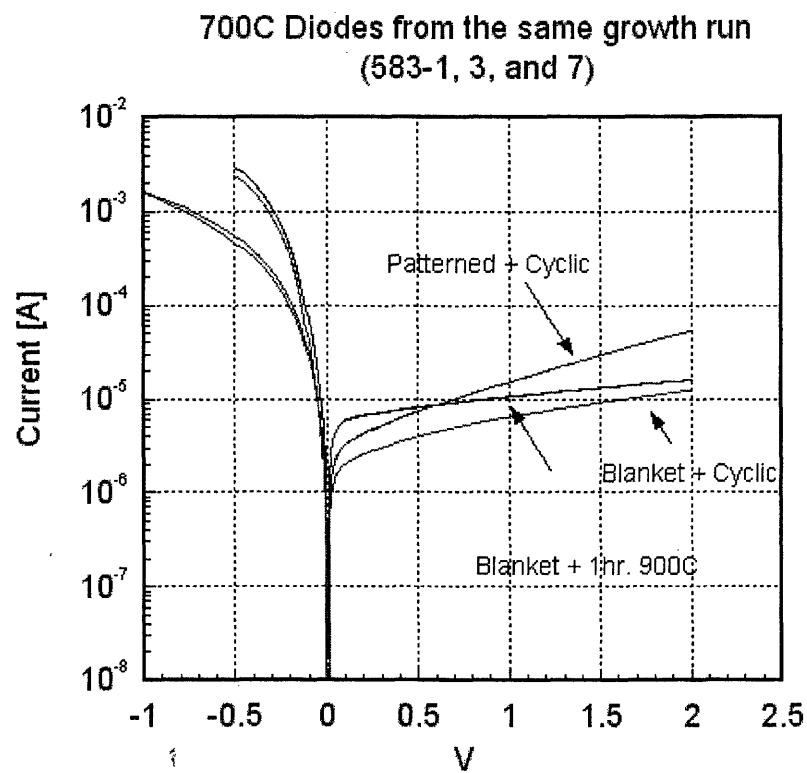
Figure 5.7 I-V curves of 300μm diodes with different fabrication conditions. Measurement courtesy of Nok Jongthammanurak.

Section 5.6   Ge diode responsivity

Photodiode responsivity has been measured as a function of wavelength for diodes fabricated from a 700C grown blanket film and is shown in Figure 5.8. The

responsivity is 260mA/W at 1550nm. Although the exact depletion width of the diode is not know, it is appriximately one micron. We can then calculate an expected responsivity assuming an absorption coefficient of 2000 cm^{-1}. This value has been obtained by shifting the absorption curve for bulk Ge [8] to lower energies by 30meV. Using equations 2.7 and 2.8 and assuming no reflected light, we calculate an expected responsivity of 145mA/W, well below what we observe. It is possible that our depletion width is wider than one micron, our absorption coefficient is higher than 2000 cm^{-1}, or a combination of both. In any case, we are confident that the diodes have high internal quantum efficiency and are collecting the vast majority of photogenerated carriers.

Figure 5.9 shows the responsivity curve for a diode fabricated from a 700C blanket film compared to calculated responsivity using absorption data for bulk Ge. The responsivity curve from our diode is shifted to longer wavelengths by approximately 30nm, in agreement with the direct bandgap reduction present in our strained films, as discussed in chapter four.

Responsivity vs wavelength

No anti-reflection coating
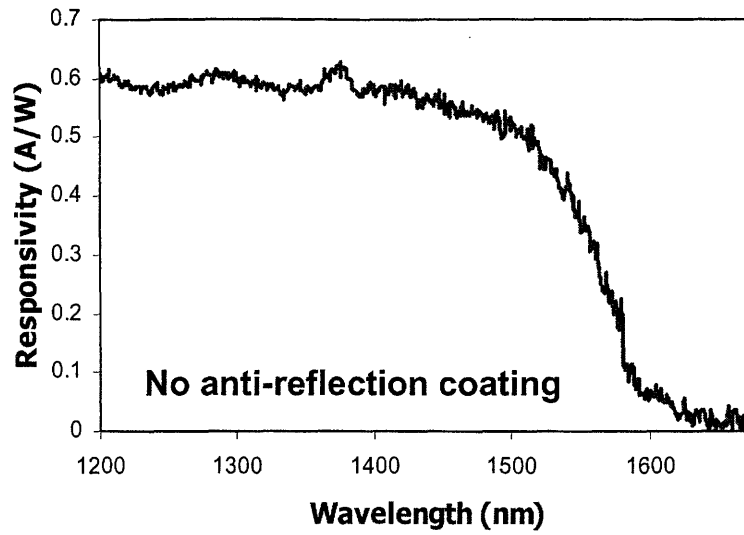
Figure 5.8 Responsivity of Ge diode fabricated from 700C blanket film and cyclic annealed.

Measurement courtesy of Nok Jongthammanurak.
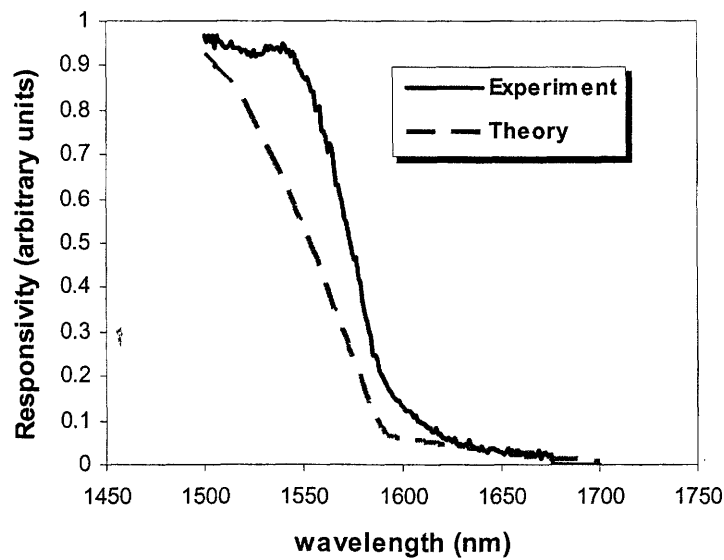
Figure 5.9 Diode responsivity of strained Ge compared to calculated responsivity using bulk Ge

absorption data. Calculation courtesy of Kazumi Wada.

Chapter 6:   Modulation of light using the Franz-Keldysh effect

Electro-optic modulators are an important part of optical networks, as they provide the means to encode optical data. Two types of modulators are currently in use, lithium niobate modulators and multiple quantum well (MQW) modulators, which are fabricated on InP substrates. Although both types are currently in use in long haul networks, significant difficulties exist to their integration into a silicon based microphotonics platform.

In this chapter we show that near-infrared (NIR) light can be modulated in Ge through the Franz-Keldysh effect. While further development is still needed, this offers the potential for a low cost CMOS-compatible electro-optic modulator. We begin by briefly reviewing the current modulator technologies in use today. We then discuss the Franz-Keldysh effect and prior work utilizing this effect to modulate light. Finally, we show experimentally that the absorption of NIR light can be increased in the Ge system by applying an electric field and compare this to what we would expect from theoretical calculations.

Section 6.1   Present Modulators and their capabilities and limitations

Two types of modulators are currently used in telecommunications, $LiNbO_3$ based modulators and multiple-quantum-well (MQW) modulators. Each of these modulators has advantages and limitations, which will be briefly discussed below.

Section 6.1.1 Lithium Niobate Modulators

LiNbO$_3$ modulators are constructed by forming a Mach-Zender interferometer of Ti-diffused waveguides in a LiNbO$_3$ crystal. By the application of a voltage, it is possible to change the effective path length in the arms of the interferometer to cause destructive interference. These modulators are a relatively mature technology and currently achieve modulation speeds of 20 GHz with modulation depths of 15dB. The required voltage is approximately 4V. Although LiNbO$_3$ modulators have been very successful to this point, several factors will hinder further progress:

1) Driving 4V to high frequencies is expensive.

2) Because they are made in single-crystal LiNbO3, they cannot be readily integrated on a Si (or InP) substrate for use with other devices.

3) Device sizes are several millimeters, making them an unattractive option for microphotonics

Section 6.1.2 InGaAsP MQW Modulators

MQW modulators use the quantum confined Stark effect to modulate the absorption of light. They are fabricated on InP substrates, with the active layers composed of InGaAsP. They possess several advantages over LiNbO3 modulators. While achieving the same modulation depths and speeds, they require lower voltages and are much smaller. Furthermore, they can be readily integrated with other III/V devices grown on InP substrates, such as lasers. Their main drawback to integration with Si microphotonics is that they cannot be integrated on a Si substrate without bonding.

Section 6.2   Franz-Keldysh Effect

The change in absorption coefficient of a semiconductor in the presence of an applied field is known as the Franz-Keldysh effect. This phenomenon, independently observed by Franz[113] and Keldysh[114], results in the absorption of photons with energies less than the bandgap of the semiconductor. The physical origin of this effect can be understood with the help of Figure 6.1, reproduced from [115].
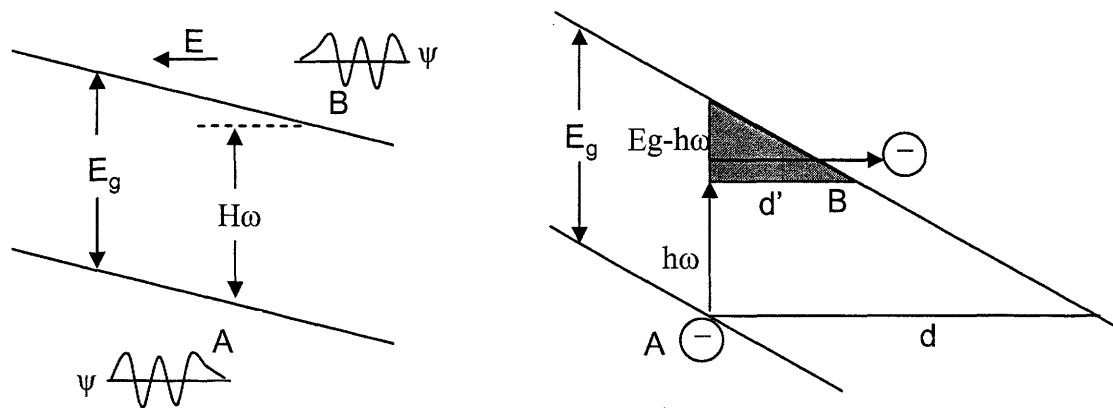
Figure 6.1 The Franz-Keldysh effect can be thought of as photon-assisted tunneling. With low electric field (a) tunneling is not posible, but with high field (b) carriers tunnel through a triangular barrier.

At the classical turning points, marked A and B, the wave function turns from oscillatory in nature to decaying. In the energy gap, the electron is described by an exponentially decaying function of the form $u_K e^{ikx}$, where K is imaginary. The distance AB decreases with increasing electric field, and the overlap of the wavefunctions within the gap increases.

For a valence electron to reach the conduction band, it must tunnel through a triangular barrier of height E_g and thickness d, given by $d = E_g/qE$. However, with the aid of an absorbed photon (of energy less than the bandgap) the barrier height is reduced to

$E_g - h\omega$ and the barrier thickness is reduced to d' = $(E_g - h\omega)/qE$. The overlap of the wavefunctions increases further, and the valence electron can tunnel to the conduction band. The Franz-Keldysh effect can be thought of as photon-assisted tunneling.

Section 6.3   *The Franz-Keldysh Effect in Ge*

The Franz-Keldysh effect has been investigated in Ge, with the most detailed work done at low fields and near the band edge.[116, 117] Although Ge has an indirect band gap, the direction transition is at 0.8 eV, corresponding to 1.55um light. Near this energy, the absorption coefficient increases abruptly from $\sim 10^2$ to 10^4 cm^{-1}. The Franz Keldysh effect does allow for strong changes in absorption near the direct transition, as has been demonstrated by Frova and Handler by measuring the absorption spectrum of light through a reversed biased p-n diode as a function of electric field.[118] Their data showing the absorption coefficient as a function of wavelength and electric field is shown in Figure 6.2.
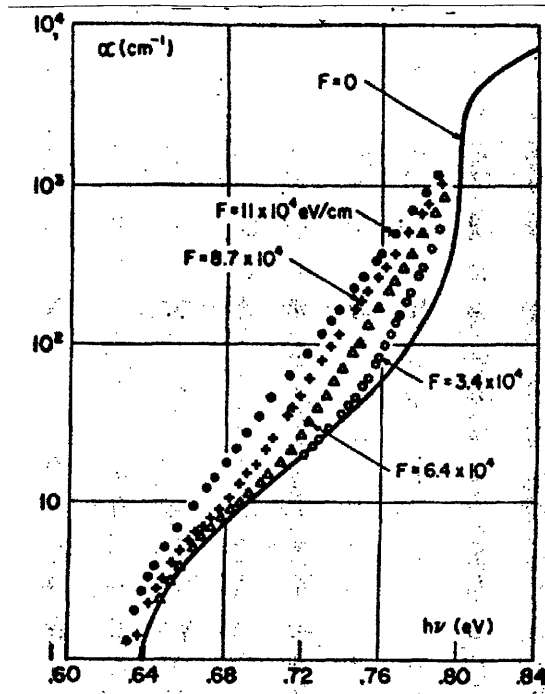
Figure 6.2 Ge absorption data as a function of electric field. (Frova and Handler,)

Section 6.4 Franz-Keldysh effect in other materials systems

The Franz-Keldysh effect has been used to make electro-optic modulators in GaAs, with most of the work being done by a German group led by G.H. Dohler. Using a n-i-p-i structure to achieve high electric fields, they have achieved a change in the absorption coefficient of 2000 cm^{-1} near the band edge.[119, 120] This has been achieved with a change in applied bias of only 3.3V, corresponding to a maximum internal electric field of 6.3x10^5 V/cm.

This same group has achieved a modulation ratio of 6:1 using a vertical n-i-p-i structure 3.9 um thick.[121] By using a waveguide structure, they were able to achieve a modulation ratio of 30 dB. The structure was 900 um long and required an applied bias of 6.5 V.[122]

113

Some work has been done to examine Franz-Keldysh effect in silicon, but it has been found that the effect is only significant near the band edge, where the absorption is very low.[123, 124] This prohibits its use in practical modulators.

Section 6.5   Simulations of achievable index changes in Ge and SiGe

The magnitude of the achievable index change, both real and imaginary, can be calculated using the generalized Frzna-Keldysh theory of electromodulation, developed by Shen and Pollack [125]. This theory states that the dialectric function can be varied by changes in both the AC and DC components of the electric field. The variation can be expressed as

$$\delta\varepsilon(E, \mathrm{E}_{dc}, \mathrm{E}_{ac}) = \varepsilon(E, \mathrm{E}_{dc} + \mathrm{E}_{ac}) - \varepsilon(E, \mathrm{E}_{dc} - \mathrm{E}_{ac}) \qquad (6.1)$$

$$= \Delta\varepsilon(E, E_{dc} + \mathrm{E}_{ac}) - \Delta\varepsilon(E, \mathrm{E}_{dc} - \mathrm{E}_{ac})$$

where E is the photon energy and

$$\Delta\varepsilon(E, \mathrm{E}) = \varepsilon(E, \mathrm{E}) - \varepsilon(E, 0) \qquad (6.2)$$

For an Mo (three-dimensional) critical point the quantity $\Delta\varepsilon(E,E)$ from above can be written as [126-128]

$$\Delta\varepsilon(E, \mathrm{E}) = (B/E^2)(\hbar\theta)^{\frac{1}{2}}[G(\eta) + iF(\eta)] \qquad (6.3)$$

where B, which is related to matrix elements, is defined on p. 172 of reference 14. The other parameters are defined as

$$(\hbar\theta)^3 = e^2\hbar^2\mathrm{E}^2/2\mu_{par} \qquad (6.4)$$

$$\eta = (E_o - E)/\hbar\theta \qquad (6.5)$$

114

where μ_{par} is the reduced effective mass in the direction of E and Eo is the energy

gap. $G(\eta)$ and $F(\eta)$ are given by [126, 128]

$$G(\eta) = \pi\left[Ai'(\eta)Bi'(\eta) - \eta Ai(\eta)Bi(\eta)\right] + \eta^{\frac{1}{2}}H(-\eta) \quad (6.6)$$

$$F(\eta) = \pi\left[Ai'^2(\eta) - \eta Ai(\eta)\right] - (-\eta)^{\frac{1}{2}}H(-\eta) \quad (6.7)$$

where Ai(η), Bi(η), Ai'(η), and Bi'(η) are Airy functions and their derivatives and

H(-η) is the unit step function [126, 128].

We have observed the Franz-Keldysh effect in our Ge diodes by measuring the

responsivity at different reverse biases, or higher electric fields. As shown in Figure 6.3,

we observe increased responsivity above the bandgap as the electric field is increased.

This is in relative agreement with the calculated responsivity change, which is also

shown. The calculation is made by using the above equations to calculate the change of n

and k for Ge in the presence of an applied field, and using the result to calculate the

resulting change in responsivity of a p-i-n diode as a function of wavelength.

Mathematica code for calculating the change in n and k is found in Appendix B.

Due to the varying electric field within the diode (as a consequence of the doping

profile) we are unable to extract the change in absorption of our strained Ge as a function

of electric field. Still, we have observed the Franz-Keldysh effect in our epitaxially

grown Ge as evidenced by the responsivity increase with increased reverse bias. Because

this increase only evident at wavelengths above the band gap, we know that it is not

simply due to increased carrier collection efficiency.

For an absorption based modulator, the optimal wavelength is one slightly lower

in energy in the direct band gap, as that is where the largest change in absorption can be

realized. For a Mach-Zender structure, a wavelength far from the band gap will be used,

as only a small change in the index is desired. For pure Ge, this wavelength could be as long as 1800nm.

Unfortunately, in a modern communications system we cannot choose the wavelength to modulate simply on the band structure of Ge. The wavelengths of interest are 1.3 and 1.55μm, and we must make a modulator that operates at these wavelengths. To do this we can change the band gap to shorter wavelengths by alloying with Si. This is the motivation of the Si rich SiGe work discussed in Chapter three. By choosing an appropriate composition and device structure, modulation of 1.55μm light should be achievable.
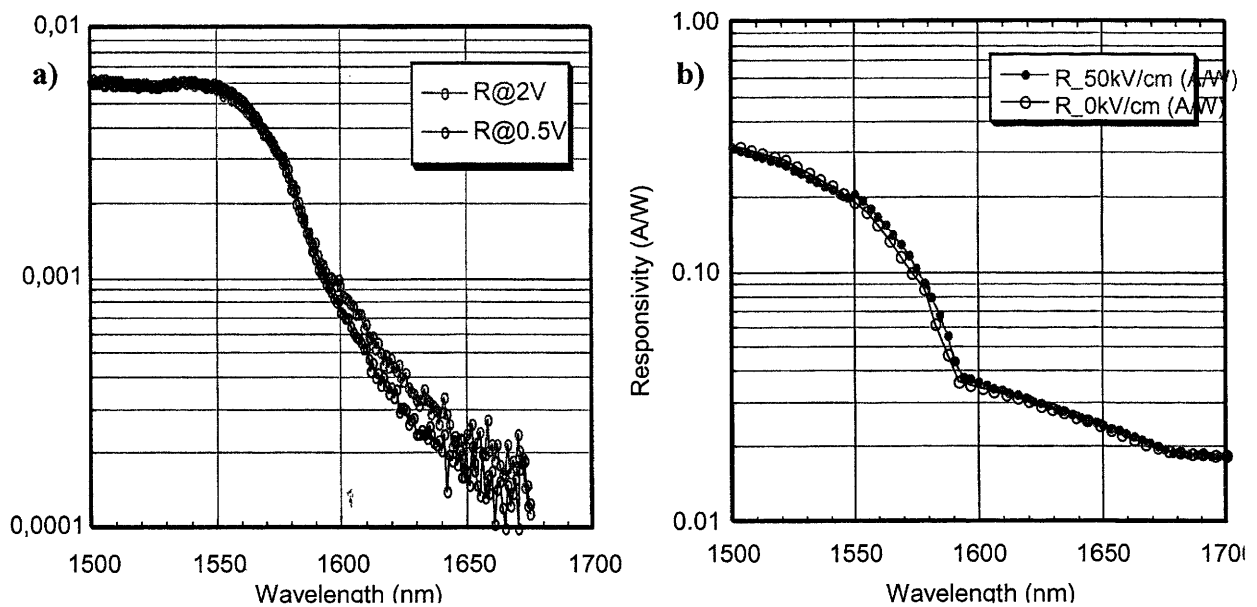
Figure 6.3 a) actual and b) calculated change in responsivity of Ge diode with increasing electric field

Chapter 7:   Summary and future work

Section 7.1   Summary

This thesis has focused on the development of Ge and SiGe technology for photodetectors and electro-optic modulators. Design considerations have been explored in addition to experimental work. Experimental results have been shown to be consistent with theory. Below is a summary of the key points of each chapter.

In chapter two we considered many design and integration issues of monolithically integrated Ge photodetectors. Design plots were used to show the relationships between depletion width, area, photocurrent, responsivity, and bandwidth. The performance advantages of waveguide integration were illustrated, and it was shown for the first time that waveguide integration allows for a potentially higher optical saturation point, as a result of the ability to use devices with thin depletion regions.

Chapter three was devoted to Ge and SiGe epitaxial growth by ultra-high vacuum chemical vapor deposition (UHVCVD). For pure Ge, high-yield selective epitaxial growth of Ge was been demonstrated by two methods. Photodetectors made from these selectively grown mesas were demonstrated in chapter four. Additionally, the ability to grow high Ge content SiGe directly on Si by utilizing a low temperature Ge buffer layer was demonstrated, and thermal annealing was shown to reduce the dislocation density of both Ge and SiGe films to the low 10^7cm^{-2} range.

In chapter four we showed that the direct bandgap in our Ge films can be engineered by controlling the amount of tensile strain in the film. By utilizing the difference in thermal expansion coefficient of Ge and the underlying Si substrate, tensile

strain was introduced in the films, which results in a decrease in the direct transition

energy, E_g^{Γ}. Theoretical predictions agree with our experimental results. The intrinsic

carrier concentration of strained Ge was calculated, predicting a 15% increase in n_i for

0.2% tensile strain.

Chapter five was devoted to the processing of CMOS-compatible Ge p-i-n

photodetectors on Si substrates. To our knowledge, this is the first time Ge

photodetectors have been fabricated on Si using a completely CMOS process. Devices

exhibit good electrical and optical characteristics, and the responsivity is shifted to longer

wavelengths in agreement with the results of chapter four. SiGe p-i-n diodes were also

been fabricated, and the responsivity spectrums agree well with the bandgap

measurements of chapter three.

Chapter six was devoted to the modulation of near infrared light using the Franz-

Keldysh effect, which can be thought of as photon assisted tunneling of carriers from the

valence band to the conduction band. While this effect is weak for an indirect

semiconductor, near the direct band transition of Ge the effect is expected to be

significant. The Franz-Keldysh effect was experimentally demonstrated in Ge

photodetectors as an increase in responsivity for increased electric fields.

Section 7.2   Future work

Although we have realized improvements in Ge photodetectors, much more can

still be done. Introducing waveguide coupling would be a huge advance, and lowering

the leakage current further would open the door to more applications. Realization of a

working SiGe modulator would also be a significant achievement.

Successful integration of waveguides will require attention to both processing and design. Efficient coupling to Ge, which has an index of refraction of four, will require careful design. Designing a structure that can also be fabricated will require creativity and process know-how. Planarity of the waveguide as it interacts with the detector will likely be key, as will process complexity. A simple design with the least complexity possible should be sought after.

Better passivation of the Ge to further lower the leakage current would open up additional applications, such as near infrared cameras. In this thesis the only passivation explored was deposited LTO. Other promising passivating layers, such as a Si cap or Ge oxynitride were not explored, but could potentially offer better performance. Design changes could also be made to keep electric fields from the diode junction away from mesa edges, which could also lower the leakage current.

Much work is still needed to realize an electro-optic modulator in SiGe. A wider range of alloy composition may need to be developed than was shown in this work. Also, the decision of which type of design, linear absorption or interference (Mach-Zender), will perform better has not been answered. Much work in design simulation and fabrication is needed, but the realization of a truly CMOS compatible electro-optic modulator is a goal worth pursuing.

Fortunately, because several bright, hard-working researchers are continuing to work on these problems, the probability of success is high.

Appendix A: Code used to calculate mode profiles in 1D layered structures

The following Matlab code was written by Michael Watts

```
%Finite Difference Solution of the scalar wave equation (M. Watts)
close all;
clear all;

%%% Inputs
lambda = 1.55e-6; % Wavelength
npts = 601; % # of points in grid
n1 = 1.445; % index of layer 1
n2 = 1.445; % index of layer 2
n3 = 2.0;   % index of layer 3
n4 = 4.0+0.02467j; % index of layer 4
n5 = 3.5; % index of layer 5

w1 = 0.5e-6; % thickness of layer 1
w2 = 0.5e-6; % thickness of layer 2
w3 = 0.5e-6; % thickness of layer 3
w4 = 1.0e-6; % thickness of layer 4
w5 = 4.e-6; % thickness of layer 5
%%% end Inputs

%% Begin code

% Define constants
eps0 = 8.854e-12;
mu0 = 4*pi*1e-7;
c = 1/sqrt(mu0*eps0);
omega = 2*pi*c/lambda;

% generate mesh;
x = linspace(0,w1+w2+w3+w4+w5,npts).';
dx = x(2)-x(1);
x = x+dx/2;  % Offset x for improved accuracy / convergence

% Define the index distribution
n = zeros(size(x));
ind1 = find(x<w1);
ind2 = find(x>=w1 & x<(w1+w2));
```

```
ind3 = find(x>=(w1+w2) & x<(w3+w2+w1));
ind4 = find(x>=(w1+w2+w3) & x<(w1+w2+w3+w4));
ind5 = find(x>=(w1+w2+w3+w4));

n(ind1) = n1;
n(ind2) = n2;
n(ind3) = n3;
n(ind4) = n4;
n(ind5) = n5;

%Define dielectric constant such that Gauss' Law is satisfied
eps = n.^2*eps0;
eps(2:end) = (n(1:end-1).^2+n(2:end).^2)*eps0/2;

%Write the Scalar Wave Equation in Tridiagonal form
udiag = ones(size(x(1:end-1)))./dx.^2;
cdiag = -2*ones(size(x))./dx.^2+omega^2*mu0*eps;
ldiag = ones(size(x(2:end)))./dx.^2;

% Generate tri-diagonal matrix
A = gallery('tridiag',udiag,cdiag,ldiag);

% some options for sparse eigenvalue solver
options.issym = 0;
options.disp = 0;
tic

% find 10 eigenvalues of Largest magnitude
[E_TE,Betasq] = eigs(A,10,'LR',options); toc

% These are the effective indices
Beta = sqrt(diag(Betasq));
alpha = imag(Beta);
Neff = Beta/(2*pi/lambda)
fprintf(1,'Loss in dB/um')
-10*log10(exp(-2*alpha*1e-6))
%Loss = 'dB/um' %loss in db/um


%Normalize the Field to unit power
E_TE =
E_TE./((ones(size(E_TE,1),1))*sqrt(trapz(x,abs(E_TE).^2,1).*(Beta.'/(2*omega*mu0))));

figure
%plot(x,real(E_TE(:,1)));
plotyy(x*1e6,abs(real(E_TE(:,1))),x*1e6,n)
```

xlabel('position \mum')

Appendix B: Mathematica code used to calculate change in n and k of Ge as a function of electric field

Note: The version of the code shown here is for calculating the change of n and k for SiGe. To modify it back to compute the change in n and k for Ge with applied electric field, simply change the input file to one containing n and k for pure Ge. If the input files contain n and k data for Ge, then the code will compute the change in n an k for Ge. This code is functioning code for the change n and k with electric field; just be sure to use the appropriate input files for the material under investigation.

```
Directory
   Graphics`Graphics`
```

```
Clear x, y, e1, e2, n, k, h, p, e, m, mr, t1, t2, t3, t4, t5, t6, t7,
   x1, x2, x3, x4, x5, x6, x7, Eg, EE, En, W, g, WL, f1, fff1, f2, fff2,
   f3, fff3, f4, fff4, f5, fff5, f6, fff6, f7, fff7, G1, G2, G3, G4, G5,
   G6, G7, GG1, GG2, GG3, GG4, GG5, GG6, GG7, F1, F2, F3, F4, F5, F6,
   F7, FF1, FF2, FF3, FF4, FF5, FF6, FF7, A1, A2, A3, A4, A5, A6, A7,
   RE1, RE2, RE3, RE4, RE5, RE6, RE7, RE, IM1, IM2, IM3, IM4, IM5, IM6,
   IM7, p0, p1, p2, p3, p4, p5, p6, p7, pl1, pl2, pl3, pl4, pl5, pl6,
   pl7, lambda1, lambda2, IE, lst1, lst2, lst3, lst4, lst5, lst6,
   lst7, lat11, lst12, lst13, lst14, lst15, lst16, lst17, deltaEps1,
   deltaEps2, eps1prime, eps2prime, dataGeN, lambda1, lambda2,
   eps1prime, nNew, length, deltaK, deltaN, i, reflectanceNew,
   reflectance, responsivityNew, responsivity ;

SetDirectory "C:\Program Files\Eudora\attach\FK" ;

alphaSiGe   ReadList "calculated SiGe data.txt", Number,
    RecordLists    True ;

dataGeN   ReadList "calculatedGeN.txt", Number, RecordLists    True ;

lambda1  1000; lambda2  1700; length   lambda2   lambda1; lambda3  1500;
thickness  1 10^ 4;   Ge layer thickness in cm
fieldStrength   50;    field strength in units of kV cm
A1  2.88;
me  0.08; mlh  0.043;
```

$$h = \frac{6.6256}{10^{34}}; \quad p = \frac{h}{2}; \quad e = \frac{1.6}{10^{19}}; \quad m = \frac{9}{10^{31}}; \quad mr = me\,mlh\,me\,mlh\,m$$

$$t1 = \frac{\frac{e^2\,f1^2\,p^2}{2\,mr}}{p}^{1\,3}; \quad x1 = \frac{Eg\,En}{p\,t1}; \quad En = W\,e; \quad W = \frac{1239.8}{WL}; \quad Eg = 0.8\,e;$$

```
f1 = fieldStrength = 10^5;
G1 x1_       AiryAiPrime x1  AiryBiPrime x1   x1 AiryAi x1  AiryBi x1
   Re   x1 ;

F1 x1_        AiryAiPrime x1  ^2  x1 AiryAi x1  ^2   Re   x1 ;

GG1 x1_     Abs A1  G1 x1
          ----------------- ;
            10^38 En^2

FF1 x1_     Abs A1  F1 x1
          ----------------- ;
            10^38 En^2

RE WL_     Re GG1 x1  ;
RE1 WL_    Re GG1 x1  ;
IM1 WL_    Re FF1 x1  ;
deltaEps1  Table  WL, RE1 WL  ,  WL, lambda1, lambda2  ;
deltaEps2  Table  WL, IM1 WL  ,  WL, lambda1, lambda2  ;
   "deltaEps1"
ListPlot deltaEps1, PlotRange   lambda1,lambda2 ,  0.7,0.06
   "deltaEps2"
ListPlot deltaEps2, PlotRange   lambda1,lambda2 ,  0.5,0.5
   ListPlot dataGeN,  PlotRange   lambda1,lambda2 , 4,4.3


Export "delta epsilonReal data 100kV.txt", deltaEps1,"Table"
Export "delta epsionImag data 100kV.txt", deltaEps2,"Table"
```

```
k
  Table alphaSiGe i   1 ,
      10^ 9 alphaSiGe i   1    100 alphaSiGe i   2     4 Pi ,
    i, length  ;
  ListPlot k
eps1prime
  Table alphaSiGe i   1 ,
      dataGeN i   2  ^2  k i   2  ^2 deltaEps1 i   2 ,
    i, length  ;
  ListPlot eps1prime, PlotRange   lambda1,lambda2 , 15.4,18.3
eps2prime
  Table alphaSiGe i   1 ,
      2  dataGeN i   2   k i   2    deltaEps2 i   2 ,
    i, length  ;
  ListPlot eps2prime,  PlotRange   lambda1,lambda2 , 0,0.7
```

$$nSiGe \ x\_, y\_ \quad \frac{x \quad \overline{x^2 \ y^2} \ x \quad \overline{x^2 \ y^2}}{y \quad \overline{2}} ;$$

$$kSiGe \ x\_, y\_ \quad \Big| \ \frac{x}{2} \quad \frac{\overline{x^2 \ y^2}}{2} \ ;$$

```
nNew
  Table alphaSiGe i    1 ,
     nSiGe eps1prime i    2 , eps2prime i    2    , i, length ;
  "n E "
ListPlot nNew, PlotRange   lambda1,lambda2 , 4.1,4.3
"n 0 "
ListPlot dataGeN, PlotRange   lambda1,lambda2 , 4.1,4.3
kNew
  Table alphaSiGe i    1 ,
     kSiGe eps1prime i    2 , eps2prime i    2    , i, length ;
  "k E "
ListPlot kNew, PlotRange   lambda1,lambda2 , 0,0.09
"k 0 "
ListPlot k, PlotRange   lambda1,lambda2 , 0,0.09


  deltaN Table alphaSiGe i    1 ,nNew i    2    dataGeN i    2   ,
     i,length ;
  "deltaN"
ListPlot deltaN,  PlotRange   lambda1,lambda2 ,  0.09,0.02
  "Log deltaN"
LogListPlot deltaN
deltaK Table alphaSiGe i    1 , kNew i    2    k i    2   ,
     i, length ;
  "deltaK"
ListPlot deltaK,  PlotRange   lambda1,lambda2 ,  0.05,0.05
  "Log deltaK"
 LogListPlot deltaK


  deltaalpha
   Table alphaSiGe i    1 ,4 Pi deltaK i    2   alphaSiGe i    1   ,
     i, length ;
```

```
reflectanceNew
  Table alphaSiGe i   1 ,
     nNew i   2   1 ^2 kNew i   2 ^2
     nNew i   2   1 ^2 kNew i   2 ^2 , i, length ;
  "reflectance E    "
ListPlot reflectanceNew,  PlotRange   lambda1,lambda2 , 0.2,0.6   ,
  PlotStyle  RGBColor 0,0,1
reflectance
  Table alphaSiGe i   1 ,
     dataGeN i   2   1 ^2 k i   2 ^2
     dataGeN i   2   1 ^2 k i   2 ^2 , i, length ;
  "reflectance   "
ListPlot reflectance,  PlotRange   lambda1,lambda2 , 0.0,0.6


ResponsivityNew
  Table alphaSiGe i   1 ,
    1 reflectanceNew i   2     1240 alphaSiGe i   1
     1
      Exp  4 Pi kNew i   2   alphaSiGe i   1   10 ^7
         thickness    , i, length ;
"ResponsivityNew "
lst0  ListPlot ResponsivityNew,
   PlotRange    lambda3, lambda2 , 0, 0.6   ,
  PlotStyle   RGBColor 1, 0, 0
Responsivity
  Table alphaSiGe i   1 ,
    1 reflectance i   2     1240 alphaSiGe i   1
     1
      Exp  4 Pi k i   2   alphaSiGe i   1   10 ^7 thickness    ,
    i, length ;
"Responsivity "
lst1 ListPlot Responsivity,  PlotRange   lambda3, lambda2 , 0, 0.6   ,
  PlotStyle   RGBColor 0, 1, 0
```

```
Show lst0, lst1, DisplayFunction   $DisplayFunction

  "deltaalpha"
ListPlot deltaalpha,
    PlotRange   lambda1,lambda2 ,  0.00005,0.0004

  "Log deltaalpha"
LogListPlot deltaalpha

"fieldStrength " fieldStrength
  Export "n 100kV cm .txt", nNew, "Table"
fieldStrength
Export "k 100kV cm .txt", kNew, "Table"
```

Bibliography

[1]   L. C. Kimerling, "Silicon Microphotonics," *Applied Surface Science*, vol. 159, pp. 8, 2000.

[2]   B. Zhen, J. Michel, F. Y. G. Ren, D. C. Jackson, J. M. Poate, and L. C. Kimerling, "Room temperature sharp line electroluminescence lambda = 1.54 micron from an erbium-doped silicon light-emitting diode," *Applied Physics Letters*, vol. 64, pp. 2842, 1994.

[3]   K. K. Lee, "Transmission and routing of optical signals and on-chip waveguides for Si microphotonics," in *Department of Materials Science and Engineering*. Cambridge, MA: Massachusetts Institute of Technology, 2001.

[4]   D. R. C. S. Lim, "Device integration for silicon microphotonic platforms," in *Department of Materials Science and Engineering*. Cambridge, MA: Massachusetts Institute of Technology, 2000.

[5]   H.-C. Luan, K. Wada, L. C. Kimerling, G. Masani, L. Colace, and G. Assanto, "High efficiency photodetectors based on high quality epitaxial germanium grown on silicon substrates," *Optical Materials*, vol. 17, pp. 71-73, 2001.

[6]   L. Colace, G. Masini, G. Assanto, H.-C. Luan, K. Wada, and L. C. Kimerling, "Efficient high-speed near-infrared Ge photodetectors integrated on Si substrates," *Applied Physics Letters*, vol. 76, pp. 1231-1233, 2000.

[7]   L. Colace, G. Masani, and G. Assanto, "p-i-n germanium photodetectors integrated on silicon substrates," presented at Proceedings of the SPIE The INternational Society for Optical Engineering, 2001.

[8]   R. Braunstein, A. R. Moore, and F. Herman, "Intrinsic Optical Absorption in Germanium-Silicon Alloys," *Physical Review*, vol. 109, pp. 695-710, 1957.

[9]   J. E. Bowers and C. A. Burrus, "Ultrawide-Band Long-Wavelength p-i-n Photodetectors," *Journal of Lightwave Technology*, vol. LT-5, pp. 1339, 1987.

[10]   M. B. Das, "Optoelectronic Detectors and Receivers: Speed and Sensitivity Limits," pp. 15-22, 1999.

[11]   K. J. Williams, R. D. Esman, R. B. Wilson, and J. D. Kulick, "Differences in p-Side and n-Side Illuminated p-i-n Photodiode Nonlinearities," *IEEE Photonics Technology Letters*, vol. 10, pp. 132-134, 1998.

[12]   K. J. Williams, R. D. Esman, and M. Dagenais, "Effects of High Space-Charge Fields on the Response of Microwave Photodetectors," *IEEE Photonics Technology Letters*, vol. 6, pp. 639-641, 1994.

[13]   C.-K. Sun, I.-H. Tan, and J. E. Bowers, "Ultrafast Transport Dynamics of p-i-n Photodetectors Under High-Power Illumination," *IEEE Photonics Technology Letters*, vol. 10, pp. 135-137, 1998.

[14]   P.-L. Liu, K. J. Williams, M. Y. Frankel, and R. D. Esman, "Saturation Characteristics of Fast Photodetectors," *IEEE Transactions on Microwave Theory and Techniques*, vol. 47, pp. 1297-1303, 1999.

[15]   K. J. Williams, R. D. Esman, and M. Dagenais, "Nonlinearities in p-i-n Microwave Photodetectors," *Journal of Lightwave Technology*, vol. 14, pp. 84-96, 1996.

[16]   S. M. Sze, *Physics of Semiconductor Devices*, 2nd ed. New York: John Wiley & Sons, 1981.

[17]   K. Kato, S. Hata, K. Kawano, and A. Kozen, "Design of Ultrawide-Gand, High-Sensitivity p-i-n Photodetectors," *IEICE Trans. Electron.*, vol. E76-C, pp. 214-221, 1993.

[18]   B. E. Saleh and M. C. Teich, *Fundamentals of Photonics*. New York: John Wiley & Sons, 1991.

[19]   R. J. Deri and O. Wada, "Impedance matching for enhanced waveguide/photodetector integration," *Applied Physics Letters*, vol. 55, pp. 2712-2714, 1989.

[20]   R. J. Deri, W. Doldissen, R. J. Hawkins, R. Bhat, J. B. D. Soole, L.M.Schiavone, M.Seto, N.Andreadakis, Y.Silberberg, and M. A. Koza, "Efficient vertical coupling of photodiodes to InGaAsP riib waveguides," *Applied Physics Letters*, vol. 58, pp. 2749-2751, 1991.

[21]   A. Bruno, F. Huet, M. Carre, M. Foucher, M. Billard, F. Devaux, J. Brandon, L. Menigaux, A. Carenco, and A. Scavennec, "p-i-n-i-p photodetector proposal and integration with waveguides," *Applied Physics Letters*, vol. 69, pp. 605-607, 1996.

[22]   G. Lucovsky, R. F. Schwarz, and R. B. Emmons, "Transit-Time Considerations in p-i-n Diodes," *Journal of Applied Physics*, vol. 35, pp. 622-628, 1964.

[23]   E. Braun, "Personal communication, Analog Devices," 2003.

[24]   R. G. Hunsperger, *Integrated Optics Theory and Technology*, 5th ed. Berlin Heidelberg: Springer-Verlag, 2002.

[25]   G. Guekos, *Photonic Devices for Telecommunications*. Berlin Heidelberg: Springer-Verlag, 1999.

[26]   C. J. Sher DeCusatis and C.-L. J. Jiang, "Chapter 3, Detectors for Fiber Optics," in *Handbook of fiber Optic Data Communication*, C. DeCusatis, E. Maass, D. P. PClement, and R. C. Lasky, Eds. London: Academic Press, 1998, pp. 87-114.

[27]   H. J. R. Dutton, *Understanding Optical Communications*. Saddle River, NJ: Prentice Hall, 1998.

[28]   A. Yariv, *Optical Electronics in Modern Communications*, Fifth ed. New York: Oxford University Press, 1997.

[29]   G. Keiser, *Optical Fiber Communications*, Second ed. New York: McGraw-Hill, Inc., 1983.

[30]   T. P. Lee and T. Li, "Photodetectors," in *Optical fiber communications*, S. E. Miller and A. G. Chynoweth, Eds. New York: Academic Press, 1979.

[31]   R. People, *IEEE J. Quantum Electron.*, vol. 22, pp. 1696, 1986.

[32]   R. People and J. C. Bean, "Calculation of critical layer thickness versus lattice mismatch for GexSi$_{1-x}$/Si strained-layer heterostructures," *Applied Physics Letters*, vol. 47, pp. 322-4, 1985.

[33]   E. Kasper, H. J. Herzog, and H. Kibbel, *Applied Physics Letters*, vol. 7, pp. 199, 1975.

[34] G. Masini, L. Colace, and G. Assanto, "Germanium thin films on silicon for detection of near-infrared light," in *Handbook of Thin Film Materials, Volume 4: Semiconductor and Superconductor Thin Films*, vol. 4, H. S. Nalwa, Ed., 2002, pp. 327-367.

[35] E. Kasper and F. Schaffler, *Semicond. Semimetals*, vol. 33, pp. 223, 1991.

[36] J. C. Bean, T. T. Sheng, L. C. Feldman, A. t. Fiory, and R. T. Lynch, *Applied Physics Letters*, vol. 44, pp. 102, 1984.

[37] B. S. Meyerson, *Applied Physics Letters*, vol. 48, pp. 797, 1986.

[38] B. Y. Tsaur, J. C. C. Fan, and R. P. Gale, *Applied Physics Letters*, vol. 38, pp. 176, 1981.

[39] T. F. Kuech and M. Maenpaa, *Applied Physics Letters*, vol. 39, pp. 245, 1981.

[40] M. Maenpaa, T. F. Kuech, M. A. Nicolet, S. S. Lau, and D. Sadana, "The heteroepitaxy of Ge on Si: A comparison of chemical vapor and vacuum deposited layers," *Journal of Applied Physics*, vol. 53, pp. 1076, 1982.

[41] B. Cunningham, J. O. Chu, and S. Akbar, "Heteroepitaxial growth of Ge on (100) Si by ultrahigh vacuum, chemical vapor deposition," *Applied Physics Letters*, vol. 59, pp. 3574-76, 1991.

[42] B. Y. Tsaur, M. W. Geis, J. C. C. Fan, and R. P. Gale, "Heteroepitaxyh of vacuum-evaporated Ge films on single-crystal Si," *Applied Physics Letters*, vol. 38, pp. 779, 1981.

[43] T. F. Kuech, M. Maenpaa, and S. S. Lau, "Epitaxial growth of Ge on <100> Si by a simple chemical vapor deposition technique," *Applied Physics Letters*, vol. 39, pp. 245, 1981.

[44] Y. Fukuda and Y. Kohama, "Effect of in situ thermal annealing on crystaline quality of Ge layers grown by molecular beam epitaxy on Si (100)," *Japanese Journal of Applied PHysics*, vol. 26, pp. L597, 1987.

[45] Y. Jukuda, Y. Kohoma, M. Seki, and Y. Ohmachi, "Dislocation reduction in MBE-grown Ge on Si (001) by in situ thermal annealing," *Japanese Journal of Applied PHysics*, vol. 27, pp. L1591, 1988.

[46] D. C. Houghton, J. M. Baribeau, P. Maigne, T. E. Jackman, I. C. IBassignana, C. C. Tan, and R. Holt, "Ge and GeSi heteroepitaxy on Si (100) by MBE," *Materials Research Society Symposium*, vol. 77, pp. 411, 1987.

[47] J. M. Baribeau, T. E. Jackman, D. C. Houghton, P. Maigne, and M. W. Denhoff, "Growth and characterization of Si 1-x Ge x and Ge epilayers on (100) Si," *Journal of Applied Physics*, vol. 63, pp. 5738, 1988.

[48] D. P. Malta, J. B. Posthill, R. J. Markunas, and T. P. Humphreys, "Low-defect-density germanium on silicon obtained by a novel growth phenomenon," *Applied Physics Letters*, vol. 60, pp. 844, 1992.

[49] D. P. Malta, J. B. Posthill, R. J. Markunas, T. P. Humphreys, and N. R. Parikh, "Low-defect-density Ge on Si for large-lattice-mismatched semiconductor integration and strain-engineered devices," *Materials Research Society Symposia Proceedings*, vol. 263, pp. 491, 1992.

[50] M. C. Ozturk, D. T. Grider, J. J. Wortman, M. A. Littlejohn, Y. Zhong, and D. Batchelor, "Rapid thermal chemical vapor deposition of germanium on silicon and silicon dioxide and new applications of Ge in ULSI technologies," *Journal of Electronic Materials*, vol. 19, pp. 1129, 1990.

[51] F. K. LeGoues, B. S. Meyerson, J. F. Morar, and P. D. Kirchner, *Journal of Applied Physics*, vol. 71, pp. 4230, 1992.

[52] H.-C. Luan, D. R. Lim, K. K. Lee, K. M. Chen, J. G. Sandland, K. Wada, and L. C. Kimerling, "High-quality Ge epilayers on Si with low threading-dislocation densities," *Applied Physics Letters*, vol. 75, pp. 2909-2911, 1999.

[53] G. Heigle, G. Span, and E. Kasper, "Elastic Strain energy of graded Si/sub 1-x/Ge/sub x/ buffer layers," *Thin Solid Films*, vol. 222, pp. 184, 1992.

[54] E. A. Fitzgerald, Y. H. Xie, M. L. Green, D. Brasen, A. R. Kortan, J. Michel, Y. J. Mii, and B. E. Weir, *Applied Physics Letters*, vol. 59, pp. 811, 1991.

[55] Y. H. Xie, E. A. Fitzgerald, P. J. Silverman, A. R. Kortan, and B. E. Weir, *Mater. Sci. Eng., B*, vol. B14, pp. 332, 1992.

[56] G. P. Watson, E. A. Fitzgerald, Y. H. Xie, and D. Monroe, *J. Appl. Phys.*, vol. 75, pp. 263, 1994.

[57] M. T. Currie, S. B. Samevadam, T. A. Langdo, C. W. Leitz, and E. A. Fitzgerald, "Controlling threading dislocation densities in Ge on Si using graded SiGe layers and chemical-mechanical polishing," *Applied Physics Letters*, vol. 72, pp. 1718, 1998.

[58] A. St. Amour, C. W. Liu, J. C. Sturm, Y. Lacroix, and M. L. W. Thewalt, *Applied Physics Letters*, vol. 67, pp. 3915, 1995.

[59] K. Eberl, S. S. Iyer, S. Zollner, J. C. Tsang, and F. K. LeGoues, *Applied Physics Letters*, vol. 60, pp. 3033, 1992.

[60] R. A. Soref, *J. Vac. Sci. Technol. A*, vol. 14, pp. 913, 1996.

[61] H.-C. Luan, D. D. Cannon, A. M. Agarwal, K. Wada, and L. C. Kimerling, "Passivation of High Quality Ge Epilayers for the integration of Ge Photodetectors on Si," presented at TECHCON 200, Phoenix, AZ, USA, 2000.

[62] H.-C. Luan, "Ge Photodetectors for Si Microphotonics," in *Department of Materials Science and Engineering*. Cambridge, MA: Massachusetts Institute of Technology, 2001, pp. 157.

[63] F. Schaffler, "Silicon-Germanium (Si1-xGex)," in *Properties of Advanced Semiconductor Materials*, M. E. Levinshtein, S. L. Rumyantsev, and M. S. Shur, Eds.: John Wiley & Sons, Inc., 2001.

[64] j. S. Kline, F. H. Pollack, and M. Cardona, *Helv. Phs. Acta (Switzerland)*, vol. 41, pp. 968, 1968.

[65] *Properties of advanced semiconductor materials: GaN, AlN, InN, BN, SiC, SiGe*. New York: Wiley, 2001.

[66] R. A. Logan, J. M. Rowell, and F. A. Trumbore, *Phys. Rev.*, vol. 136, pp. A1751, 1964.

[67] M. Racanelli and D. W. Greve, "Low-temperature selective epitaxy by ultrahigh-vacuum chemical vapor deposition from SiH4 and GeH4/H2," *Applied Physics Letters*, vol. 58, pp. 2096-98, 1991.

[68] W. Katsuyoshi, O. Eiji, O. Katsuya, H. Reiko, T. Masamichi, S. Hiromi, M. Toru, O. Ken'ichi, and K. Masao, "Self-aligned selective-epitaxial-growth SiGe HBTs: process, device, and ICs," *Thin Solid Films*, vol. 369, pp. 352-357, 2000.

[69] K. O, E. O, M. T, H. S, and K. W, "Si1-xGex selective epitaxial growth for ultra-high-speed self-aligned HTSs," *Thin Solid Films*, vol. 369, pp. 358-361, 2000.

[70] L. Vescan, K. Grimm, and C. Dieker, "Facet investigation in selective epitaxial growth of Si and SiGe on (001) Si for optoelectronic devices," *Journal of Vacuum Science and Technology B*, vol. 16, pp. 1549, 1998.

[71] S. G, T. R, and H. K, "Selective growth of SiGe structures in the sub 100 nm range using low pressure vapor phase epitaxy," *Journal of Crystal Growth*, vol. 154, pp. 189-92, 1995.

[72] K. Kawaguchi, U. N, and S. Y, "Formation of relaxed SiGe films on Si by selective epitaxial growth," *Thin Solid Films*, vol. 369, pp. 126-129, 2000.

[73] C. G. V. d. Walle, *Phys. Rev. B*, vol. 39, pp. 1871, 1989.

[74] e. a. Pollack, *Phys. Rev.*, vol. 172, pp. 816, 1968.

[75] H. P. Singh, "Determination of Thermal Expansion of Germanium, Rhodium, and Iridium by X-rays," *Acta Cryst.*, vol. A24, pp. 469-471, 1968.

[76] Y. Okada and Y. Tokamaru, "Precise determination of lattice parameter and thermal expansion coefficient of silicon between 300 and 1500K," *Journal of Applied Physics*, vol. 56, pp. 314-320, 1984.

[77] Y. Ishikawa, K. Wada, D. D. Cannon, J. Liu, H.-C. Luan, and L. C. Kimerling, "Strain-induced band gap shrinkage in Ge grown on Si substrate," *Applied Physics Letters*, vol. 82, pp. 2044-46, 2003.

[78] D. E. Aspnes and A. A. Studna, *Phys. Rev. B*, vol. 7, pp. 4605, 1973.

[79] R. N. Bhattacharya, H. Shen, P. Parayanthal, F. H. Pollack, T. Coutts, and H. Aharoni, *Phys. Rev. B*, vol. 37, pp. 4044, 1988.

[80] N. Bottka, D. K. Gaskill, R. J. M. Griffiths, R. R. Bradley, T. b. Joyce, C. Ito, and D. McIntyre, *J. Cryst. Growth*, vol. 93, pp. 481, 1988.

[81] C. Kittell, *Introduction to Solid State Physics*, 7th ed. New York: John Wiley & Sons, 1996.

[82] L. C. Kimerling, "Photons to the Rescue: Microelectronics Becomes Microphotonics," *The electrochemical Society Interface*, pp. 28-31, 2000.

[83] S. Luryi, A. Kastalsky, and J. C. Bean, "New infrared detector on a silicon chip," *IEEE Transactions on Electron Devices*, vol. 31, pp. 1135, 1984.

[84] H. Temkin, T. P. Pearsall, J. C. Bean, R. A. Logan, and S. Luryi, *Applied Physics Letters*, vol. 48, pp. 963, 1986.

[85] R. People, "Indirect bandgap of coherently strained GexSi1-x bulk alloys on (001) silicon substrate," *Physical Review*, vol. B32, pp. 1405, 1985.

[86] D. V. Lang, R. People, J. C. Bean, and A. M. Sergent, "Measurement of the bandgap of GexSi1-x/Si strained layer heterostructures," *Applied Physics Letters*, vol. 47, pp. 1333, 1985.

[87] J. C. Bean, presented at First International Symposium on Si Molecular Beam Epitaxy, Pennington, NJ, 1985.

[88] B. Jalali, A. F. J. Levi, F. Ross, and E. A. Fitzgerald, "SiGe waveguide photodetectors grown by rapid thermal chemical vapour deposition," *Electronics Letters*, vol. 28, pp. 269, 1992.

[89] B. Jalali, L. Naval, and A. F. J. Levi, "Si-based receivers for optical data links," *Journal of Lightwave Technology*, vol. 12, pp. 930, 1994.

[90] H. Lafontaine, N. L. Rowell, S. Janz, and D. X. Xu, "Si$_{1-x}$Ge$_x$/Si resonant-cavity-enhanced photodetectors with a silicon-on-oxide reflector operating near 1.3 μm," *Journ of Applied Physics*, vol. 86, pp. 1287, 1999.

[91]   S. Janz, J. M. Baribeau, D. J. Lockwood, J. P. McCaffrey, M. S., N. L. Rowell, D. X. Xu, H. Lafontaine, and M. R. T. Pearson, "Si/Si$_{1-x}$Ge$_x$ photodetectors using three-dimensional growth modes to enhance photoresponse at λ=1550 nm," *Journal of Vacuum Science and Technology A*, vol. 18, pp. 588, 2000.

[92]   H. Temkin, A. Antrasyan, N. A. Olsson, T. P. Pearsall, and J. C. Bean, "GeSi rib waveguide avalanche photodetectors for 1.3 mm operation," *Applied Physics Letters*, vol. 49, pp. 809, 1986.

[93]   S. B. Samevadam, M. T. Currie, T. A. Langdo, S. M. Ting, and E. A. Fitzgerald, "High quality germanium photodiodes on silicon substrates using an intermediate chemical mechanical polishing step," presented at Materials and Devices for Silicon-based Optoelectronics. Symposium, Boston, MA, 1997.

[94]   J. Oh, J. C. Campbell, S. G. Thomas, S. Bharatan, R. Thoma, C. Jasper, R. E. Jones, and T. E. Zirkle, "Interdigitated Ge p-i-n photodetectors fabricated on a Si substrate using graded SiGe buffer layers," *IEEE Journal of Quantum Electronics*, vol. 38, pp. 1238-41, 2002.

[95]   L. Colace, G. Masani, F. Galluzzi, G. Assanto, G. Capellini, L. Di Gaspare, E. Palange, and F. Evangelistis, "Metal-semiconductor-metal near-infrared light detector based on epitaxial Ge/Si," *Applied Physics Letters*, vol. 72, pp. 3175-7, 1998.

[96]   L. Colace, G. Masini, G. Assanto, H.-C. Luan, K. Wada, and L. C. Kimerling, "Efficient high-speed near-infrared Ge photodetectors integrated on Si substrates," *Applied Physics Letters*, vol. 76, pp. 1231, 2000.

[97]   H.-C. Luan, K. Wada, L. C. Kimerling, G. Masini, L. Colace, and G. Assanto, "High efficiency photodetectors based on high quality epitaxial germanium grown on silicon substrates," presented at Optoelectronics I: Materials and Technologies for Optoelectronic Devices. Symposium G of the 2000 E-MRS-IUMRS-ICEM Spring Conference. 30 May-2 June 2000 Strasbourg, France, Strasbourg, France, 2001.

[98]   K. Koyama, M. Hiroi, T. Tatsumi, and H. Hirayama, "Etching characteristics of Si1-xGex alloy in ammoniac wet cleaning," *Applied Physics Letters*, vol. 57, pp. 2202, 1990.

[99]   K. Prabhakarana, T. Ogino, R. Hull, J. C. Bean, and L. J. Peticolas, "An efficient method for cleaning Ge (100) surface," *Surface Science*, vol. 316, pp. L1031, 1994.

[100]   T. Akane, H. Okumura, J. Tanaka, and S. Matsumoto, "New Ge substrate cleaning method for Si1-x-y GexCy MOMBE growth," *Thin Solid Films*, vol. 294, pp. 153-156, 1997.

[101]   H. Okumura, T. Akane, and S. Matsumoto, "Carbon contamination free Ge(100) surface cleaning for MBE," *Applied Surface Science*, vol. 125, pp. 125-128, 1998.

[102]   N. K. Abrikosov, V. M. Glazov, and L. Chen-yuan, "Individual and joint solubilities of aluminum and phosphorus in germanium and silicon," *Russian Journal of Inorganic Chemistry*, vol. 7, pp. 429-431, 1962.

[103]   J. W. Mayer, L. Eriksson, and J. A. Davies, *Ion Implantation in Semiconductors*. New York, 1970.

[104]   H. Ryssel and I. Ruge, "Ion Implantation," in *Ion Implantation*. Chichester: John Wiley & Sons, 1986, pp. 264-289.

[105] J. M. Shannon, R. A. Ford, and G. A. Gard, "Annealing Characteristics of Highly Doped Ion IMplanted Phosphorus Layers in Silicon," *Radiation Effects*, vol. 6, pp. 217-221, 1970.

[106] H. Herzer and S. Kalbitzer, "Electrical Properties of Ion Implanted Germanium," presented at 2nd International Conference on Ion Implantation in Semiconductors, Garmisch-Partenkirchen, Bavaria, Germany, 1971.

[107] G. D. Alton and L. O. Love, "Radiation damage and substitutional chemical impurity effects in single-crystal germanium bombarded with 40-keV B+, Al+, Ga+, Ge+, P+, and Sb+ ions," *Canadian Journal of Physics*, vol. 46, pp. 695-704, 1968.

[108] R. M. Burger and R. P. Donovan, *Fundamentals of Silicon Integrated Device Technology*, vol. 1. Englewood Cliffs, NJ: Prentice-Hall Inc., 1967.

[109] S. Matsumoto and T. Niimi, *Journal of the Electrochemical Society*, vol. 125, pp. 1307, 1978.

[110] U. Sodervall and M. Friesel, "Diffusion of Silicon and Phosphorus into Germanium as Studied by Secondary Ion Mass Spectrometry," *Defect and Diffusion Forum*, vol. 143-147, pp. 1053-1058, 1997.

[111] C. Y. Chang and S. M. Sze, *ULSI Technology*: The McGraw-Hill Companies, 1996.

[112] "Ge electrical properties http://www.ioffe.rssi.ru/SVA/NSM/Semicond/Ge/electric.html," vol. 2003: Ioffe Institute.

[113] W. Franz, *Z. Naturforsch*, vol. 13a, pp. 484, 1958.

[114] L. V. Keldysh, *Sov. Phys. JETP*, vol. 7, pp. 788, 1958.

[115] P. Bhattacharya, *Semiconductor Optoelectronic Devices*. Englewood Cliffs: Prentice Hall, 1994.

[116] A. G. Aronov, I. V. Mochan, and V. I. Zemskii, "Influence of the Electric Field on the Exciton Absorption in Germanium," *Phys. Stat. Sol. (B)*, vol. 45, pp. 395-403, 1971.

[117] J. A. V. Vechten and D. E. Aspnes, "Franz-Keldysh Contributions to Third-Order Optical Susceptibilities," *Physics Letters*, vol. 30A, pp. 346-347, 1969.

[118] A. Frova and P. Handler, "Franz-Keldysh Effect in the Space-Charge Region of a Germanium p-n Junction," *Physical Review*, vol. 137, pp. 1857-1861, 1965.

[119] K. H. Gulden, M. Kneissl, P. Kiesel, S. Malzer, G. H. Dohler, X. Wu, and J. S. Smith, "Enhanced absorption modulation in hetero n-i-p-i structures by constructive superposition of field effect and phase space filling," *Applied Physics Letters*, vol. 64, pp. 457-459, 1994.

[120] G. H. Dohler, H. Kunzel, and K. Ploog, "Tunable absorption coefficient in GaAs doping superlattices," *Phys. Rev. B*, vol. 25, pp. 2616-2626, 1982.

[121] P. Kiesel, K. H. Gulden, A. Hofler, M. Kneissl, B. Knupfer, N. Linder, P. Riel, X. Wu, J. S. Smith, and G. H. Dohler, "High Speed and High Contrast Electro-optical Modulators Baed on n-i-p-i Doping Superlattices," *Superlattices and Microstructures*, vol. 13, pp. 21, 1993.

[122] S. Malzer, W. Geibelbrecht, U. Hilburger, K. M, K. P, R. Mayer, and G. H. Dohler, "Waveguide modulator structures with soft optical confinement grown by

the epitaxial shadow mask (ESM) MBE-technique," *Journal of Crystal Growth*, vol. 175/176, pp. 960-963, 1997.

[123]   L. H. Yang, R. F. Gallup, and C. Y. Fong, "Electornic properties of micro-n-i-p-i structures in silicon," *Phys. Rev. B*, vol. 39, pp. 3795-3800, 1989.

[124]   C. M. d. Sterke, "Calculation of optical absorption associated with indirect transitions in silicon n-i-p-i structures," *Journal of Applied Physics*, vol. 64, pp. 3187-3192, 1988.

[125]   H. Shen and F. H. Polllack, "Generalized Franz-Keldysh theory of electromodulation," *Physical Review B*, vol. 42, pp. 7097-7102, 1990.

[126]   M. Cardona, *Modulation Spectroscopy*. New York: Academic, 1969.

[127]   B. O. Seraphin, "Semiconductors and Semimetals," vol. 9, R. K. Willardson and A. C. Beer, Eds. New York: Academic, 1972, pp. 1.

[128]   D. E. Aspnes, in *Handbook on Semiconductors*, vol. 2, T. S. Moss, Ed. Amsterdam: North-Holland, 1980, pp. 109.